UNIVERSIDAD NACIONAL AUTÓNOMA DE MÉXICO
PROGRAMA DE POSGRADO EN ASTROFÍSICA
INSTITUTO DE ASTRONOMÍA
ASTROFÍSICA DE CAMPOS Y PARTÍCULAS

Study on dark matter-argon interactions with effective field theories and non-thermal halo components using the DEAP-3600 experiment

TESIS
QUE PARA OPTAR POR EL GRADO DE:
DOCTOR EN CIENCIAS (ASTROFÍSICA)

PRESENTA:
Ariel Zuñiga Reyes

TUTOR:
Dr. Eric VÁZQUEZ JÁUREGUI
INSTITUTO DE FÍSICA

CDMX, MÉXICO, ENERO 2022

NATIONAL AUTONOMOUS UNIVERSITY OF MEXICO
POSTGRADUATE PROGRAM IN ASTROPHYSICS
INSTITUTE OF ASTRONOMY
ASTROPHYSICS OF FIELDS AND PARTICLES

Study on dark matter-argon interactions with effective field theories and non-thermal halo components using the DEAP-3600 experiment

a dissertation submitted in partial fulfillment
of the requirements for the degree of

DOCTOR OF PHILOSOPHY (PH.D.)

in

ASTROPHYSICS

by

Ariel Zuñiga Reyes

Supervisor

Dr. Eric VÁZQUEZ JÁUREGUI
INSTITUTE OF PHYSICS

CDMX, MÉXICO, JANUARY 2022

Abstract

DEAP-3600 is an underground experiment optimized for searching WIMP dark matter at the SNOLAB laboratory (Canada) since 2016. This single-phase detector uses liquid argon as the target material. The WIMP search in 231 live-days of data (first year of operation) collected by DEAP-3600 showed no event candidates, resulting in a world-leading upper limit on the spin-independent dark matter-nucleon cross-section for argon. The thesis presents a reanalysis of that null result within a non-relativistic effective field theory framework allowing more possible interactions (in form of effective operators) to be contemplated and further examines the impact of potential dark matter halo substructures motivated by the observations of stellar distributions from the Gaia satellite and other astronomical surveys. The previous combines particle/nuclear physics and astrophysics uncertainties. Constraints were set on the coupling strength of the effective operators $\mathcal{O}_1$, $\mathcal{O}_3$, $\mathcal{O}_5$, $\mathcal{O}_8$, and $\mathcal{O}_{11}$, considering isoscalar, isovector, and xenonphobic scenarios, as well as on the specific interactions: millicharge, magnetic dipole, electric dipole, and anapole. The effects of halo substructures on each of the operators were explored as well, showing that the $\mathcal{O}_5$ and $\mathcal{O}_8$ operators are particularly sensitive to the velocity distribution, even for heavy WIMPs. Under a xenonphobic isospin-violating scenario, leading sensitivity was achieved with DEAP-3600. This research demonstrates that astrophysics and particle/nuclear physics uncertainties can significantly affect how the parameter space is constrained, and it could help to disentangle the nature of the dark matter in case of being detected. In the thesis, it is also reported for the first time the gamma-ray flux between 10 and 70 MeV at SNOLAB.

Resumen

DEAP-3600 es un experimento subterráneo optimizado para buscar materia oscura WIMP en el laboratorio SNOLAB (Canadá) desde 2016. Este detector utiliza argón líquido como blanco. La búsqueda de WIMPs en 231 días de datos (primer año de operación) recopilados por el experimento no mostró alguna señal positiva, por lo que se estableció el límite superior sobre la probabilidad de interacción materia oscura-nucleón independiente del espín que constituye el más fuerte usando argón. Esta tesis presenta un reanálisis de ese resultado nulo considerando una teoría de campo efectiva no-relativista que incluye otras posibles interacciones (expresadas como operadores efectivos) y además estudia el impacto que pueden tener posibles subestructuras de materia oscura motivadas por distribuciones estelares recientemente descubiertas con el satélite Gaia y otros sondeos astronómicos. Lo anterior combina incertidumbres astrofísicas y de física nuclear/partículas. Se obtuvieron curvas de exclusión sobre el acoplamiento de los operadores efectivos $\mathcal{O}_1$, $\mathcal{O}_3$, $\mathcal{O}_5$, $\mathcal{O}_8$ y $\mathcal{O}_{11}$ para simetrías de isoespín isoescalar, isovector y xenonfóbica; y también para interacciones específicas como la anapolar, dipolar magnética, dipolar eléctrica y milicargada. Se examinó además el efecto de las subestructuras con cada operador, revelando que los operadores $\mathcal{O}_5$ y $\mathcal{O}_8$ son particularmente sensibles a la distribución de velocidad empleada, incluso para WIMPs pesadas. Para un escenario de materia oscura xenonfóbica se logró un límite importante. La investigación demuestra que las incertidumbres astrofísicas y de física nuclear/partículas pueden afectar sobremanera los resultados. Además, este tipo de análsis ayudaría a distinguir propiedades de la materia oscura en caso de ser detectada. Finalmente, en la tesis también se reporta por primera vez una medición del flujo de rayos gammas de alta energía (10 - 70 MeV) en SNOLAB.

Acknowledgements

La sabiduria suprema es tener sueños bastante grandes para no perderlos de vista mientras se persiguen.
William Faulkner
Escritor americano

Doing a Ph.D. has been a great endeavor but ultimately rewarding. It represents a life goal that required me 23 years of education to achieve.

- I want to express appreciation to my supervisor Eric Vázquez Jáuregui for his excellent guidance, being accessible anytime, providing the best working environment, and supporting me through these four years. I could not have made a better choice!
- Special thanks go to Shawn Westerdale, who served as a second supervisor and was an example to follow, one of the most hardworking scientists I ever met.
- My gratitude to Aaron Vincent for sharing his expertise in multiple meetings, which exceedingly enriched this research.
- Thanks to the members of my tutor committee (Vladimir Ávila, Dany Page) and the Postgraduate in Astrophysics, especially: Bertha, Heike, and Adriana.
- An acknowledgment to the IFUNAM dark matter research group: Estela, Alejandro, Osmany, Ernesto, Mario, and to the whole DEAP-3600 collaboration, in particular, to Sean Daugherty, Tina Pollmann, and Chris Jillings.
- I'm also grateful to the UNAM for hosting me since 2015, which has allowed me to grow academically. In addition, thanks to the CONACyT agency for the funding through the National Scholarships Program and via Grant No. A1-S-8960. Lastly, to the support from DGAPA-UNAM (PAPIIT No. IN108020).
- Last but not least, thanks to my family in Cuba (dad, mom, brother) for providing emotional support and encouraging me to reach this academic degree. I feel blessed to have had such a great partner in crime, Alejandra, who lived this stage with me and was very comprehensive.

Contents

List of Figures

List of Tables

List of Abbreviations

AARF	Aluminium-coated Acrylic Reflectors
AV	Acrylic Vessel
CCD	Charge-Coupled Device
CDM	Cold Dark Matter
CL	Confidence Level
CMB	Cosmic Microwave Background
DAQ	Data Acquisition system
DM	Dark Matter
DEAP	Dark matter Experiment using Argon Pulse-shape discrimination
ER	Electron Recoil
GS	Gaia Sausage
GL	Gravitational Lensing
IC	In-falling Clump
IS	Isoscalar
IV	Isovector
LAr	Liquid Argon
LED	Light-Emitting Diode
LG	Light Guide
LSR	Local Standard of Rest
MW	Milky Way
NR	Nuclear Recoil
NREFT	Non-Relativistic Effective Field Theory
PE	Photo-Electron
PMT	Photomultiplier Tube
PSD	Pulse-Shape Discrimination
ROI	Region-Of-Interest
SDSS	Sloan Digital Sky Survey
SD	Spin-Dedependent interactions
SHM	Standard Halo Model
SI	Spin-Independent interactions
TPC	Time Projection Chamber
VDF	Velocity Distribution Function
WIMP	Weakly Interacting Massive Particle
XP	Xenonphobic

Chapter 1

Introduction

Nowadays, the research area of dark matter (DM) detection is highly competitive, with many collaborations worldwide seeking to directly detect DM in very sensitive detectors. In the particular case of DEAP-3600, its latest results [1], reported a limit on the isoscalar cross-section excluding values above 3.9×10^{-45} cm^2 (1.5×10^{-44} cm^2) for 100 GeV/c^2 (1 TeV/c^2) WIMP masses, where Standard Halo Model parameters were utilized and the excluded interaction was assumed to be constant (spin-, momentum transfer- and velocity-independent). Standard assumptions for astrophysics and particle/nuclear physics models are often adopted by direct-detection experiments [2], e.g. isotropic halo with Maxwellian velocity distribution, contact interaction independent of momentum exchange and isospin-conserving. Even though this allows a direct comparison among different experiments, not necessarily implies to be using an accurate description of the local DM distribution or the nuclear coupling. Important features in exclusion curves could be missed, or the parameter space may be overly constrained. For this reason, a reinterpretation of the DEAP-3600 null result was performed considering modifications to the nuclear/particle physics model by using a Non-Relativistic Effective Field Theory (NREFT), and to the astrophysics model, taking into account new substructures in the local halo that could have DM associated and therefore change the velocity distribution function (VDF). A scientific article with the results of this thesis was published in [3].

The NREFT formalism [4–6] involves DM-nucleus interactions beyond the standard spin-independent and spin-dependent ones. In this limit, scattering amplitudes are parameterized in terms of non-relativistic effective operators with dependence on velocity and/or transferred momentum. Besides, NREFT can describe more exotic interactions like DM with an anapole moment, electric or magnetic dipole moment, and millicharged. As the theory has become a systematic approach in direct-detection searches, experiments like XENON100 [7], LUX [8], SuperCDMS [9], COSINE [10], DarkSide-50 [11] have used it. A novel approach in the present thesis is to include isospin-violation with NREFT. Scenarios violating isospin symmetry are interesting since the DM coupling strength to neutrons and protons could be different.

On the other hand, astrophysical measurements by the *Gaia* satellite combined with Sloan Digital Sky Survey data indicate that the velocity distribution of DM differs from the usual Maxwell-Boltzmann distribution assumed [12, 13], as non-virialized stellar debris from mergers and accretion events locally in the galaxy have been seen, which likely indicate similar DM structures. Some research [14, 15] suggests that local DM velocities can be inferred from selecting metal-poor stars in the Solar neighbourhood and should predominantly sample the oldest mergers which correlate with the virialized DM. This idea that stars could help to track DM was adopted in the analysis even when the uncertainties for some types of substructures are notable. Studied substructures range from cold components like Nyx stream [16, 17] to hot components like in-falling extra-galactic DM, near the galactic escape velocity [18, 19]. Sixteen velocity distributions have been modeled following the method presented in [20, 21], but assuming other fractions of DM. This research also evaluates the impact of the VDFs on each effective operator

considered, an approach used by authors from [22] as well but with the Gaia Sausage substructure only. The previous study showed that the velocity distribution of the Gaia Sausage led to lower momentum transfers and therefore reduced sensitivities, except at higher DM masses, where an increase in recoils below 5–10 keV could yield a slight improvement in sensitivity.

The thesis is organized as follows: Chapter 2 gives an overview on diverse aspects of dark matter: evidence, candidates, detection strategy, and search status. Chapter 3 describes the DEAP-3600 detector. The effective field theory and details of its implementation are explained in Chapter 4 whilst Chapter 5 presents the description and modelling of non-thermal halo substructures. Chapter 6 discusses the main results, and finally, Chapter 7 shows the conclusions of the research.

Chapter 2

The quest for dark matter

Dark matter is the generic term to describe a mysterious matter which does not interact electromagnetically and comprises around 27% of the total mass-energy density of the Universe [23, 24]. Despite it remaining undetected, its existence has mostly been inferred from the gravitational effects it has on visible matter but also through precision cosmology. DM plays a critical role in the evolution of the Universe seen today, it is required to explain the formation, growth, and dynamics of galaxies/large-scale structures, the gravitational lensing phenomenon, the anisotropic temperature distribution of the Cosmic Microwave Background radiation, etc. This chapter reviews evidence of dark matter, the WIMP particle candidate and its properties, the method of direct detection, and the current status of WIMP search.

2.1 Evidence: from galactic to cosmological scales

This section introduces the most powerful evidence for DM, it is not a comprehensive list. More extensive discussions including proofs related to velocity dispersions, galaxy clusters, structure formation, type Ia supernova distance measurements, baryon acoustic oscillations are given in [25–29].

2.1.1 Rotation curves of galaxies

Important evidence for DM comes from the flatness of the rotation curves of galaxies. Mapping the circular velocity $v_c(r)$ of the objects bound to them (stars, gas) as a function of the galactic radius r, reveals that the velocity remains nearly constant (Fig. 2.1) even far beyond the visible part of the galaxy where it should to decrease. A widely accepted explanation is that there should be a large amount of non-luminous mass in the halo of the galaxies. According to the Newtonian dynamics [25] $v_c = \sqrt{G\,M(r)/r}$ = constant, with $M(r) \propto r$. G is the gravitational constant and $M(r) = 4\pi \int \rho(r) r^2 dr$, with $\rho(r)$ as the mass density profile. A universal density profile such as the Navarro-Frenk-White (NFW) derived from N-body simulations [30] may provide a good fit to rotation curve data, with a density of DM at the solar radius in the range $\rho_0 \sim 0.2$ - 0.8 GeV/cm^3 [31, 32]. Currently, the mass profile of cold and warm DM haloes seems to be better approximated by the Einasto profile [33].

A compilation of Milky Way (MW) rotation curve measurements is reported in [34], where a flat trend is observed indicating the possible existence of DM in the inner galactic region (2-15 kpc). Authors from [35] also confirm that. They found the mean rotation curve steadily declines at distances beyond ∼60 kpc after constructing the MW rotation curve from 0.2 up to 200 kpc.

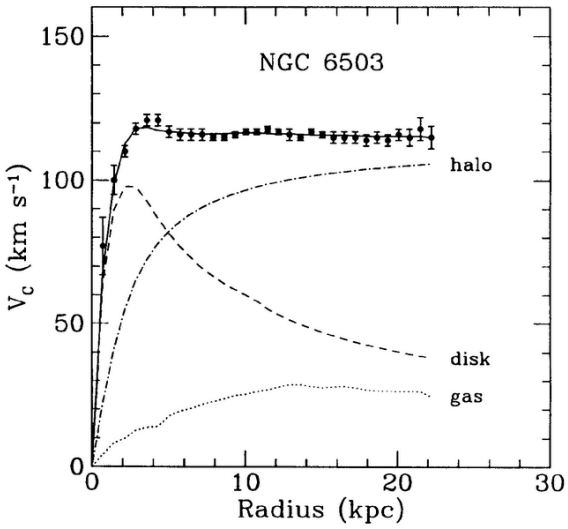

FIGURE 2.1: Rotation curve of the spiral galaxy NGC 6503 with the contribution from disk (dashed), gas (dotted), and the DM halo (dash-dotted) needed to match the data. Figure from [36].

2.1.2 Gravitational lensing

A gravitational lensing (GL) effect takes place when a massive object is located in between the observer at Earth and the object under study. Due to the gravitational pull of the massive object, the light-rays coming from the source are distorted or deflected (Fig. 2.2(a)). The observer perceives, for example, multiple images (strong lensing) or a deformation (weak lensing) of the observed image (Fig. 2.2(b)). Using this deformation, one can estimate the amount of mass of the intermediate object that is distorting the space-time along the line of sight. The luminous mass is not enough to explain the mass inferred via GL. Read [37] for more details.

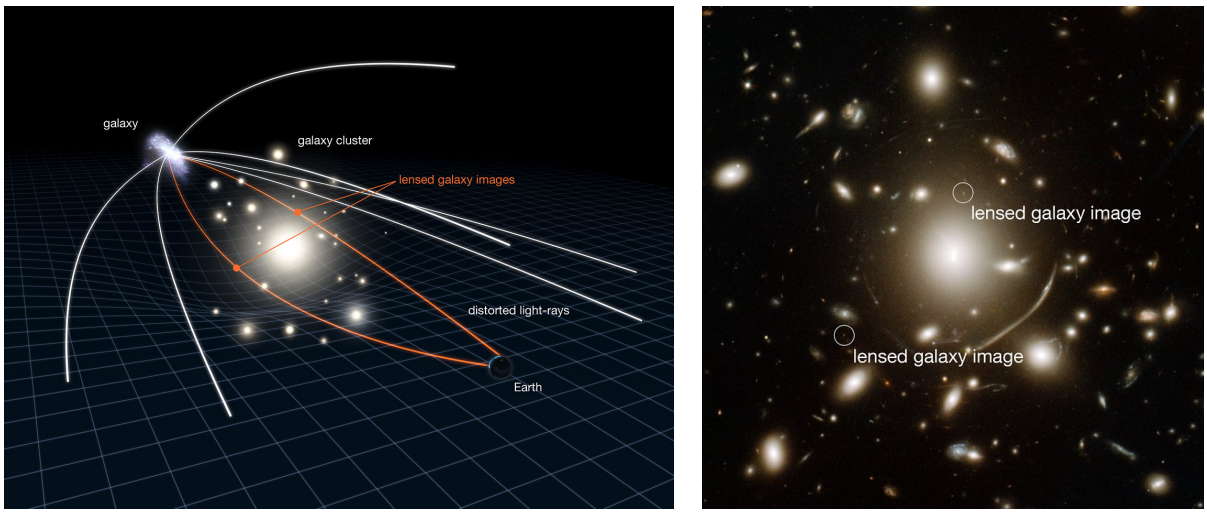

(a) (b)

FIGURE 2.2: a) Illustration describing the phenomenon of GL [38]. b) Image of a faint galaxy (tiny circle dots) magnified by the gravity of the cluster of galaxies Abell 383 located ahead with a large fraction of DM mass [39].

The Bullet Cluster is a direct proof of DM that can not be explained using modified gravity. It consists of two colliding clusters of galaxies leading to a separation of the baryonic matter (plasma) and the DM observed through GL (Fig. 2.3). The dissipation-less dark mass component traces the distribution of the cluster's galaxies which remains unaffected after the collision. Measurements through strong GL indicated that the mass associated with individual galaxies is ∼11% of the total mass, whilst 89% of the mass corresponds to DM [40].

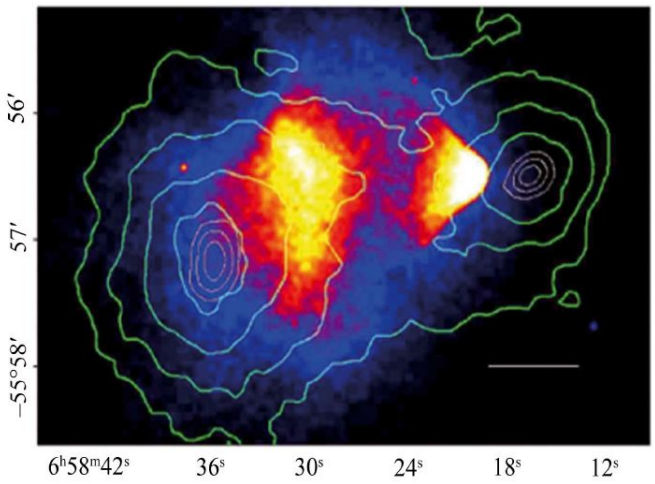

FIGURE 2.3: Merging cluster 1E0657-558 a.k.a Bullet Cluster. The smaller cluster (bullet) is shown on the right after traversing the larger cluster (left). Using the Chandra telescope the X-ray temperature distribution of the plasma was obtained: blue is coolest and white is hottest. Superimposed over the image is represented (green contours) the gravitational potential of the cluster reconstructed with weak lensing. Image from [41].

2.1.3 CMB anisotropies

The Cosmic Microwave Background (CMB) is electromagnetic radiation emitted 380,000 years after the Big Bang when the Universe became transparent to photons (recombination epoch). It comes from all-sky directions with an average thermal spectrum very close to a black-body with temperature T $\simeq$ 2.73 K [42] (spectral radiance peaking at the microwave frequencies). At scales of $\Delta T/T \approx 10^{-5}$, the CMB's temperature presents small fluctuations or anisotropies (Fig. 2.4(a)) that give indications on how the first structures grew and evolved. They originated due to acoustic oscillations in the primordial baryon-photon plasma and their size relates to the gravitational potential generated by DM, which does not interact with the photons [43, 44]. Decomposing the distribution of CMB anisotropies as a function of angular scale, a power spectrum containing a series of peaks can be constructed (Fig. 2.4(b)) which encodes relevant information about the geometry, contents, and evolution of the early stages of the Universe [45]. Under the assumption of the Λ-CDM[1] model, CMB measurements by the Planck spacecraft found DM and baryon densities of $\Omega_{DM}h^2 = 0.1200 \pm 0.0012$ and $\Omega_b h^2 = 0.02237 \pm 0.00015$, respectively [46]. The previous implies that the DM makes up 83.9% of the matter content in the Universe.

[1] Λ-CDM: is the standard model of cosmology which describes the Universe as a homogenous, isotropic, and flat space-time, whose total energy density consists of ordinary matter, dark matter, and dark energy in the form of a cosmological constant Λ.

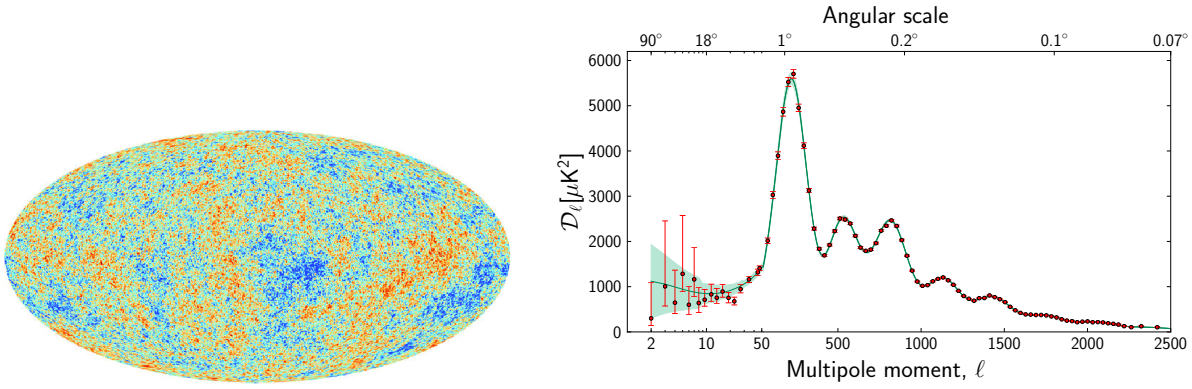

(a) (b)

FIGURE 2.4: a) Anisotropies of the CMB obtained by the Planck collaboration. b) The CMB power spectrum for both the 2014 data (dots) and the best fit of the cosmological Λ-CDM model (green line). The first peak gives information about the curvature of the Universe, the second one indicates the amount of baryon matter whilst the third peak measures the physical density of the DM. Figures from [23].

2.2 Particle dark matter

Despite the relevant amount of proofs about the existence of DM, its nature remains unknown, it could be a single particle or several new particles. What scientists know is a collection of properties that DM must fulfill:

1. Be non-luminous (not reflect, absorb or emit light).
2. Be non-relativistic and therefore able to drive structure formation.
3. Be stable, at least on the time scale of the age of the Universe.
4. Act as collision-less and non-dissipatively. This implies that the DM particle should have no interactions with ordinary matter apart from gravity or maybe only weak interactions.
5. Get produced in the right amount during the early Universe via some mechanism.

Being DM a hot topic in physics, there are plenty of theoretical models where a DM particle candidate naturally arises [25]. This thesis concentrates on WIMPs, an acronym to describe Weakly Interacting Massive Particles. Inside this category fall possible candidates as the neutralino, the lightest stable particle of super-symmetry [47] or the Kaluza-Klein photon of extra-dimensions [48]. Theory predicts WIMPs thermally produced in the early Universe with non-relativistic velocities at the present time, which makes them a suitable candidate for Cold Dark Matter (CDM). The thermal production of WIMPs with weak-scale cross-sections ($\sim 10^{-9}$ GeV^{-2} corresponding to $<\sigma v> \sim 10^{-26}$ cm^3/s) naturally leads to the correct relic DM abundance after their freeze-out from the thermal plasma ($\Omega_{DM}h^2 \approx 0.12$), this coincidence is the so-called *WIMP Miracle* [26, 28]. The mass of WIMPs is expected in the GeV/c^2-TeV/c^2 range.

2.3 Direct-detection method

The movement of the Solar System with respect to the galactic frame implies a DM flux. The direct-detection approach seeks to record the DM signature after its interaction with a target material inside a detector on Earth. The WIMP-nucleus elastic scattering is expected to produce a nuclear recoil depositing some energy (10's of keV) in the form of ionized electrons, scintillation light and/or heat/phonons [26] (Fig 2.5). These signals could be later analyzed to constrain properties like the DM mass and its cross-section. Other interaction channels studied are the inelastic WIMP scattering [49], collision of DM with electrons in the atomic shell [50], Bremsstrahlung from polarised atoms [51, 52], and e^- emission due to the *Migdal effect* [53, 54].

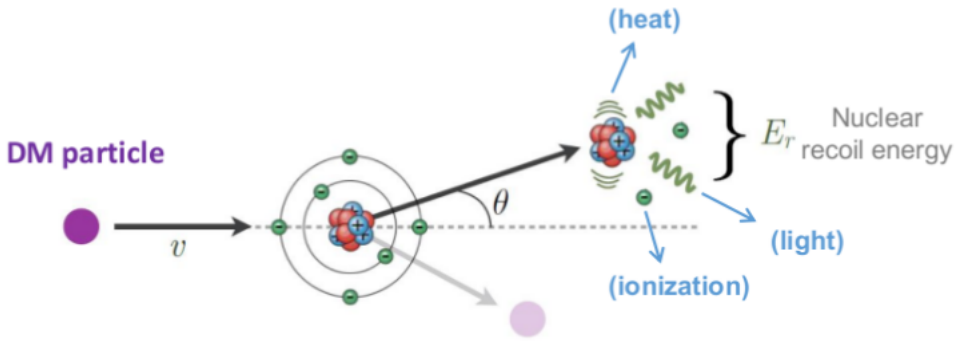

FIGURE 2.5: Representation of the DM-nucleus elastic collision. Normally, current detectors are not sensitive to the scattering angle θ.

When a DM particle of a given velocity v scatters off a nucleus, it transfers to the nucleus a certain amount of energy E_r:

$$E_r = \frac{|q|^2}{2\,m_T} = \frac{\mu_T^2\, v_{rel}^2\,(1-\cos\theta)}{m_T}, \tag{2.1}$$

with q the momentum transfer, m_T the target nucleus mass, μ_T the DM-nucleus reduced mass, v_{rel} the DM-nucleus relative velocity in the laboratory frame[2] and θ the scattering angle in the center of mass which varies from 0 to π. This energy is maximum when the DM particle backscatters in the center of mass frame ($\theta = \pi$):

$$E_{max} = \frac{2\,\mu_T^2\, v^2}{m_T}. \tag{2.2}$$

Experiments are only sensitive to recoil energies above a certain threshold, $E_{th} \leq E_r$. Inverting Eq. 2.2, the minimal speed v_{min} necessary to produce a nuclear recoil of energy E_{th} is obtained:

$$v_{min} = \sqrt{\frac{E_{th}\, m_T}{2\,\mu_T^2}}. \tag{2.3}$$

For $v_{min} < v$ a detector can observe a visible signal. Fig. 2.6 illustrates how v_{min} changes as a function of the DM mass and energy threshold assuming an argon target. Notice v_{min} increasing with larger values of E_{th} and low-mass DM particles.

[2] The laboratory frame is the one where the nucleus is initially at rest. Thus, v_{rel} is basically the incoming DM velocity v.

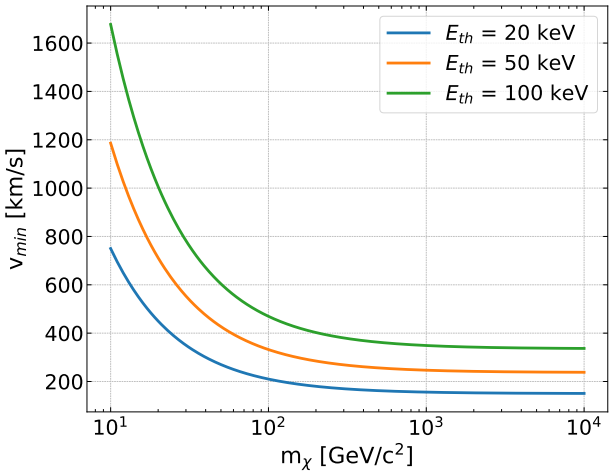

FIGURE 2.6: Minimum speed of a WIMP with mass m_χ required to produce a nuclear recoil in ^{40}Ar with energy thresholds: 20, 50 and 100 keV.

On the other hand, to understand and reduce as much as possible the backgrounds[3] in DM experiments is crucial since the values predicted for the event rate could be significantly low. A simple estimation for an argon (A=40) detector suggests a rate of $\sim 2.8 \times 10^{-6}$ events/ton/yr assuming a DM mass m_χ=100 GeV/c^2, with flux of $\phi_\chi = 6.6 \times 10^4$ cm^{-2}s^{-1}, and cross-section σ_χ=10^{-46} cm^2. The nuclear recoil spectrum relies on the DM mass with light particles producing a dominant rate at low recoil energies (Fig. 2.7(a)) and on the nucleus mass with heavier targets giving the highest rate (Fig. 2.7(b)).

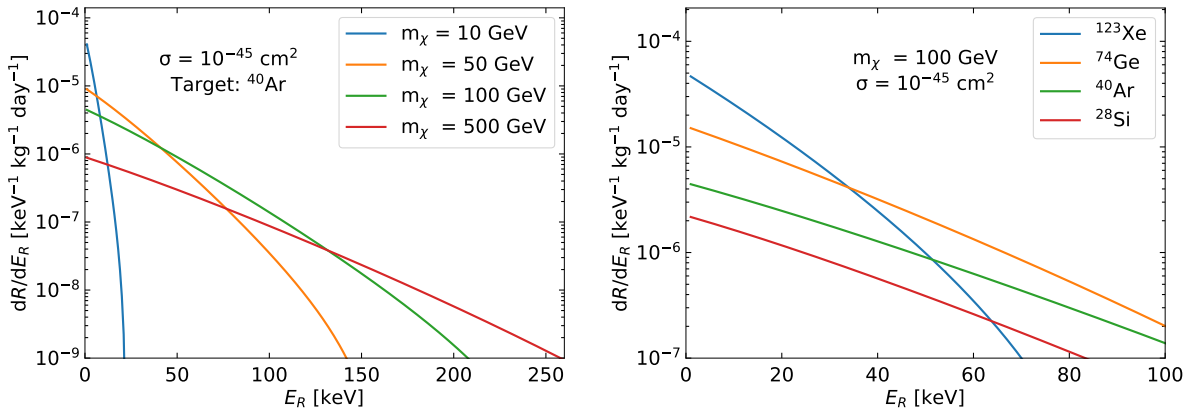

(a) (b)

FIGURE 2.7: a) Differential event rate vs. recoil energy showing the dependence on the WIMP mass $\propto 1/m_\chi$. b) Differential event rate vs. recoil energy with the dependence on the nucleus mass $\propto A^2$.

Many sophisticated technologies are currently being utilized: scintillating crystals from CsI or NaI (e.g. COSINE-100), single-(e.g. DEAP-3600) and dual-phase (e.g. LZ TPC[4]) noble liquid

[3] Backgrounds refers to signal events occasioned by particles other than WIMPs, e.g. gamma-rays from environmental radioactivity, neutrons from natural fission, cosmogenic muons, etc.

[4] TPC: Time Projection Chamber

detectors with Ar or Xe, bubble chambers using refrigerants like CF_3I or C_3F_8 (e.g. PICO-60), cryogenic bolometers using Ge, Si, $CaWO_4$, TeO_2, Al_2O_3, LiF (e.g. SuperCDMS, CRESST), semiconductor ionisation detectors (e.g. DAMIC) made with Si or/and Ge.

Some clues indicating a potential DM signal could be [55]:

- Annual modulation of the event rate due to the motion of the Earth around the Sun, with a maximal flux in June and minimal in December.
- Diurnal modulation of the DM flux direction. The detector must measure directionality.
- Subtraction of a well-understood background and look for excesses in the rate or observing a DM-like signal in analyses with negligible backgrounds.

If after the data analysis a detector does not observe WIMP-like events, the approach is to report an upper limit in the parameter space of WIMP-nucleon cross-section vs. WIMP mass showing the ruled out region above the curve. Mathematical treatment and astrophysical/particle/nuclear assumptions needed for WIMP direct-detection searches are discussed in Section 4.2 and more extensively in [56].

2.3.1 Search status and future directions

Since the '80s, the sensitivity of DM experiments has been improving considerably but without strong evidence for a discovery. Fig. 2.8(a) summarizes the status of the spin-independent (SI)[5] WIMP-nucleon interaction search with the lowest cross-section excluded in the order of 4.1×10^{-47} cm^2 at 30 GeV/c^2 by the XENON1T experiment [57]. The mass region below 10 GeV/c^2 remains poorly explored. Controversial signals (circled in the figure) have been reported by the DAMA/Libra collaboration claiming a detection. This experiment, with an array of NaI(Tl) crystals, has published a 12.9 σ annual modulation signal over 20 annual cycles [58]. However, other detectors using the same technology excluded that region of search, e.g. ANAIS-112 [59] and COSINE-100 [60]. Alternatively, isospin-violating DM models (e.g. two-Higgs doublet portal [61], new colored mediators [62], effective Z' [63]) have been considered as a way to explain this discrepancy between results. On the other hand, the XENON1T collaboration has announced a mysterious excess of electronic recoil events which is under study, and possible interpretations are: tritium background, solar axions, neutrino magnetic moment, bosonic DM [64].

Leading limits for spin-dependent (SD)[6] couplings with PICO bubble chamber were reported in [65], reaching the lowest cross-section value at 2.5×10^{-41} cm^2 for a 25 GeV/c^2 WIMP.

The second generation of DM experiments (SuperCDMS [66], LZ [67] and ADMX-Gen2 [68]) will be soon operating with sensitivities at least 10 times larger than the current detectors. Both SuperCDMS and LZ will look for low-mass and heavy WIMPs, respectively, and ADMX-Gen2 will search Axions. Other instruments already reported their search results: PandaX-4T (liquid xenon TPC) did not identify WIMP candidates above expected background in 0.63 tonne·year exposure [69], DAMIC (CCDs[7]) set the strongest constraints from a silicon target for WIMPs < 9 GeV/c^2 and observed an excess of low-energy ionization events above 50 eV$_{ee}$

[5] SI interactions: the scattering cross-section does not depend on the nuclear spin but on A^2.

[6] SD interactions: the cross-section depends on the spin of the nucleus. Nuclei with an odd number of protons/neutrons contribute due to unpaired spin (e.g. Fluorine).

[7] CCD: Charge-Coupled Device

currently under investigation [70], SENSEI (skipper-CCDs[8]) measured the lowest rates in silicon detectors and achieved world-leading sensitivity for sub-GeV DM masses with 24 days of data [71], DS-50 (liquid argon TPC) established exclusion limits under the hypothesis of DM-nucleus interaction at high-($m_\chi \sim 10$ - 1000 GeV/c^2) and low-mass WIMPs ($m_\chi > 1.8$ GeV/c^2), and for sub-GeV DM masses through the scattering with electrons [72], and the Chinese experiment CDEX-10 (pPCGe[9]) also did not find any signal and published limits on SI and SD couplings for light WIMPs (1 - 10 GeV/c^2) [73]. Whilst upcoming detectors like DarkSide-20k (liquid argon TPC) [74], XENONnT (liquid xenon TPC) [75], NEWS-G @ SNOLAB (gaseous spherical proportional counter) [76], SBC (scintillating bubble chamber) [77], SABRE (NaI(Tl) crystals inside a liquid scintillator) [78] are in the design, construction, or commissioning phase. Consult Table 1 in [79] for a comprehensive list of DM experiments and its status. The ultimate goal is the development of multiton-scale detectors like DARWIN (∼40 tonnes liquid xenon TPC) and ARGO (∼300 tonnes of liquid argon) with very large exposures for WIMP search, and sensitivity to the interaction of atmospheric neutrinos [79]. Projected limits for ARGO and DARWIN as well as for other detectors are shown in Fig. 2.8(b).

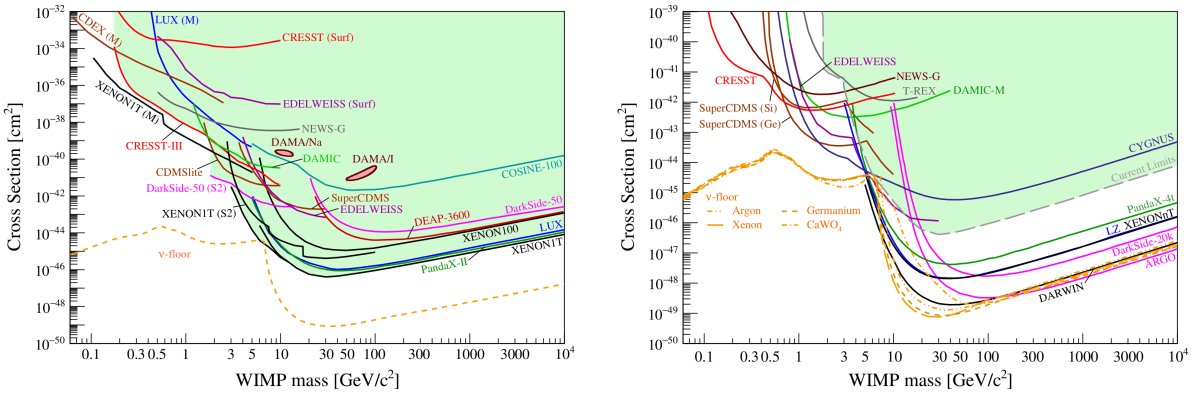

FIGURE 2.8: a) Limits set by different DM direct-detection experiments. b) Projections for future DM detectors. It is also shown the neutrino floor dependence with the target. Figures from [79].

As a result of the rising sensitivity of these detectors, in a near future, they will be able to detect neutrinos through the Coherent Elastic neutrino-Nucleus Scattering (CEνNS) and/or to allow the study of rare interactions, e.g. double electron capture in ^{124}Xe by XENON1T [80]. The neutrino floor, usually presented along with the DM limits, represents the point where the neutrinos from various sources (e.g. solar, supernova, atmospheric, etc.) will produce signals similar to that of WIMPs in the detector. An alternative to reject this background and thus to extend physics reach is to account for the directionality of the events. There are a lot of potential new technologies to take advantage of: gas TPC, nuclear emulsion, anisotropic scintillators, etc. [81]. An interesting project is CYGNUS, a worldwide directional DM experiment which could also be able to detect solar neutrinos [82]. Even reaching the neutrino floor, the WIMP paradigm can survive because there is substantial theoretical motivation to go beyond it, for instance, the neutralino in the constrained Minimal Supersymmetric Standard Model (cMSSM) at high WIMP masses [83].

[8] skipper-CCD: a special type of CCD sensor that can achieve sub-electron readout noise levels.
[9] pPCGe: p-type Point Contact Germanium detector with sub-keV energy sensitivity.

Chapter 3

Direct detection with DEAP-3600

The main features of the DEAP-3600 detector are given in this chapter. Aspects related to its structure and working principle, data acquisition, calibration, pulse-shape discrimination, position reconstruction, backgrounds, and database are reviewed. Finally, a summary of results corresponding to the first year of WIMP-search is presented.

3.1 Detector description

DEAP-3600 is a single-phase WIMP dark matter direct-detection experiment located ∼2 km underground at the SNOLAB facility in Sudbury, Canada. The detector operates since 2016 and consists of ∼3.3 tonnes of liquid argon (LAr) stored inside a spherical, radiopure acrylic vessel (AV) which is viewed by 255 photomultiplier tubes (PMTs) via acrylic light guides (LG), Fig. 3.1. Along with the LGs, various filler blocks provide thermal insulation and neutron shielding. The AV is not completely full, there is a layer of gaseous argon at the top due to a previous seal failure in the neck region that required the detector to be drained and refilled to a lower level. Inside the neck, a N_2-filled cooling coil condenses the gaseous argon into the AV, passing over through flow-guides. Details on physical properties and construction of DEAP-3600 in [84].

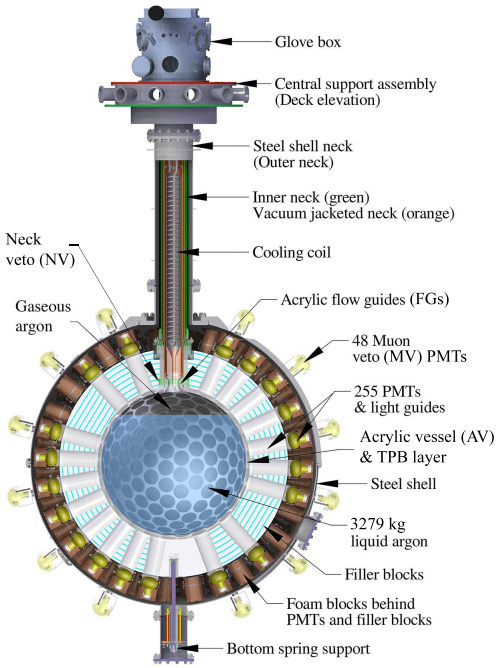

FIGURE 3.1: Description of the DEAP-3600 components. Figure from [1].

This instrument is optimized for collecting the scintillation light due to WIMP-induced nuclear recoils (NRs) after scattering with ^{40}Ar nuclei. A tetraphenyl butadiene (TPB) layer was evaporated on the inner surface of the AV. This is a wavelength shifter that converts the 128 nm LAr scintillation light to a visible spectrum, peaked at 420 nm, where it can be detected by the PMTs. Electron recoils (ERs) signals are classified as a background and rejected using the Pulse-Shape Discrimination approach (Section 3.4).

The whole setup was covered with a stainless steel shell and immersed inside a ∼300 tonnes water tank. The outer water and 48 outward-looking PMTs make up the Cherenkov muon veto. To enhance the probability of seeing WIMP signals in DM detectors like DEAP-3600, a large active volume is required. In this sense, the choice of LAr as target material is ideal because of its good properties: readily available (1% of the atmosphere components), easy to purify, high light yield, cheaper than other noble liquids (e.g. Xe, Ne), transparent to its own scintillation light, and suitable to build large volume targets, meaning a higher exposure. See Table 3.1.

TABLE 3.1: Properties of noble liquids: neon (Ne), argon (Ar) and xenon (Xe). Data from [85, 86].

	Ne	Ar	Xe
Atomic number (mass number)	10 (20)	18 (40)	54 (131)
Boiling point [K] @ 1 atm	27.1	87.3	165.0
Density [g/cm^3]	1.2	1.4	3.0
Radiation length [cm]	24.0	14.0	2.8
Light yield [γ/MeV]	30 000	40 000	42 000
dE/dx [MeV/cm]*	1.4	2.1	3.8
Scintillation wavelength [nm]	78	128	175
Singlet lifetime (ns)	18.2 $\pm$ 0.2	7.0 $\pm$ 1.0	4.3 $\pm$ 0.6
Triplet lifetime (ns)	14900 $\pm$ 300	1600 $\pm$ 100	22.0 $\pm$ 2.0
Cost per kg	$$	$	$$$$

*Mean energy loss for minimum ionizing particles

3.2 Data acquisition

The DEAP-3600 Data AcQuisition (DAQ) system is responsible for providing a high voltage to the PMTs, deciding which data is interesting, digitizing the PMT signals, writing data to disk, and controlling calibration systems. The PMTs usually operate with a high voltage (∼1500 - 1900 V) supplied by a MPOD power system. Each PMT is connected to one of 12 channels on a custom analog Signal Conditioning Board (SCB) which decouples the signal from high voltage and shapes it to make the pulse longer. A total of 27 SCBs are employed to cover all PMTs. The SCBs output is divided in three pathways: high-gain signals processed with fast CAEN V1720 waveform digitizers (250 MHz), low-gain signals processed with slow CAEN V1740 waveform digitizers (62.5 MHz), and the analog sum of each SCB which goes to the Digitizer and Trigger Module (DTM). The DTM decides when an event should be recorded or not, depending on whether the trigger conditions were met. The physics trigger considers parameters like the charge integral in a narrow time window and the prompt fraction of charge. Different computers are used to read data from digitizers. The readout software is MIDAS with output files containing many events which are later reprocessed into ROOT files. More information about the DEAP-3600 DAQ is presented in [87].

3.3 Calibration

A LED light injection system is utilized to periodically calibrate the PMTs. It consists of diverse aluminum-coated acrylic reflectors (AARFs) placed near the end of LGs and with optical fibers coupled to guide the emitted light. AARFs reflect light onto the PMTs' photocathode and the frequency of observed pulses when the LED flash is registered with some light being reflected. This LED calibration system is used to estimate the mean single photoelectron (SPE) charge value relevant to determine the number of photo-electrons (PEs) an event produces, but also for monitoring various time-dependent PMT effects like the afterpulsing rate and relative quantum efficiency.

On the other hand, the detector response is calibrated monthly with two external radioactive sources deployed inside calibration tubes around the steel shell: an AmBe neutron source to study nuclear recoils and a ^{22}Na gamma-ray source to characterize the energy and position response with induced ERs. Also, the intrinsic radioactivity from ^{39}Ar β-decays in the LAr volume offers a uniformly distributed source of ER signals used to analyze the energy response. A Gaussian energy response function is used to fit the ^{39}Ar spectrum to the one observed, resulting in a light yield of 6.1±0.4 PE/keV$_{ee}$[1] [1]. This light yield value serves to transform the PE-based energy deposited into electron-Volt units.

3.4 Pulse-shape discrimination

The Pulse-Shape Discrimination (PSD) method allows classifying nuclear and electron recoil signals. When a particle interacts in the LAr can induce the formation of dimers or excimers (excited argon molecules), which after some time decay emitting scintillation light (S1 in Fig. 3.2). Depending on the energy and nature of the interaction, the excited state of the excimers can be singlet and triplet, with very well separated lifetimes (7 ns and 1.6 μs, respectively). NRs excite predominantly the singlet state whilst ERs the triplet. The previous means that NRs will produce more prompt light compared to ERs.

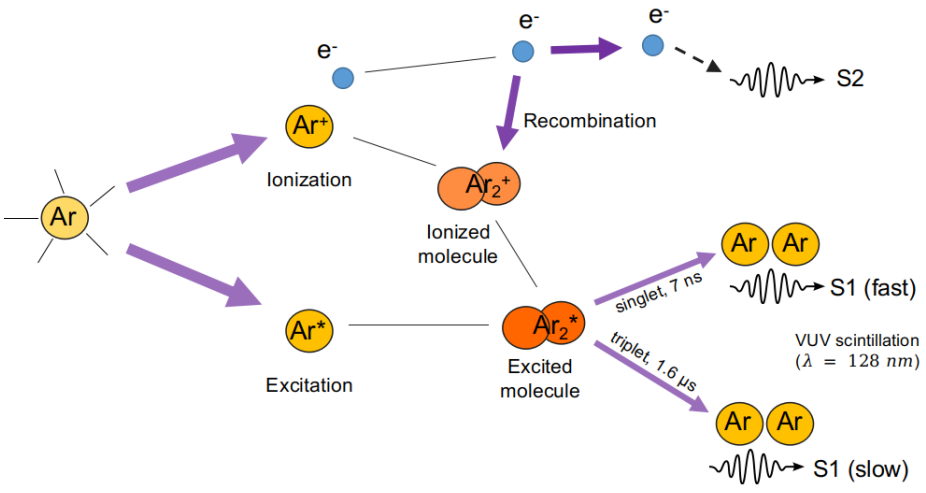

FIGURE 3.2: Argon scintillation (S1) and ionization (S2) signals derived from nuclear scattering.

[1] keV$_{ee}$: kilo electron-Volt electron-equivalent. Mathematically, $E_e(keV_{ee}) = Q_F \times E_R(keV_{nr})$, where Q_F is the nuclear quenching factor of the detector material (20-30% for argon [88]), and $E_R(keV_{nr})$ the nuclear recoil energy.

Thus, the F_{prompt} parameter accounts for such differences and it is defined as the ratio between the number of PEs in a small time window over the total PE collected:

$$F_{prompt} = \frac{Prompt\ PE[-28, 60]\ ns}{Total\ PE[-28, 10000]\ ns}. \tag{3.1}$$

F_{prompt} ranges between 0 and 1, lower values are related to ER signals and higher values to NRs. With a bi-dimensional plot of F_{prompt} vs PE (Fig. 3.3), it is possible to characterize the different events observed in the experiment. The Region-Of-Interest (ROI) where events due to WIMPs are expected is determined at high F_{prompt} (0.55 - 0.8) and low PE values (80 - 240).

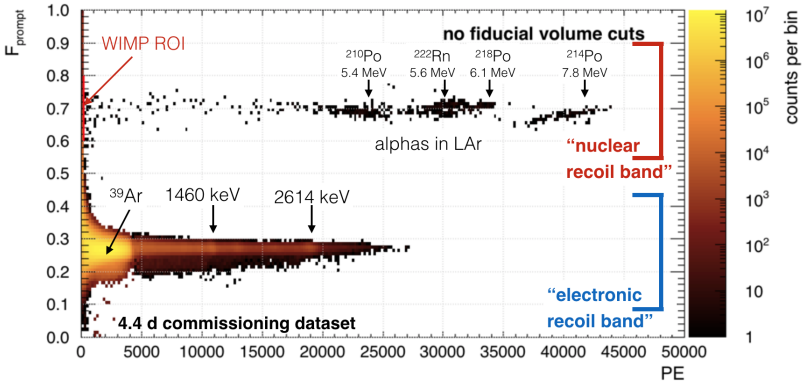

FIGURE 3.3: PSD (F_{prompt}) vs energy (PE) plane of the 4.4 days dataset [89]. The WIMP ROI is zoomed in Fig. 3.7(a). Figure from [90].

Fig. 3.4 describes the fraction of ER events expected above a given F_{prompt} value. The energy window corresponds to the range 95-101 PE (15.6-16.6 keV$_{ee}$) with the empirical PSD functions for ERs and NRs reported in [1]. With a F_{prompt} value of 0.6 the probability of having an ER is in the order of 10^{-7}, which shows the power of the PSD.

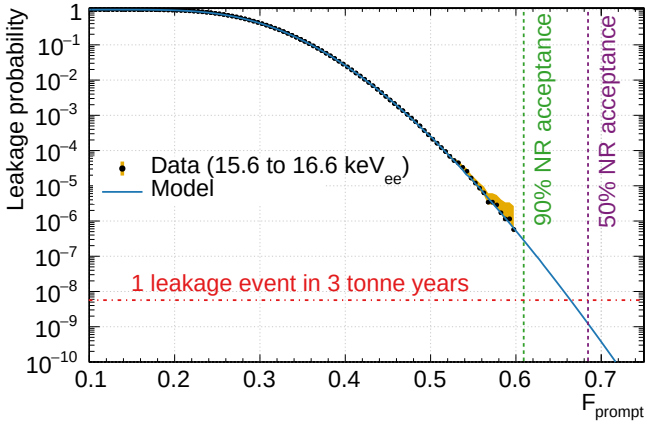

FIGURE 3.4: Probability of an ER being detected as a function of F_{prompt}. For comparison, vertical lines show the values above which 90% or 50% of NRs are expected to be found. Figure from [1].

3.5 Position reconstruction

Two position-reconstruction algorithms have been developed to identify where an interaction happened: a PE-based and a time residual-based algorithm. The PE-based algorithm determines the most likely position looking at the spatial distribution of the charge, and it is used for fiducialization [91]. The time residual-based algorithm considers the times-of-flight for photons detected in the first 40 ns of an event. The position and time are determined by identifying the vertex with the most likely time residual distribution, estimated by simulation [92]. This algorithm helps to remove backgrounds induced by α-decays from the AV neck.

3.6 Backgrounds

There are several sources of background in the experiment and some of them could significantly affect the WIMP search:

- **β and γ interactions**. Both, beta particles and gamma-rays, trigger events either by producing scintillation light in the LAr or by creating Cherenkov light in the acrylic. The dominant source of ER events is ^{39}Ar, a radioisotope which decays emitting β particles with an activity of 3.1 kBq in the LAr bulk [1]. These low-energy ERs are efficiently removed with a F_{prompt} cut (> 99%). Most of the Cherenkov light comes from ^{238}U and ^{232}Th progeny interacting with the detector materials, the ultraviolet component of this light is absorbed by the acrylic vessel and light guides, the remaining fraction generates events which reconstruct at high F_{prompt} values outside the ROI.

- **Radiogenic and cosmogenic neutrons**. The radiogenic neutrons arise from (α,n) reactions induced by α-decays in the ^{238}U, ^{235}U, and ^{232}Th decay chains, or by the spontaneous fission of ^{238}U. Despite the detector using radio-clean materials, there are remaining trace quantities of these isotopes. The polyethylene filler blocks and borosilicate glass of the PMTs are the main components contributing to the neutron backgrounds [1]. A WIMP-like signal is expected as a single scatter in the LAr volume, therefore neutron-induced multiple scattering NRs could be rejected if an adequate discriminator is developed, e.g. using a machine learning algorithm trained with Monte Carlo simulations or with high-energy alphas to distinguish single collisions and thus removing all other signals. Backgrounds due to single scatter NR events are estimated taking advantage of gamma-rays from neutron capture on ^{1}H or on ^{40}Ar detected in a 1 ms coincidence window following the NR [93]. These backgrounds are reduced by the fiducial cut. Cosmogenic neutrons are produced by high-energy atmospheric muons interacting with the detector and its environment. Because of the SNOLAB depth, few muons reach DEAP-3600 with a measured flux of (3-4) $\times 10^{-10}$ muons/cm^2/s. These signals are reduced by tagging events in which muon-induced Cherenkov light is seen in the water tank by veto PMTs [94].

- **α particles**. Signals from α-decays from short- and long-lived ^{222}Rn progeny as well as short-lived ^{220}Rn progeny are observed at several locations inside the detector [1, 95]: (1) the LAr bulk, (2) the inner acrylic vessel surface, and (3) the acrylic neck flow-guides. The α-particles from the region (1) reconstruct with energies of a few MeVs, far away from the ROI. In contrast, α events from (2) can leak into the ROI if most of their energy is deposited in the acrylic. These surface events are rejected with a fiducial cut. The dominant background comes from α-decays in (3). The geometry of the neck flow-guides shadows

scintillation light, thus only a small fraction of the photons from an event are detected by the PMTs resulting in a signal-like event, with a reconstructed position in the fiducial region. However, the high energy of these events relative to WIMP-like NRs allows them to be separated from WIMPs using PSD. These backgrounds are further suppressed by rejecting events with significant disagreement between both position reconstruction algorithms and by removing events with very early or excessive amounts of light seen in the PMTs in the gaseous-argon region.

3.6.1 High-energy gammas

A complementary analysis was conducted in this thesis work to measure the underground flux of photons with energies above 10 MeV at SNOLAB. These high-energy gamma-rays need to be well characterized because may produce (γ, n) reactions in the detector materials near the LAr volume or lead directly to photo-nuclear reactions in the LAr volume itself, and thus originating spurious signals which can imitate that of WIMPs. In addition, knowing its flux can help to design appropriate shielding for future experiments.

The experimental setup (Fig. 3.5) consisted of a sodium iodide crystal (NaI) with dimensions of 10.16 cm $\times$ 10.16 cm $\times$ 40.64 cm and a mass of 15.4 kg. To record the scintillation light from the NaI crystal, a PMT manufactured by Electron Tubes Enterprises (model 9306KB) was attached to the 3.5" diameter window of the crystal enclosure. An acetal plastic casing was placed over the entire PMT/window and the crystal was inserted inside an aluminum case. The data acquisition system was a Spectrum Techniques UCS30 analyzer with 1024 channels. The acquisition mode was set to PHA Pre-Amp and a positive high-voltage of 700 V was applied.

FIGURE 3.5: The NaI detector with mounted PMT next to the laptop used for data taking.

Data was collected between 2018 and 2021 with the detector unshielded and mostly placed at the bottom of the Cube Hall cavern. After data cleaning, a livetime of 602 days (1.65 years) was achieved. The energy calibration used dominant peaks of the spectra originated from natural radioactivity: ^{40}K with the emission of a 1.460 MeV gamma-ray and ^{208}Tl producing

a gamma line of 2.615 MeV. A Gaussian fit to these peaks allowed their bins to be identified. The channel-to-energy conversion was performed doing a linear fit (E = m·C + n, with E: energy and C: channel) and estimating the fit parameters (slope, intercept) by linear regression. The flux per energy bin Φ is calculated as $\Phi = \mathbb{R}^{-1}\cdot R$, where $\mathbb{R}^{-1}$ is the inverse of an efficiency matrix determined with a Geant4 simulation and R is the rate per energy bin ($\gamma/cm^2/yr$).

According to [96], there are two possible interpretations for gammas above 10 MeV. In the energy range 10 - 30 MeV, cosmic-muons bremsstrahlung in the surrounding rocks or materials presumably induces gammas. Above 30 MeV, the events are likely due to muons hitting directly the NaI crystal. Measured gamma flux values are shown in Table 3.2 for different energy bins and plotted in Fig. 3.6 along with the expected muon flux. The later was obtained by scaling the total muon cosmic-ray flux reported at SNOLAB (3.31 ± 0.01 (stat) $\pm$ 0.09 (sys)$\times 10^{-10}$ cm^{-2} s^{-1} [97]) with the crystal efficiency to muons calculated through a simulation.

TABLE 3.2: Gamma-ray flux per energy interval without muon contribution. The flux in the last bin was not reported because the muon flux is dominant.

Energy range (MeV)	Flux (cm^{-2} yr^{-1}) $\times 10^{-3}$
10 - 11	93.7 ± 4.0
11 - 13	28.3 ± 2.0
13 - 15	5.88 ± 1.00
15 - 20	3.79 ± 0.90
20 - 30	0.852 ± 0.600
30 - 70	–

Fig. 3.6 indicates that events above 30 MeV are likely correlated to muons. By integrating both distributions and subtracting the total muon flux, a value of 0.13 ± 0.01 cm^{-2} yr^{-1} is obtained for the total gamma-ray flux between 10 and 70 MeV.

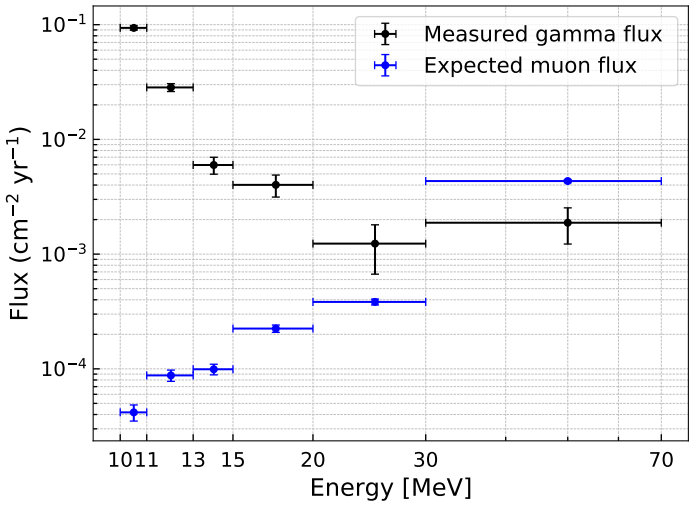

FIGURE 3.6: Gamma-ray flux measured between 10 and 70 MeV at SNOLAB. An estimation of the expected muon flux is also presented.

3.7 Database

The DEAP detector daily generates a data volume exceeding 600 GB, among which are physics and non-physics data (a.k.a metadata). The physics data refers to ROOT files organized in runs where the WIMP search is carried out, and they are stored in disks at ComputeCanada[2]clusters. Metadata includes information about components and parameters that are needed in analysis, for instance, PMTs (SPE charge, noise, afterpulses), detector hardware (optical transmission properties, location of PMTs), DAQ/Electronics (settings, run information), calibration constants, data quality, runlists, and many more. All the latest information is saved in the DEAP database (DB), a central store based on remote DB servers running CouchDB[3], an open-source document-oriented NoSQL database software for working with many disparate types of data in JSON format.

Currently, five servers are mirroring each other's databases: DUG1 (SNOLAB underground) dedicated to the DAQ, DDAQ3 (SNOLAB surface) for development and fall-back, PENGUIN (Carleton University) for production use, and RAVEN (Graham cloud at the University of Waterloo)/ BLACKBIRD (CIEMAT, Spain) for processing. PENGUIN also hosts a DB (PostgreSQL[4]-based) utilized for slow control systems which record environmental data (temperatures, pressures, liquid levels). Getting information from the DB can be done through the DB website or accessing via C++/Python scripts. There is a DB document specification describing its content and a changes log TWiki page. A database manager ensures the data in the DB is consistent, complete, and searchable; the CouchDB servers properly interface with the DEAP analysis tools; help users to retrieve information from the DB, and periodically upload/update calibration constants from working groups. Description of the DEAP database is in [98].

3.8 First year of WIMP search

In 2019, the collaboration reported the DM search results from the first year of running (Nov. 2016 to Oct. 2017), with a total livetime of 231 days, and an exposure of 758 tonne·years (LAr mass of 3279 kg). The ROI (Fig. 3.7(a)) was delimited by four distinct criteria: lower-left bound (95-160 PE) defined such as the ERs leakage events are < 0.05, the lower-right curve between 160-200 PE sets a constant 1% NR acceptance loss, the upper bound was set to ensure < 0.5 events from α-decays in the AV neck whilst beyond the vertical limit at 200 PE the rate of α-particle and neutron-related backgrounds events increases. A fiducial radius of 630 mm was also defined.

Normally, only a fraction of the data is available for analysis to the researchers to reduce or eliminate any kind of bias, this is called a blind analysis strategy. The methods and studies developed working with that sample of data are later utilized with the whole dataset once the collaboration decides to unblock it.

After applying fiducial and background rejection cuts to 1 year of data, a background expectation of < 1 event in the ROI was achieved. For a fiducial mass of 824 kg, the average WIMP efficiency was 35.4%. The next step is quantifying the remaining events inside the ROI. No signal candidates were observed, therefore an exclusion limit was set [1].

[2] https://www.computecanada.ca/home/
[3] https://docs.couchdb.org/en/stable/
[4] PostgreSQL is an open-source relational database management system for handling structured data.

The statistical approach considered for limit setting is Maximum Patch, a method similar to Maximum Gap, but instead of looking only at the energy spectrum, it looks for boxes in a 2D parameter space (PE vs. F_{prompt}) [99]. The Maximum Gap method compares the signal to the observed background events, finds the gap in background events where the most signal events should be, and uses that to find the maximum cross-section consistent with the data (to a given confidence level, C.L.) for a given WIMP mass. It requires a model of the signal, but not of the background. With zero events, Poisson statistics allows to exclude 2.3 WIMP events, resulting in an upper limit (90% C.L.) on the SI WIMP-nucleon cross-section (Fig. 3.7(b)) which represents a world-leading constraint with a LAr target.

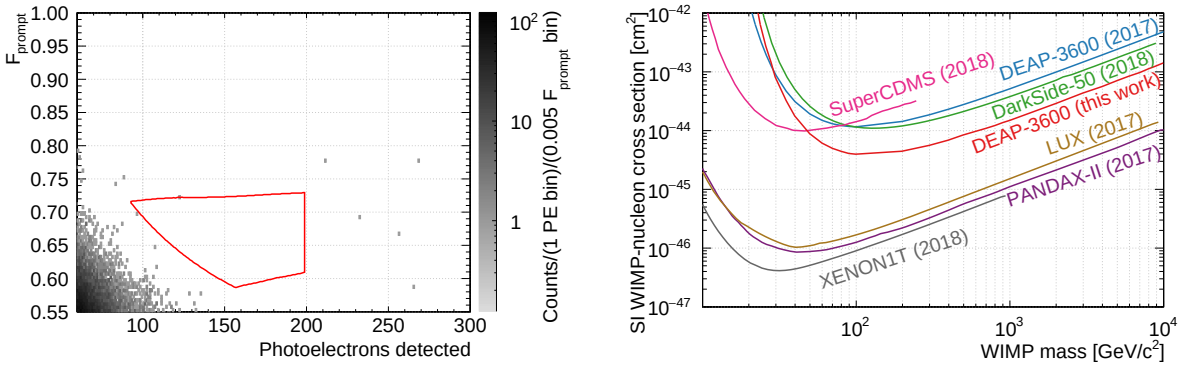

(a) (b)

FIGURE 3.7: a) Distribution of events in the PE vs. F_{prompt} parameter space after applying cuts. There are no events within the ROI (red). b) Upper limits (90% C.L.) on the spin-independent WIMP-nucleon cross-section vs. WIMP mass for DEAP-3600 (red) and other experiments. Plots from [1].

Despite DEAP-3600's null result, the analysis demonstrated the power of PSD to achieve low backgrounds in WIMP searches and also reported a detailed description of backgrounds. Exploring alternative scenarios of WIMP-nucleus couplings other than SI, could be useful to interpret a future detection. Likewise, including new data-motivated velocity distribution functions make the event rate calculation more detailed. That is why the upcoming sections explore the effects of applying an effective theory and other VDFs to this first year of DEAP-3600 data.

Chapter 4

Non-Relativistic Effective Field Theory

This chapter introduces the effective field theory of dark matter direct-detection that can help to explore possible blind spots in the sensitivity of experiments. Formulas used in the scattering cross-section calculation, description of specific interactions, and details on the software employed in the analysis are discussed.

4.1 Overview of NREFT

The velocity of DM particles in the MW halo is estimated to be of the order $v/c \sim 10^{-3}$ (c is the speed of light) [100, 101]. If the WIMP mass is in the GeV/c^2–TeV/c^2 range, the expected recoil energies $\mathcal{O}$(keV) are much smaller than typical nuclear binding energy (1–10 MeV/nucleon). This justifies the treatment of DM scattering against the nucleus using non-relativistic quantum mechanics [4]. Considering a Non-Relativistic Effective Field Theory (NREFT) direct-detection experiments have a more general way to characterize their results. NREFT provides a detailed formulation to describe all possible dark matter-nucleus couplings and a better description of the nuclear response. Instead of the classical two couplings SI and SD, six nuclear response functions arise from different effective operators. In this framework, the nucleus is not treated as a point-like particle but its composite nature is reflected [102]. Table 4.1 shows the main non-relativistic effective operators up to the twelfth operator, where $\mathcal{O}_1$ represents the standard SI interaction and $\mathcal{O}_4$ the standard SD. The nucleon mass (m_N) in the equations is used to construct the dimensionless quantity $\vec{q}/m_N$, a parameter related to the relative velocities of nucleons bound in the nucleus [6]. Transforming the operators (see [5, 6] for details) and grouping them into a linear combination, result in a general expression for the WIMP-nucleus cross-section (Eq. 4.7, 4.8).

TABLE 4.1: NREFT operators. ✓ indicates the operators surviving for an argon target and ✗ the non-available ones (not the full list).

	Operators		**Operators**
✓	$\mathcal{O}_1 = 1_\chi 1_N$	✗	$\mathcal{O}_7 = \vec{S}_N \cdot \vec{v}^\perp$
✗	$\mathcal{O}_2 = (v^\perp)^2$	✓	$\mathcal{O}_8 = \vec{S}_\chi \cdot \vec{v}^\perp$
✓	$\mathcal{O}_3 = i\vec{S}_N \cdot (\frac{\vec{q}}{m_N} \times \vec{v}^\perp)$	✗	$\mathcal{O}_9 = i\vec{S}_\chi \cdot (\vec{S}_N \times \frac{\vec{q}}{m_N})$
✗	$\mathcal{O}_4 = \vec{S}_\chi \cdot \vec{S}_N$	✗	$\mathcal{O}_{10} = i\vec{S}_N \cdot \frac{\vec{q}}{m_N}$
✓	$\mathcal{O}_5 = i\vec{S}_\chi \cdot (\frac{\vec{q}}{m_N} \times \vec{v}^\perp)$	✓	$\mathcal{O}_{11} = i\vec{S}_\chi \cdot \frac{\vec{q}}{m_N}$
✗	$\mathcal{O}_6 = (\vec{S}_\chi \cdot \frac{\vec{q}}{m_N})(\vec{S}_N \cdot \frac{\vec{q}}{m_N})$	✓	$\mathcal{O}_{12} = \vec{v}^\perp \cdot (\vec{S}_\chi \times \vec{S}_N)$

The operators were built out with four three-vectors: $i\frac{\vec{q}}{m_N}$ - momentum transfer, $\vec{v}^{\perp}$ - component of the velocity perpendicular to the momentum transfer, $\vec{S}_\chi$ - DM spin and $\vec{S}_N$ - nucleon spin. They are Hermitian and Galilean invariant quantities. The momentum transfer is equivalent to $\vec{q} = \vec{p}' - \vec{p} = \vec{k} - \vec{k}'$, where $\vec{p}$ ($\vec{p}'$) is the incoming (outgoing) WIMP momentum and $\vec{k}$ ($\vec{k}'$) the incoming (outgoing) nucleon momentum (Fig. 4.1(a)). On the other hand, the transverse-velocity operator $\vec{v}^{\perp} \equiv \vec{v} + \frac{\vec{q}}{2\mu_N}$ ($\mu_{N=p,n} = \frac{m_\chi m_N}{m_\chi + m_N}$) satisfies $\vec{v}^{\perp} \cdot \vec{q} = 0$, as a consequence of energy conservation (Fig. 4.1(b)).

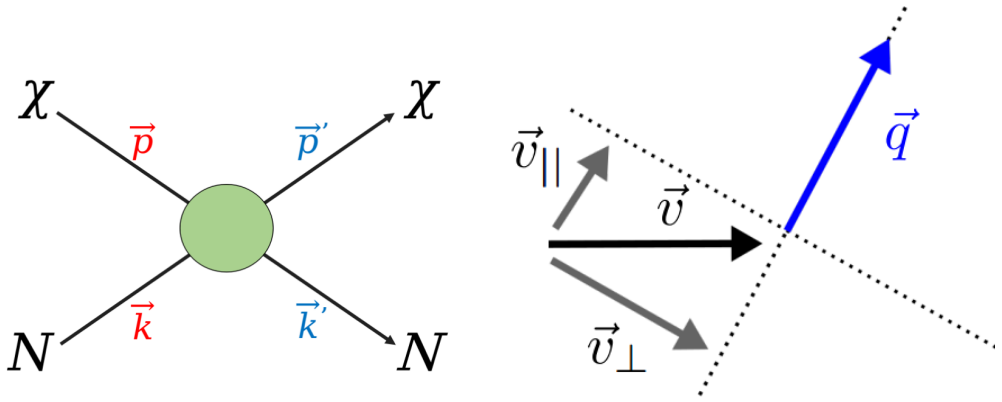

(a) (b)

FIGURE 4.1: a) Feynman diagram for the effective WIMP-nucleon scattering with a massive mediator. b) Representation of the parallel and perpendicular components of the relative incoming velocity $\vec{v}$ with respect to the momentum transfer $\vec{q}$.

DEAP-3600 uses liquid argon (^{40}Ar) as the target; this material has no unpaired nucleons (Z=18 and A-Z=22) meaning that the ground state nucleus has zero total spin and hence the operators $\mathcal{O}_4$, $\mathcal{O}_6$, $\mathcal{O}_7$, $\mathcal{O}_9$, $\mathcal{O}_{10}$ don't contribute. Other operators expressed in terms of the nucleon spin can survive ($\mathcal{O}_3$ and higher-order: $\mathcal{O}_{12}$, $\mathcal{O}_{15}$), as they account for the angular momentum of nucleons and the spin-orbit coupling is non-zero. The $\mathcal{O}_2$ operator is discarded because it is a second-order correction to the SI operator $\mathcal{O}_1$. The contribution of the operators to DM-nucleus scattering was computed using a nuclear shell model and parameterized in [103].

4.2 WIMP-nucleus scattering theory

The expected number of events (N_E) due to the DM-nucleus elastic scattering to be observed in a direct-detection dark matter experiment is obtained through the Eq. 4.1:

$$N_E = \frac{\epsilon\,\rho_0}{m_T\,m_\chi} \int_{E_r^{min}}^{E_r^{max}} \varepsilon(E_r)\,dE_r \int_{v_{min}}^{v_{esc}} v \cdot f[\vec{v} + \vec{v}_E(t)] \cdot \frac{d\sigma_T(v, E_r)}{dE_r}\,d\vec{v}. \tag{4.1}$$

The above expression requires a set of parameters that can be divided into three groups:

- **Detector parameters** (A: atomic mass, m_T: nucleus mass, E_r: nuclear recoil energy, ε: detector efficiency, ϵ: exposure), which are chosen via the material selection of the target and the experimental setup. The detector efficiency is an energy-dependent function

describing the fraction of recoil events observed in a given energy ROI, defined within $[E_r^{min}, E_r^{max}]$. The total exposure is the product of the detector mass and the run-time. v_{min} is the minimum WIMP speed needed to produce a nuclear recoil of energy E_r (Eq. 2.3).

- **Astrophysical parameters** (ρ_0: local DM density, $\vec{v}$ and $f[\vec{v}+\vec{v}_E(t)]$: DM velocity and velocity distribution function boosted to Earth reference frame and normalized to unity, v_{esc}: DM galactic escape speed), depend on the halo model used and are fixed by astrophysical observations. SHM values and Maxwell-Boltzmann velocity distribution are typically used. The Earth velocity relative to the DM in galactic coordinates[1] ($\vec{v}_E(t)$) is time-dependent due to the revolution and rotation of the Earth throughout the year:

$$\vec{v}_E(t) = \vec{v}_\odot + \vec{v}_O(t) \tag{4.2}$$

$$\vec{v}_\odot = \vec{v}_c + \vec{v}_{pec} = (0, v_0, 0) + (\mathrm{U}, \mathrm{V}, \mathrm{W}) \tag{4.3}$$

$$\vec{v}_O(t) = \vec{v}_\oplus[\hat{e}_1 \sin w(t-t_a) + \hat{e}_2 \cos w(t-t_a)] \tag{4.4}$$

where $\vec{v}_\odot$ is the Sun's velocity with respect to the halo and set by the velocity of the Local Standard of Rest (LSR), $\vec{v}_c$ the circular velocity at the Sun position and $\vec{v}_{pec}$, Sun's peculiar velocity with respect to LSR. On the other hand, the yearly Earth orbital velocity is $\vec{v}_O(t)$ with mean magnitude $v_\oplus$. $w = 2\pi/365$, is the angular velocity over one-year period and t_a = March 22$^{\mathrm{nd}}$ (81$^{\mathrm{st}}$ day of the year, vernal equinox time). Taking the values from [20]: v_0 = 220 km/s, (U, V, W) = (11.1, 12.24, 7.25) km/s, $v_\oplus$ = 29.79 km/s, and the unit vectors:

$\hat{e}_1$ = (0.9941, 0.1088, 0.0042) $\qquad$ $\hat{e}_2$ = (-0.0504, 0.4946, -0.8677)

- **Particle/nuclear physics parameters** (m_χ: DM mass, σ_T: DM-nucleus cross-section), depend on the actual model for the DM particle and its interaction with the nucleus. To compare the results of experiments with different target materials, σ_T is often scaled to σ_N, the WIMP-nucleon cross-section. For SI searches, the differential cross-section is [104]:

$$\frac{d\sigma_T(v, E_r)}{dE_r} = \frac{m_T \sigma_N}{2\, v^2 \mu_N^2} \cdot \left[Z + \frac{f_n}{f_p}(A - Z)\right]^2 \cdot F^2(E_r)\,, \tag{4.5}$$

where m_T is the nucleus mass, Z the atomic number, μ_N the DM-nucleon reduced mass, v the DM speed, $f_{n,p}$ the couplings to neutrons/protons, normally assumed to be equal ($f_n = f_p$) and $F^2(E_r)$ the nuclear form factor which describes the response of the target nucleus. In particular, the square of the form factor at a given recoil energy gives the probability of having a coherent nuclear recoil at that energy. A reasonably approximation widely used is the Helm form factor [56, 105]:

$$F(x) = \frac{3\, j_1(x)}{x}\, \exp\left[-\frac{(x \cdot s)^2}{2R^2}\right], \tag{4.6}$$

defining x as a dimensionless parameter, $x = qR/\hbar c = \sqrt{2 m_T E_r}(R/\hbar c)$. $j_1(x)$ is the first order spherical Bessel function, $j_1(x) = \sin(x)/x^2 - \cos(x)/x$. This expression is based on the Woods-Saxon potential describing a nucleus A, with a radius $R \approx 1.2\, A^{1/3}$ fm and a skin-thickness $s \approx 0.9$ fm.

[1] Galactic coordinates: in the Cartesian representation, the X-axis points toward the center of the galaxy, the Y-axis aligns with the rotation of the stars of the disk, and the Z-axis is perpendicular to the galactic plane.

4.3 Cross-section in NREFT

Traditionally, the cross-section in Eq. 4.5 is utilized for most DM experiments because of its simplicity, but this section provides a more complete calculation. The NREFT is first developed at nucleon-level and later mapped onto the nucleus, being the nuclear interaction the sum of DM particles scattering with the individual nucleons of the nucleus. This process can't be considered coherent as the inverse of momentum transfers involved are comparable to the nuclear radii, implying the nuclei are not point-like from the perspective of DM [4, 6]. The differential cross-section in NREFT is presented, through the scattering amplitude $\mathcal{M}_T$, as the product of DM particle (R) and nuclear (W) response functions (Eq. 4.7, 4.8).

$$\frac{d\sigma_T(v, E_r)}{dE_r} = \frac{2m_T}{4\pi v^2}\left[\frac{1}{(2j_\chi+1)}\frac{1}{(2J+1)}|\mathcal{M}_T|^2\right], \tag{4.7}$$

where j_χ and J are the DM and nucleus spin, respectively. The non-relativistic matrix amplitude-squared $|\mathcal{M}_T|^2$, decomposes as (averaging over initial spins and summing over final spins):

$$\left[\frac{1}{(2j_\chi+1)}\frac{1}{(2J+1)}|\mathcal{M}_T|^2\right] = \frac{4\pi}{2J+1}\sum_k \sum_{\tau=0,1}\sum_{\tau'=0,1} R_k^{\tau\tau'}\left[v_T^{\perp 2}, \frac{q^2}{m_N^2}, \left(c_i^\tau\, c_j^{\tau'}\right)\right]\cdot\, W_k^{\tau\tau'}(y)\,, \tag{4.8}$$

R_k is the DM response function containing the particle physics information and it depends on the transverse component of the velocity, the momentum transfer, and the coupling strength. On the other hand, W_k is the target-dependent nuclear response function that encompasses nuclear physics, is a function of the dimensionless variable y:

$$y = \left(\frac{q\,b}{2}\right)^2 = \frac{m_T\,E_r b^2}{2}, \tag{4.9}$$

$$b = \sqrt{41.467/(45A^{1/3} - 25A^{-2/3})}\ \text{fm}, \tag{4.10}$$

being b the harmonic oscillator size parameter. The theory is in terms of an isospin basis, where $\tau = 0$ and $\tau' = 1$ correspond to the isoscalar and isovector cases, respectively. In the proton-neutron basis, the couplings c^p, c^n relate to c^0, c^1 through $c^p = \frac{1}{2}(c^0 + c^1)$ and $c^n = \frac{1}{2}(c^0 - c^1)$. The k index indicates six nuclear operators plus two interference terms ($k = M, \Sigma', \Sigma'', \Delta, \Phi'', \tilde{\Phi}', \Phi''M, \Delta\Sigma'$).

- M is the standard SI response, describing the nucleon density inside the nucleus.
- Σ', Σ'' are the transverse and longitudinal (with respect to $\vec{q}$) components of the nucleon spin (either p or n). They favor elements with unpaired nucleons. A certain linear combination of them is the usual SD coupling.
- Δ, at $q = 0$, measures the net angular-momentum of a nucleon (either p or n). This response can be an important contribution to the coupling of DM to elements with unpaired nucleons, occupying an orbital shell with non-zero angular momentum.
- Φ'', at $q = 0$, is related to the angular momentum and spin (L · S). It favors elements with large, not fully occupied, spin-partner angular-momentum orbitals. It tends to favor heavier elements, as these have larger L orbitals not fully occupied. It can be of the same order as the M response for heavier elements.

- $\tilde{\Phi}'$ is tensor, arising only in CP non-conserving interactions and thus solely contributes if the nucleus' spin is $J \geq 1$. This response function is somewhat exotic, coming from other interactions that don't arise for traditional spin-0 or spin-1 exchanges.

Eq. 4.8 was expanded taking into account DEAP-3600's target. Non-zero W_k functions for ^{40}Ar were calculated in [103], remaining the M, Φ'', $\Phi''M$ responses and their corresponding R_k.

$$\frac{1}{2j_\chi+1}\frac{1}{2J+1}\sum|\mathcal{M}_T|^2 = \frac{4\pi}{2J+1}\sum_{\tau=0,1}\sum_{\tau'=0,1}\left\{R_M^{\tau\tau'}\left(v_T^{\perp 2},\frac{q^2}{m_N^2}\right)\ W_M^{\tau\tau'}(y) + \frac{q^2}{m_N^2}\left[R_{\Phi''}^{\tau\tau'}\left(v_T^{\perp 2},\frac{q^2}{m_N^2}\right)\ W_{\Phi''}^{\tau\tau'}(y) + R_{\Phi''M}^{\tau\tau'}\left(v_T^{\perp 2},\frac{q^2}{m_N^2}\right)\ W_{\Phi''M}^{\tau\tau'}(y)\right]\right\}. \tag{4.11}$$

4.3.1 Particle and nuclear response functions

The full set of DM response functions can be found in Appendix A of [103], but the list was limited to only those functions surviving for argon:

$$\begin{aligned}
R_M^{\tau\tau'}\left(v_T^{\perp 2},\frac{q^2}{m_N^2}\right) &= c_1^\tau c_1^{\tau'} + \frac{j_\chi(j_\chi+1)}{3}\left[\frac{q^2}{m_N^2}v_T^{\perp 2}c_5^\tau c_5^{\tau'} + v_T^{\perp 2}c_8^\tau c_8^{\tau'} + \frac{q^2}{m_N^2}c_{11}^\tau c_{11}^{\tau'}\right],\\
R_{\Phi''}^{\tau\tau'}\left(v_T^{\perp 2},\frac{q^2}{m_N^2}\right) &= \frac{q^2}{4m_N^2}c_3^\tau c_3^{\tau'} + \frac{j_\chi(j_\chi+1)}{12}\left(c_{12}^\tau - \frac{q^2}{m_N^2}c_{15}^\tau\right)\left(c_{12}^{\tau'} - \frac{q^2}{m_N^2}c_{15}^{\tau'}\right),\\
R_{\Phi''M}^{\tau\tau'}\left(v_T^{\perp 2},\frac{q^2}{m_N^2}\right) &= c_3^\tau c_1^{\tau'} + \frac{j_\chi(j_\chi+1)}{3}\left(c_{12}^\tau - \frac{q^2}{m_N^2}c_{15}^\tau\right)c_{11}^{\tau'}.
\end{aligned} \tag{4.12}$$

R_M contains the coefficients of SI effective operators $\mathcal{O}_1$ (c_1), besides, there are terms for other operators with additional dependencies on q^2 and/or $v_\perp^2$. Solely operators $\mathcal{O}_1$, $\mathcal{O}_3$, $\mathcal{O}_5$, $\mathcal{O}_8$, and $\mathcal{O}_{11}$ were considered in this study constraining an interaction at a time, hence the cross-terms and couplings greater than c_{11} were discarded. The W_k functions different from zero for ^{40}Ar were taken from [103]:

$$\begin{aligned}
W_M^{00}(y) &= e^{-2y}(31.8294 - 65.9618y + 48.5834y^2 - 15.194y^3 + 1.9036y^4 - 0.0595886y^5 \\
&\quad + 0.000544329y^6),\\
W_M^{11}(y) &= e^{-2y}(0.318304 - 1.06524y + 1.24846y^2 - 0.62249y^3 + 0.141618y^4 - 0.0138797y^5 \\
&\quad + 0.000480513y^6),\\
W_M^{10}(y) &= e^{-2y}(-3.18299 + 8.62425y - 8.02539y^2 + 3.19316y^3 - 0.554467y^4 + 0.0353797y^5 \\
&\quad - 0.000511426y^6),\\
W_M^{01}(y) &= e^{-2y}(-3.18299 + 8.62425y - 8.02539y^2 + 3.19316y^3 - 0.554467y^4 + 0.0353797y^5 \\
&\quad - 0.000511426y^6),\\
W_{\Phi''}^{00}(y) &= e^{-2y}(0.299629 - 0.373798y + 0.154895y^2 - 0.0238983y^3 + 0.00122474y^4),\\
W_{\Phi''}^{11}(y) &= e^{-2y}(0.00414999 - 0.0181474y + 0.0240755y^2 - 0.00926264y^3 + 0.00108115y^4),\\
W_{\Phi''}^{10}(y) &= e^{-2y}(-0.0352627 + 0.0990955y - 0.0683453y^2 + 0.0161561y^3 - 0.00115071y^4),\\
W_{\Phi''}^{01}(y) &= e^{-2y}(-0.0352627 + 0.0990955y - 0.0683453y^2 + 0.0161561y^3 - 0.00115071y^4),\\
W_{M\Phi''}^{00}(y) &= e^{-2y}(-3.08821 + 5.12625y - 2.89248y^2 + 0.653386y^3 - 0.0526576y^4
\end{aligned}$$

$$
\begin{aligned}
&+0.000816493y^5),\\
W^{11}_{M\Phi''}(y) &= e^{-2y}(-0.036345+0.140282y-0.171917y^2+0.0770456y^3-0.0134973y^4\\
&+0.000720769y^5),\\
W^{10}_{M\Phi''}(y) &= e^{-2y}(0.308826-0.709394y+0.515378y^2-0.153134y^3+0.0185641y^4\\
&-0.000767139y^5),\\
W^{01}_{M\Phi''}(y) &= e^{-2y}(0.363444-1.17124y+1.09117y^2-0.373592y^3+0.0452762y^4\\
&-0.000767139y^5).
\end{aligned}
\tag{4.13}
$$

Superscript's indexes indicate the isospin components and y was defined in Eq. 4.10. These nuclear response functions are different one-body multipole operators in the nuclear matrix element. They are constructed from the Bessel spherical harmonics and vector spherical harmonics with the shape shown in Fig. 4.2. For comparison, the Helm form factor is incorporated, which arises from calculating the Fourier transform of a charge distribution with spherical symmetry.

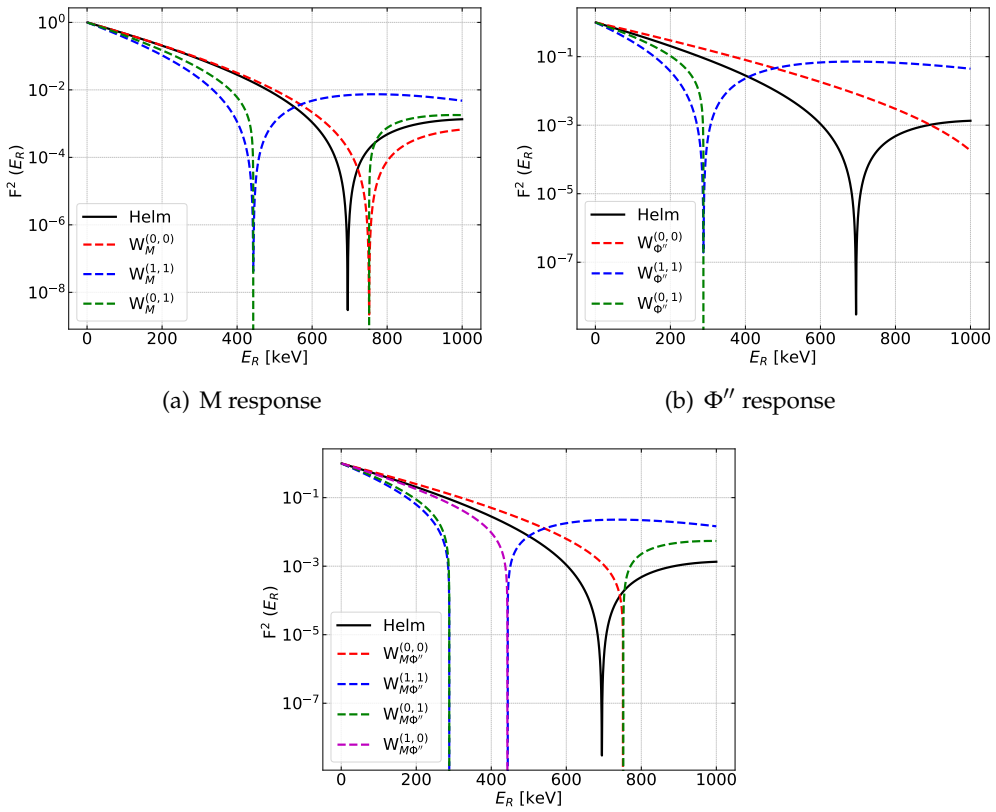

(a) M response

(b) Φ'' response

(c) M Φ'' response

FIGURE 4.2: Nuclear response functions for ^{40}Ar presented as form factors [106]: $F^2(E_R) = \frac{W_X^{(\tau,\tau\prime)}(y)}{W_X^{(\tau,\tau\prime)}(0)}$, with X = M, Φ'', MΦ''. The Helm form factor was included for comparison.

4.4 NREFT-derived specific interactions

The NREFT formalism incorporates more complex interactions. If the Standard Model (SM) photon is responsible for the DM-nucleon interaction, relevant cases arise from using a certain effective operator or combining some of them, e.g. anapole, electric or magnetic dipole, and millicharged DM.

4.4.1 DM with an anapole moment

The anapole moment is the lowest electromagnetic moment allowed for a Majorana[2] particle. It is generated by a toroidal electric current which confines the magnetic field within a torus; basically, it is equivalent to having a particle with a toroidal dipole moment.
If the DM particle is assumed to be a Majorana fermion scattering off a nucleus via a spin-1 mediator that kinetically mixes with the photon, then the effective interaction is written as:

$$\mathcal{L}_{\mathcal{A}} = c_{\mathcal{A}}\,\bar{\chi}\,\gamma^{\mu}\gamma^{5}\,\chi\,\partial^{\nu}\,F_{\mu\nu}\,, \tag{4.14}$$

where the χ spinor represents the Majorana DM particle, $c_{\mathcal{A}}$ the anapole moment coupling strength and $F_{\mu\nu}$ the electromagnetic field tensor. The anapole moment has a unique feature, it interacts only with external electromagnetic currents $\mathcal{J}_{\mu} = \partial^{\nu}F_{\mu\nu}$ [107].
In the non-relativistic limit, the effective operator for anapole interactions, $\mathcal{O}_{\mathcal{A}}$, is a linear combination of the momentum-independent operator $\mathcal{O}_8$ and the momentum-dependent $\mathcal{O}_9$:

$$\mathcal{O}_{\mathcal{A}} = c_{\mathcal{A}} \sum_{N=n,p} \left(Q_N\mathcal{O}_8 + g_N\mathcal{O}_9\right)\,, \tag{4.15}$$

where Q_N is the nucleon charge ($Q_p = e$, $Q_n = 0$) while g_N is the nucleon g-factor (g_p = 5.59 and g_n = -3.83). This interaction takes the next form for argon, $\mathcal{O}_{\mathcal{A}} = 2\,e\,c_{\mathcal{A}}\,\mathcal{O}_8$. It is possible to parametrize the coupling strength in terms of an anapolar effective cross-section as:

$$\sigma_{\mathcal{A}} = \frac{c_{\mathcal{A}}^2\,\mu_N^2}{\pi}\,. \tag{4.16}$$

4.4.2 DM with a magnetic dipole moment

Contact interactions ($|\vec{q}| \ll m_\phi$[3]) are independent on the exchanged momentum, however long-range interactions ($|\vec{q}| \gg m_\phi$) are enhanced at small momentum transfer. Examples of long-range interactions are: DM with electric or magnetic dipole moment and millicharged DM. These arise from the exchange of a massless mediator, whose propagator is responsible for the enhancement.
Considering the DM particle as a Dirac fermion[4] which acquires a magnetic dipole moment, then the effective interaction is given by:

$$\mathcal{L}_{\mathcal{MD}} = \frac{\mu_\chi}{2}\,\bar{\chi}\,\sigma^{\mu\nu}\chi\,F_{\mu\nu}\,, \tag{4.17}$$

[2] Majorana particles: particles that constitute their own antiparticle, e.g. photon.
[3] m_ϕ is the mediator mass.
[4] Dirac fermions: spin-½ particles with a different antiparticle, e.g. electron (positron).

here, the spinor χ is the Dirac DM particle, μ_χ is the magnetic moment coupling, $\sigma^{\mu\nu} = \frac{i}{2}[\gamma^\mu, \gamma^\nu]$ and $F_{\mu\nu}$ is the tensor of the electromagnetic field. Like in the anapole case, the non-relativistic shape of the effective operator for magnetic dipole interactions, $\mathcal{O}_{\mathcal{MD}}$, depends on the operators $\mathcal{O}_1$, $\mathcal{O}_5$, $\mathcal{O}_4$ and $\mathcal{O}_6$.

$$\mathcal{O}_{\mathcal{MD}} = 2\,e\,\mu_\chi \sum_{N=n,p} \left[Q_N\, m_N \mathcal{O}_1 + 4\, Q_N \frac{m_\chi m_N}{q^2} \mathcal{O}_5 + 2\, g_N\, m_\chi \left(\mathcal{O}_4 - \frac{1}{q^2}\mathcal{O}_6 \right) \right] \tag{4.18}$$

Likewise, the magnetic moment coupling can be used to obtain an effective cross-section:

$$\sigma_{\mathcal{MD}} = \frac{\mu_\chi^2\, \mu_N^2}{\pi}. \tag{4.19}$$

4.4.3 DM with millicharge

The interaction Lagrangian of the millicharged DM is given by:

$$\mathcal{L}_{\mathcal{M}} = e\,\epsilon_\chi\, A_\mu\, \bar{\chi}\, \gamma^\mu\, \chi\,, \tag{4.20}$$

where χ is a Dirac DM particle, A_μ is the SM photon, and ϵ_χ the millicharge (a fraction of the electron charge e). The non-relativistic millicharge operator, $\mathcal{O}_{\mathcal{M}}$, is only a function of the $\mathcal{O}_1$ operator but with a q^2 dependence:

$$\mathcal{O}_{\mathcal{M}} = e^2\, \epsilon_\chi\, \frac{\mathcal{O}_1}{q^2}. \tag{4.21}$$

4.4.4 DM with electric dipole moment

The effective Lagrangian for coupling of a Dirac fermion χ with an electric dipole moment d_χ to the electromagnetic field $F_{\mu\nu}$ is:

$$\mathcal{L}_{\mathcal{ED}} = \frac{d_\chi}{2}\, i\, \bar{\chi}\, \sigma^{\mu\nu} \gamma^5 \chi\, F_{\mu\nu}\,, \tag{4.22}$$

A DM particle with a permanent electric dipole moment must have a non-zero spin, also d_χ must satisfy time-reversal and parity violation [108]. The non-relativistic electric operator, $\mathcal{O}_{\mathcal{ED}}$, is a function of the $\mathcal{O}_{11}$ operator:

$$\mathcal{O}_{\mathcal{ED}} = 2\,e\,d_\chi\, \frac{\mathcal{O}_{11}}{q^2}. \tag{4.23}$$

4.5 The WIMpy_NREFT code

The Python-based WIMpy_NREFT code [109] determines DM-nucleus scattering rates in the framework of NREFT including operators from $\mathcal{O}_1$ to $\mathcal{O}_{11}$, as well as millicharged, magnetic dipole, and anapole interactions. In addition, it can be used to generate recoil spectra for multiple targets (Xe, Ar, C, Ge, I, F). WIMpy includes functionality to calculate directional recoil spectra, as well as signals from coherent neutrino-nucleus scattering (including neutrino fluxes from the Sun, atmosphere, and diffuse supernovae). By default, the code assumes a spin-1/2 DM particle.

4.5.1 Implementation and cross-check

To carry out this work, part of the WIMpy code was adapted and inserted into Maxpatch, a ROOT-based software to calculate upper limits in DEAP-3600. It was used the main function that computes the rate, named: `dRdE_NREFT()`. This function depends on the recoil energy, WIMP mass, coupling strength, atomic mass, and other astrophysical parameters with which the minimum speed, the momentum transfer, the integral of the VDF (η), the integral of the VDF with the transverse velocity (η^T), and the nuclear/particle physics responses are determined.

The code snippet was changed from Python to a C++ syntax and then added within the file `recoilrate.cc`, calling the `dRdE_NREFT()` function within the class: `RecoilRate_Isotropic`. For determining the strength of a specific coupling (e.g. c_1), the proton's coupling was linked to the variable `_sigma0_cm2` which is an output parameter in Maxpatch (it normally holds calculated cross-section values). The coupling to the proton was not exactly equal to `_sigma0_cm2` because the results were expressed in terms of effective cross-sections. Making use of an equation similar to Eq. 4.16 but solving for the $\mathcal{O}_1$ coupling: c_1, cross-section values in GeV^{-2} units were gotten, which multiplied by $(\hbar c)^2 = 389 \cdot 10^{-30}$ GeV$^2 \cdot$ cm^2 convert to cm^2. The relationship between the protons and neutrons coupling was also defined.

Additional changes were made to Maxpatch to specify the VDF file name, the effective operator, and couplings' ratio from the *config* file. This strategy enabled the mass-production of limits in ComputeCanada clusters by modifying each *config* file through a bash script. The Maxpatch code with NREFT implemented is password-protected (maxpatch_nreft). However, a class with the function to compute the differential rate is shown below. See Appendix A for details on the code for anapole, electric, magnetic and millicharge interactions.

```
double RecoilRate_Isotropic::get_recoilrate_at(double Er_keV){

 double _vE = get_velocity_profile()->get_vE();
 double sigmav= 156.0;

 double cn[11];
 double cp[11];

 for(int k=0;k<=10;k++){
    cn[k] = 0;
    cp[k] = 0;
    }

 double m_N = 0.9315;
 double mu  = (m_N*_Mwimp_GeV)/(m_N + _Mwimp_GeV);

 cp[_eff_ope -1] = sqrt(_sigma0_cm2*TMath::Pi())/mu;
 cn[_eff_ope -1] = _cn_cp_ratio*cp[_eff_ope -1];

 double rate = dRdE_NREFT(Er_keV,_Mwimp_GeV, cp, cn,_A,_vE, sigmav,_v_esc);
 return rate;
}
```

Another modified file `maxpatch.cc`, where lines 604 and 605 were commented inside the function `determine_sigma0()` and a new range for cross-section seed values $[10^{-30}, 10^{2}]$ cm^2 was established, in this way Maxpatch properly computes the nuclear recoil rates. The first thing reviewed was the agreement between the integral of the velocity distribution (η) from WIMpy (analytically obtained) and from Maxpatch (numerically obtained). Both were calculated using the same astrophysical parameters and Fig. 4.3 shows a reasonable match between the curves. A general cross-check was done analyzing the differential rate which encloses all used functions, as shows Fig. 4.4 for operators $\mathcal{O}_1$ and $\mathcal{O}_5$ which are η- and η^T-dependent, respectively.

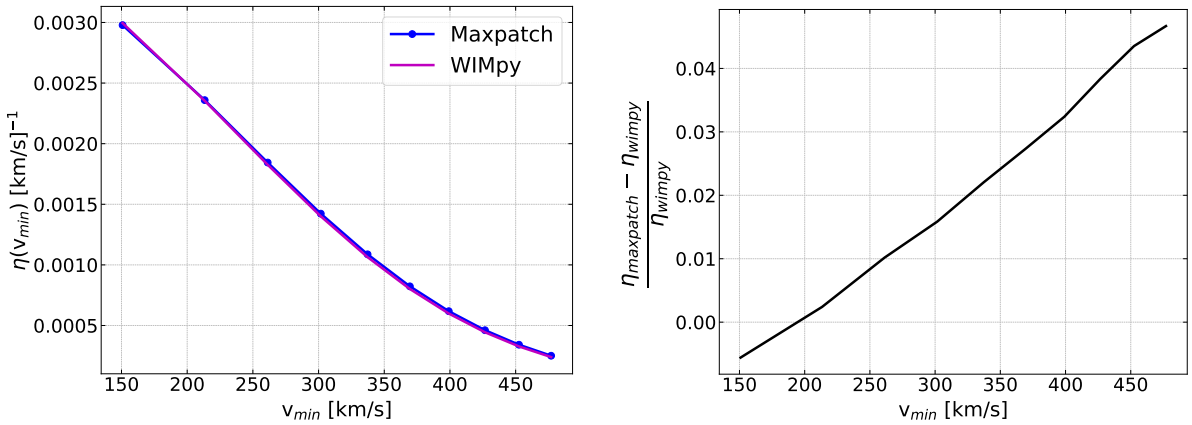

(a) (b)

FIGURE 4.3: a) Cross-check of the SHM VDF integration (η), where WIMPy refers to analytically calculated and Maxpatch to numerically. b) Relative difference between η approaches.

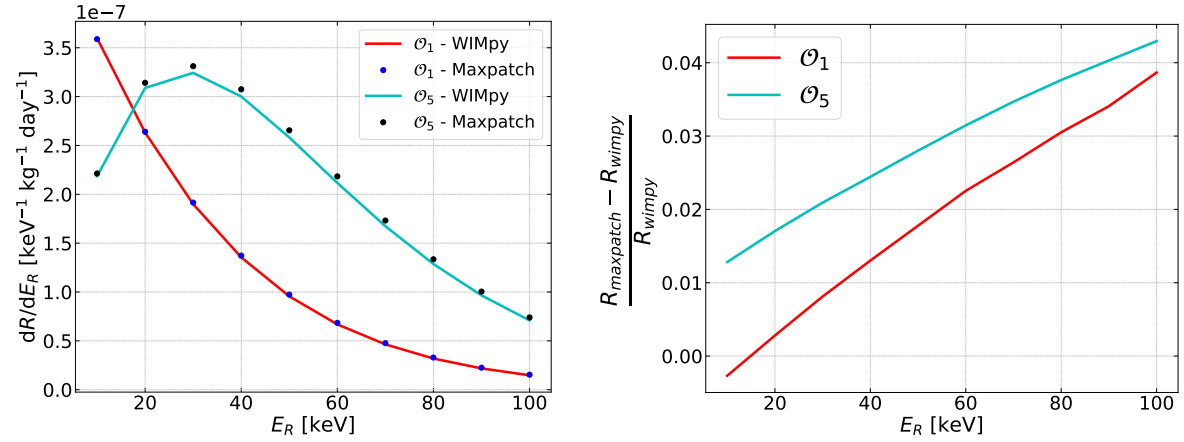

(a) (b)

FIGURE 4.4: a) Agreement between differential rates from WIMpy and Maxpatch for two effective operators: $\mathcal{O}_1$ and $\mathcal{O}_5$. The $\mathcal{O}_5$ curve was scaled by a factor of 3×10^9. b) Relative difference for the rates.

VDFs were determined from numerical simulations (Section 5.8), hence the output was a set of data-points. As WIMpy had uniquely defined the analytical integration of the SHM VDF, the explicit mathematical expression of η^T to perform its numerical integration in Maxpatch was implemented . Eq. 4.24 is the result, where equations $v_\perp^2 = v^2 - \frac{q^2}{\mu_N^2}$ and $v_{min} = \frac{q}{\mu_N}$ were utilized.

$$\eta^T = \int \frac{f(v)}{v}\, v_\perp^2\, v^2\, dv\, d(cos\,\theta)\, d\phi = 4\pi \int [f(v)\, v^3 - v_{min}^2 f(v)\, v]\, dv \tag{4.24}$$

Because the speed distributions are generated directly, doing the substitution $f'(v) = f(v)v^2$ in Eq. 4.24, gave the Eq. 4.25 which acceptably reproduces WIMpy's results (Fig. 4.5).

$$\eta^T = \int [f'(v)\, v - v_{min}^2 .f'(v)/v]\, dv \tag{4.25}$$

For η the expression transforms into:

$$\eta = \int \frac{f'(v)}{v}\, dv \tag{4.26}$$

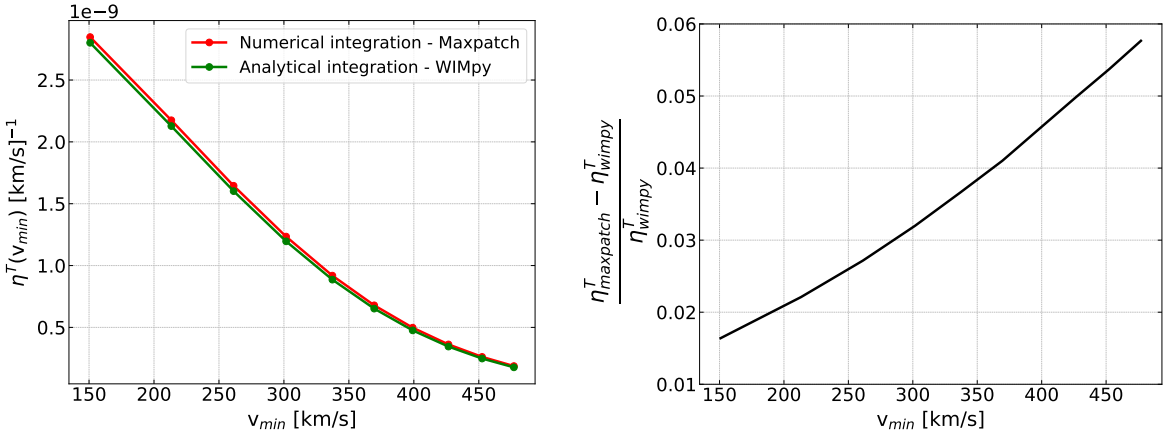

(a) (b)

FIGURE 4.5: a) Agreement between the analytical and numerical integration of η^T for the SHM VDF. b) Relative difference among η^T approaches.

This mismatch of < 6% is associated with differences in the methods utilized for implementing the VDF. The cross-check for specific interactions of DM appear in Fig. 4.6.

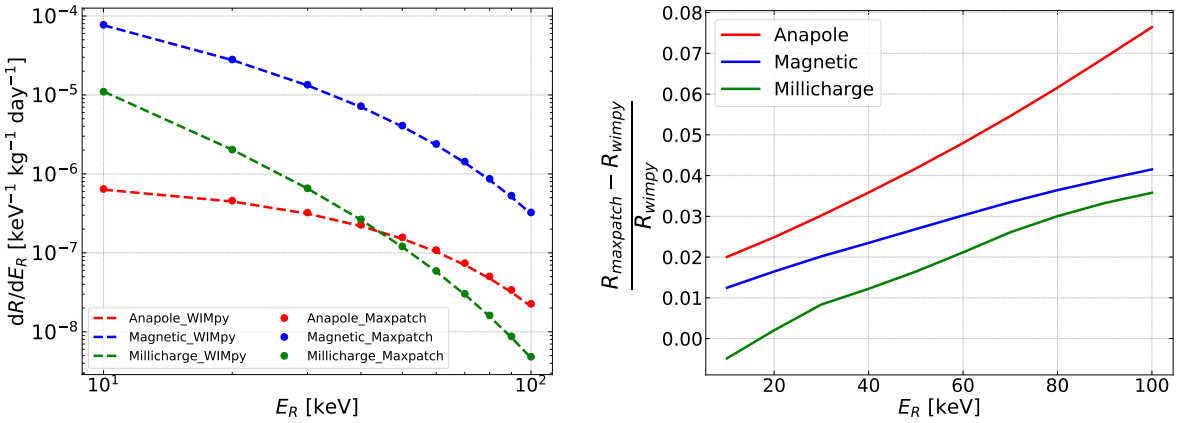

(a) (b)

FIGURE 4.6: a) Agreement between specific interactions from WIMpy and Maxpatch. b) Relative difference for specific interactions.

Chapter 5

Non-thermal halo components

The Velocity Distribution Function (VDF) describes all possible velocities of DM particles in the MW halo. The tail of this distribution[1] provides valuable information about the merging history of the halo and it can significantly modify the exclusion limits. Most direct-detection experiments utilize a Maxwell-Boltzmann distribution.
Recently, non-thermal stellar populations (substructures) have been discovered around the Sun by astronomical surveys [17, 110–113] which could have DM associated, this fact would change the perspective of the VDF shape. Thus, a reasonable approach can be to infer the contribution of non-thermal DM halo components to the VDF by using non-thermal stellar structures. Here, *non-thermal* refers to objects (e.g. stars/DM particles) with a different velocity distribution than that of virialized (stable) components of the halo.
The *Gaia* satellite [114] has provided an amazing dataset of astrometry of about 1 billion stars in Earth's neighborhood which is cross-matched with the Sloan Digital Sky Survey (SDSS) optical telescope [115]. Within the second *Gaia* catalogue[2] substructures like the *Gaia Sausage*, *Nyx* stream and new *Helmi* stream members were identified. These types of substructures could be classified based on whether their spatial and velocity distributions have virialized, divided into the following categories [13]: (1) Relaxed halo: virialized in space and velocity, (2) Debris flows: virialized in velocity but not space, and (3) Streams: virialized in neither velocity nor in space. In some simulations of mergers there is evidence that in debris flows, DM follows stars very closely. Streams also have a significant correlation, but much weaker than debris flows, so there is more uncertainty. In this chapter, after introducing the Standard Halo Model, a brief description of diverse substructures will be presented with the steps followed for their modeling.

5.1 Standard Halo Model (SHM)

The Standard Halo Model [21] includes a set of astrophysical assumptions entering in the calculation of quantities related to DM experiments. It is a simplified model that considers the Milky Way halo isotropic, virialized, without substructures, and in hydrostatic equilibrium. The velocity of particles in SHM is described by a Maxwellian velocity distribution (Eq. 5.2) truncated at the escape velocity to guarantee the DM particles are gravitationally bound to the galaxy. Its density profile is a function of the galactic radius following $\rho \propto 1/r^2$, and different models have been developed (e.g. NFW, Einasto, Burkert). Classical parameters of the SHM are the

[1] Subhalos falling into the MW galaxy are tidally disrupted and leave behind out-of-equilibrium remnants. DM particles in these remnants likely have higher speeds compared to the rest of the halo and thus contribute to the high-velocity tail of the velocity distribution. Therefore, the shape of the high-velocity end of the distribution depends on the size and time of minor mergers in the MW galaxy [100].
[2] Gaia Data Release 2 (Gaia DR2) (2018)

local DM density ($\rho_0 = 0.3$ GeV/cm^3), the circular speed ($v_c = 220$ km/s), and the escape speed ($v_{esc} = 544$ km/s), all of them with uncertainties extensively discussed [116–118]. Even when direct-detection experiments use the SHM as a way to compare the results between them, some studies suggest it should be updated to include new data-driven features [2, 21, 113]. New recommended values are [21, 119]: $\rho_0 = 0.55 \pm 0.17$ GeV/cm^3, $v_c = 233 \pm 3$ km/s, $v_{esc} = 528^{+24}_{-25}$ km/s. It worth to mention that is the uncertainty on ρ_0 what could affect exclusion limits most significantly as well as the velocity distribution employed.

5.2 Gaia Sausage

Studies of our stellar halo chemo-dynamical structure [120–122] have revealed that its velocity ellipsoid exhibits two main components: a metal-poor group of stars with isotropic feature associated with the ancient, relaxed/round halo; and the other is a more metal-rich group with high radial anisotropy. This object is a debris flow and was labeled as *Gaia Enceladus* or *Gaia Sausage* (GS) after its flattened and elongated shape in velocity space (Fig. 5.1). It is believed that it was the result of a major head-on collision between a large dwarf galaxy and the MW approximately 8-10 billion years ago. Likely, the dwarf galaxy would be accompanied by a DM fraction.

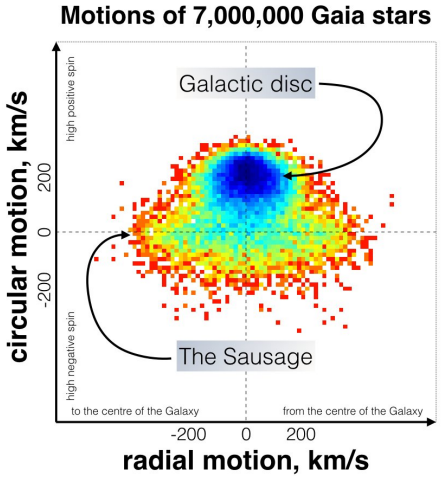

FIGURE 5.1: GS location in the velocity space. The galactic disc stars rotate around the center of the MW with a speed of $\sim$ 220 km/s, while the stars making up the *Sausage* have negligible circular velocity, but they zoom back and forth in the radial direction with a speed of almost twice as high, close to $\sim$ 400 km/s [123].

5.2.1 VDF modelling

This subsection presents how to model the GS VDF. The same procedure was followed with the other substructures. The analytic velocity distribution (in the galactic reference frame[3]) capturing the generic features of two components, a round halo (SHM) and the *Sausage* (Sub), is represented by:

[3] The Earth/Lab frame expression was obtained through a Galilean transformation: $\vec{v} \to \vec{v} - \vec{v}_E$, with $\vec{v}_E$ defined in Eq.4.2.

$$f_\chi(\vec{v}) = (1 - \eta_{sub})\, f_{\rm SHM}(\vec{v}) + \eta_{sub}\, f_{\rm Sub}(\vec{v})\,, \tag{5.1}$$

where the term $\eta_{sub} = \rho_{sub}/\rho_0$ (ρ_{sub}: substructure DM density) describes the DM fraction of the substructure at the solar neighbourhood, $f_{\rm SHM}$ is the velocity distribution of a nearly round dark halo dominating the gravitational potential in the innermost 20 kpc, and $f_{\rm Sub}$ is the velocity distribution of the substructure. The $f_{\rm SHM}$ function is an isotropic Gaussian [21]:

$$f_{\rm SHM}(\vec{v}) = \frac{1}{(2\pi\sigma_v^2)^{3/2} N_{\rm SHM}} \exp\left(-\frac{|\vec{v}|^2}{2\sigma_v^2}\right) \times \Theta(v_{\rm esc} - |\vec{v}|)\,, \tag{5.2}$$

with $\sigma_v = v_0/\sqrt{2}$ as the isotropic velocity dispersion, $N_{\rm SHM}$ a normalization constant and Θ a Heaviside step function which establishes a cutoff at the galactic escape speed. While $f_{\rm Sub}$ is characterized by means of a three-dimensional Gaussian distribution:

$$f_{\rm Sub}(\vec{v}) = \frac{1}{(8\pi^3 \det \boldsymbol{\sigma}^2)^{1/2} N_{\rm Sub}} \exp\left[-(\vec{v} - \vec{\mu}_{\rm S})^T \frac{\boldsymbol{\sigma}^{-2}}{2} (\vec{v} - \vec{\mu}_{\rm S})\right] \times \Theta\Big(v_{esc} - |\vec{v} - \vec{\mu}_{\rm S}|\Big)\,, \tag{5.3}$$

here, $\boldsymbol{\sigma}^2 = {\rm diag}(\sigma_r^2, \sigma_\theta^2, \sigma_\phi^2)$ is the velocity dispersion tensor diagonalised in spherical polar coordinates, $N_{\rm Sub}$ is a normalization constant and $\vec{\mu}_{\rm S}$ acts as the substructure mean velocity, $\vec{\mu}_{\rm S} = (v_r, v_\theta, v_\phi)$.
In order to get f_χ (Eq. 5.1), considering O'Hare's model [113], the next steps were followed:

1. First of all, a *Jupyter Notebook*[4] project was created loading all the necessary Python libraries. Note: SHM values are assumed when creating the VDFs along with (U,V,W) values reported in [20].

2. For $f_{SHM}(\vec{v})$, 20 millions DM particles were simulated in velocity space using the Python function `numpy.random.multivariate_normal()` which draws random samples from a multivariate Gaussian distribution. It was specified by its mean[5] ($\vec{\mu}_{\rm S}$ = [0,0,0]) and diagonal covariance matrix[6], $\boldsymbol{\sigma}$ = diag(σ_v, σ_v, σ_v).

3. Once generated the "dark" points, its velocity coordinates (v_r,v_θ,v_ϕ) are used for computing each velocity module or speed, $v = |\mathbf{v}| = \sqrt{v_r^2 + v_\theta^2 + v_\phi^2}$.

4. Later, the escape velocity cut-off constraint was applied to the dataset with speed values for ensuring $v < v_{esc}$, which gave another reduced dataset $(v_r,v_\theta,v_\phi)_{red}$ corresponding to those v values satisfying the condition.

5. Filtered speed values were boosted to the Earth/Lab frame effecting a Galilean transformation. Instead of considering the velocity modulation through the year, a value on March 9$^{\rm th}$ for the Earth's orbital velocity around the Sun, $\bar{v}_{\rm O}$ = (29.4, -0.11, 5.90) km/s, provided an equivalent time-averaged result [113].

$$(v_r, v_\theta, v_\phi)_{lab} = (v_r, v_\theta, v_\phi)_{red} - \vec{v}_E \tag{5.4}$$

$$(v_r, v_\theta, v_\phi)_{lab} = (v_r, v_\theta, v_\phi)_{red} - \big[(0, 0, v_0) + (\rm U, V, W) + \bar{v}_{\rm O}\big] \tag{5.5}$$

[4] https://jupyter.org/
[5] Mean: a coordinate in N-dimensional space, it represents the place where samples are most likely to be generated.
[6] Covariance indicates the level to which two or more variables vary together.

6. With $(v_r, v_\theta, v_\phi)_{lab}$ information, lab-frame speed values were recalculated (as in step 3) and inserted into a one-dimensional normalized histogram, fixing the range and bin number to produce equal bin size.

7. Such histogram already shows the shape of the VDF for SHM. The histogram's PDF (Probability Density Function) provided data-points [v, f(v)] describing $f_{\rm SHM}(\vec{v})$.

8. Basically, the former procedure (steps 2-6) was replicated with $f_{\rm Sub}(\vec{v})$ but now choosing the properties of the substructure, $\vec{\mu}_{\rm S}$ and $\boldsymbol{\sigma}$ = diag(σ_r, σ_θ, σ_ϕ), appearing in Table 5.1. At the end, a set of data-points for $f_{\rm Sub}(\vec{v})$ was obtained as well.

9. Remains to sum both VDF components[7] as indicated in Eq. 5.1, weighting each part with a certain fraction of DM related to η_{sub}, see Table 5.1. The sum was done solely over the Y-axis or f(v) values, since the X-axis (v) did not change because both histograms had the same range and binning. To conclude, $f_\chi(\vec{v})$ is exported as .txt and .root formats which are later loaded for plotting or computing limits in Maxpatch. The *Sausage* VDF following this strategy is in Fig. 5.2 with a SHM VDF for comparison.

A second attempt for describing $f_\chi(\vec{v})$ of the GS was included. Necib *et.al.*[13] obtained a VDF from the observed properties of the accreted stellar population near the Sun by properly accounting for the ratio of stars to DM contributed by individual mergers. Based on *Gaia* DR2 data, they estimated a $\sim$ 42% of DM in the debris flow [13]. Its independent SHM and GS data files were used with some η_{sub}, which gave a different VDF realization for this substructure as illustrated in Fig. 5.2. The dataset is available on the website [124].

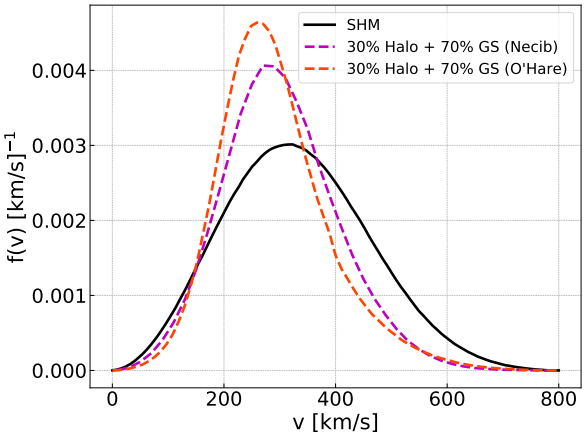

FIGURE 5.2: *Gaia Sausage* models. O'Hare's VDF was created with the previous numerical approach whereas Necib's uses data files from [124]. η_{sub} was constrained to be $\leq$ 20% in [21] whilst a mean value of 42^{+26}_{-22} % was estimated in [13]. To cover all possibilities η_{sub} was spanned up to a 70%.

5.3 S1 stream

The S1 stellar stream (Fig. 5.3), also derived from Gaia-SDSS data, is a remnant containing about 94 member stars impacting almost head-on the Solar System at very high speed ($v \sim 500$ km/s), a.k.a the *Dark Matter Hurricane* [20, 111, 125]. The progenitor of the S1 stream is believed to have

[7] In strict sense, it is the speed distributions of dark matter particles.

had a total mass of approximately 10^{10} $M_\odot$ (solar masses), comparable to the Fornax galaxy which is the largest surviving dwarf spheroidal satellite of the MW. If this prediction is true then the S1 stellar stream must be accompanied by a considerable DM remnant.

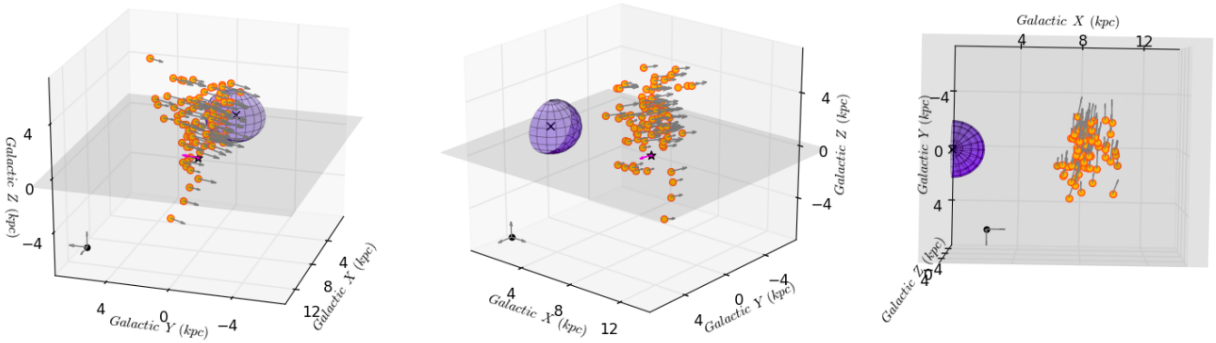

FIGURE 5.3: Different views of the S1 stream (orange circles) in galactic coordinates. The arrows show the total velocity of the S1 stars and the Sun's motion is marked as a star with a magenta arrow. A 2 kpc radius sphere and the grey plane represent the bulge and galactic plane. The Sun lies in the path of the counter-rotating S1 stars. Figure from [111].

Fig. 5.4 shows the velocity distribution modeled for S1 stream.

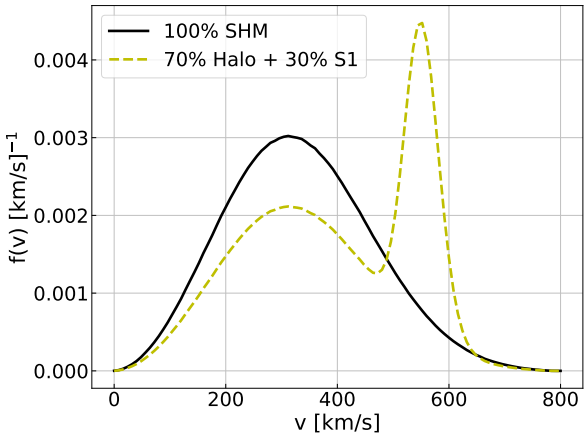

FIGURE 5.4: VDF corresponding to the S1 stream. The halo component was weighted with 70% of DM while S1 with 30%. Notice that setting η_{sub} = 0%, the VDF recovers the SHM velocity distribution (Maxwell-Boltzmann). A significant fraction of high-speed DM particles is in the tail of S1 VDF what indicates it is likely a recent merger of the MW's halo.

5.4 Nyx stream

Nyx is a new stellar stream found in the solar vicinity (Fig. 5.5). A population of about 500 stars was identified in this stream using a catalog of accreted stars built by applying deep learning algorithms to *Gaia* DR2 dataset [126]. Nyx stars concentrate within ±2 kpc of the galactic midplane and span in a radial range of 6.5-9.5 kpc, its kinematics are also distinct from the thin and thick disk of the halo. It was deduced that Nyx stars have a peak metallicity of [Fe/H] ∼ -0.5 and age ∼ 10–13 Gyr. The most solid interpretation favors Nyx as a remnant of a disrupted dwarf galaxy, but it could also be a perturbation of the MW disk.

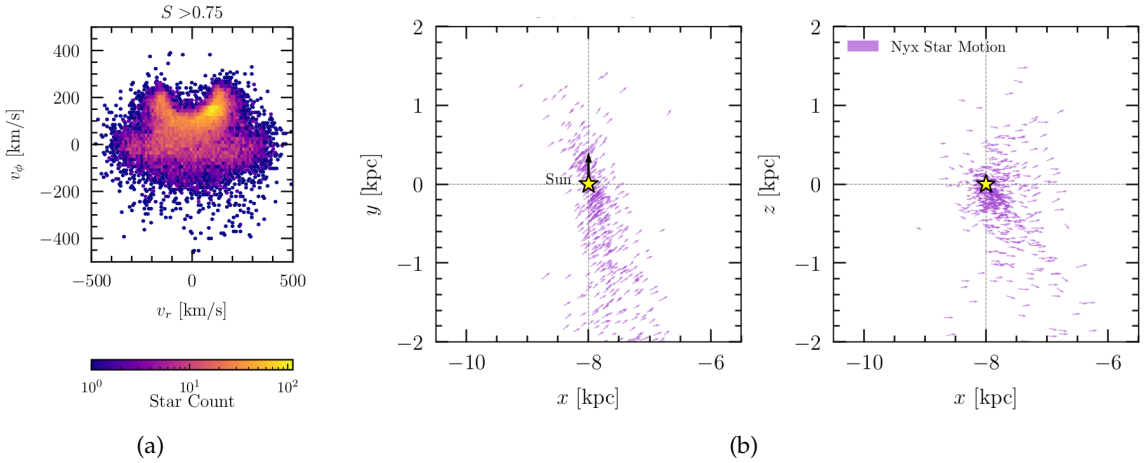

FIGURE 5.5: a) Nyx stream (crescent moon shape) in the space of spherical galactocentric velocity coordinates $v_r - v_\phi$. Here, S is a cut parameter indicating the probability of stars being accreted. b) Velocity of Nyx stars in the galactic xy and xz plane, with z orthogonal to the disk. The Sun motion is indicated by the yellow star and the black arrow. Figures from [17, 126].

Fig. 5.6 shows the VDF associated to Nyx stream with the parameters describing it in Table 5.1.

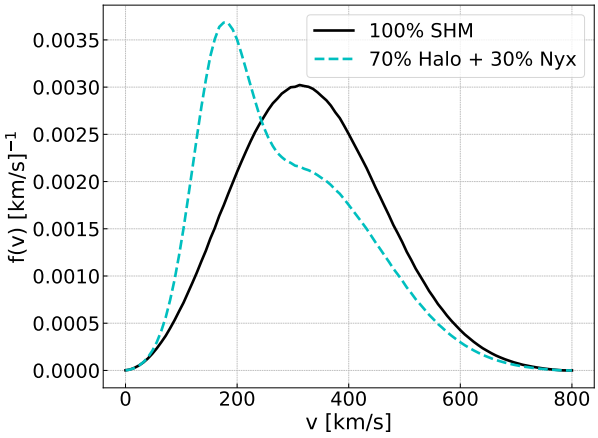

FIGURE 5.6: VDF corresponding to the Nyx stream with a 30% of DM.

5.5 Helmi streams

Helmi streams are clumps of stars crossing the solar neighborhood and detected since the 90's using Hipparcos proper motions combined with ground-based radial velocities [127]. Follow-up works estimated these streams were part of the tidal debris of a dwarf galaxy accreted 6-9 Gyr ago, based on the bimodality of the z-velocity distribution. This bimodal distribution is the distinctive feature of multiple wraps of tidal debris passing through the solar vicinity. The structure S2 from [111], consisting of $\sim$ 61 stars, is related to the Helmi streams. Lately, in [128] nearly 600 new members of the Helmi streams were reported (Fig. 5.7). Their Hertzsprung–Russell (HR) diagram reveals a broad age range, from approximately 11 to 13 Gyr, while their metallicity distribution goes from -2.3 to -1.0, and peaks at [Fe/H] $\sim$ -1.5 [128]. These findings confirm

the streams originated in a dwarf galaxy. The debris from the Helmi streams is an important donor to the MW halo, contributing approximately 15% of its mass in field stars.

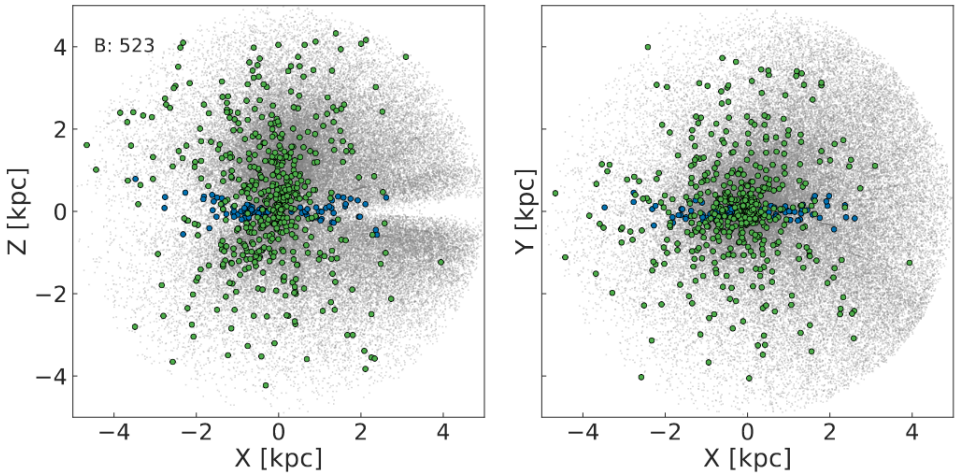

FIGURE 5.7: Spatial distribution of stars in Helmi streams for XZ and XY planes. The stream members are indicated with green circles, local halo stars are shown in the background with grey symbols. The total number of members is shown in the top left corner and tentative members are described with blue color [128].

Fig. 5.8 presents the VDF implementation for Helmi stream assuming the values in Table 5.1.

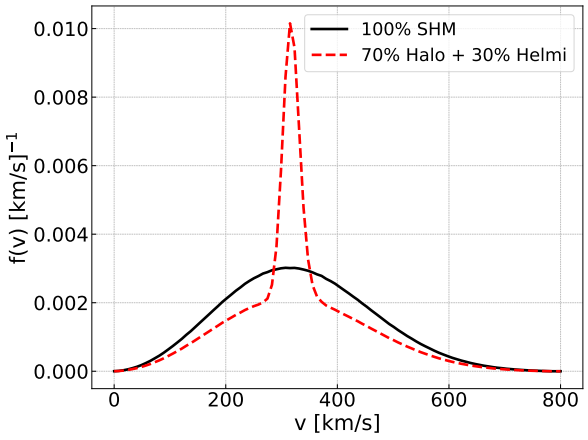

FIGURE 5.8: VDF corresponding to the Helmi stream with a 30% of DM.

5.6 Koppelman streams

Koppelman 1 (Kop1) and Koppelman 2 (Kop2) are a pair of stellar streams with retrograde motion identified in the solar neighborhood, which appear to be from relatively recent accretion events [129]. Their parameterizations in this study are from [17]. As it will be discussed later, the substructures VDF analyzed tend to form groups with similar effects on the results, therefore Kop1 was selected as their group representative while for the group containing Kop2, the S1 stream was chosen because its properties have been better documented.

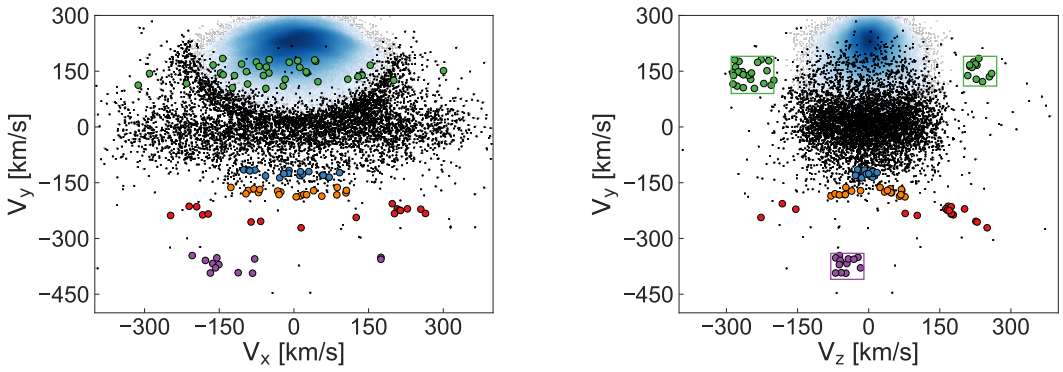

(a) (b)

FIGURE 5.9: Distribution of Kop1 (magenta circles) and Kop 2 (red circles) streams in velocity spaces $V_X V_Y$ (a) and $V_Z V_Y$ (b), they are characterized by being fast substructures. Helmi stream members are also represented with green circles. Black dots are other halo stars and the blue density maps the velocity distributions of all stars within 1 kpc from the Sun. Figures from [129].

Fig. 5.10 indicates the velocity distribution models associated to Kop1 and Kop2 streams.

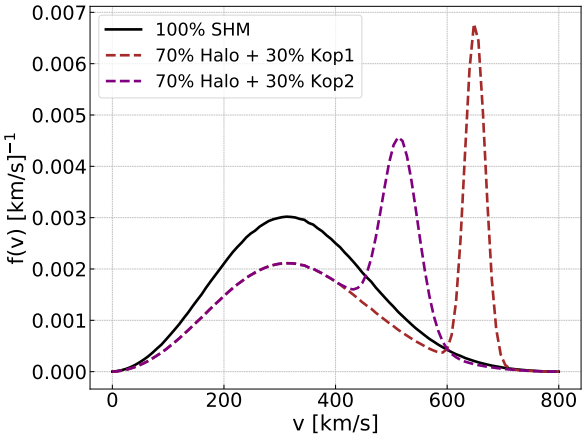

FIGURE 5.10: VDF for Koppelman streams with a 30% of DM. Kop1 was chosen for further analysis.

5.7 In-falling Clumps

A generic model of *In-falling Clumps* (ICs) to represent extra-galactic DM accreted into the MW was considered and is not described by observed streams. Such ICs may arise from past merger events or intergalactic DM continually falling into the MW, as motivated by models of hierarchical galaxy formation. They have been proposed by several authors [18, 19, 130–133]. To investigate the effects of ICs, a galactic-frame VDF is assumed as described by Eq. 5.3 with mean velocity $\vec{\mu}_S = (v_r, v_\theta, v_\phi)$ and dispersion tensor $\boldsymbol{\sigma} = \text{diag}(\sigma_r, \sigma_\theta, \sigma_\phi)$ given in galactocentric spherical coordinates, with r pointing towards the center of the galaxy, θ describing the zenith angle, and ϕ oriented with the disk rotation, and components given by,

$$
\begin{aligned}
v_\phi &= |\vec{v}| \cos\alpha \\
v_r = v_\theta &= \frac{1}{\sqrt{2}} |\vec{v}| \sin\alpha \\
\sigma_\phi &= \sigma_{||} \cos\alpha + \sigma_\perp \sin\alpha \\
\sigma_r = \sigma_\theta &= \frac{1}{\sqrt{2}} \left(\sigma_{||} \sin\alpha - \sigma_\perp \cos\alpha\right)
\end{aligned}
\tag{5.6}
$$

where $|\vec{v}|$ is the magnitude of the mean velocity vector, α is the angle between this vector and the motion of the Earth, $\sigma_{||}$ is the dispersion of the IC parallel to the Earth's velocity, and $\sigma_\perp$ is the dispersion in the perpendicular directions. To reduce the number of parameters being considered, components of the mean velocity and dispersion tensor that are perpendicular to the Earth's motion equal to each other were chosen. While this equality is not guaranteed to be the case for a generic VDF, a temporally-averaged direct-detection experiment insensitive to recoil direction is only sensitive to a DM particle's speed and the fraction of the velocity parallel to the Earth's motion. This direction-dependence is due to the boost the particles receive when transforming from the galactic-frame to the Earth-frame. Changing the partitioning of the velocity between the r- and ϕ-directions has a negligible impact on the resulting exclusion curves.

ICs were considered with 27 combinations (Fig. 5.11(a)) of $\alpha \in \{0, \pi/2, \pi\}$, $|\vec{v}| \in \{200, 300, 400\}$ km/s, and $\sigma_{||} \in \{10, 30, 50\}$ km/s, with $\sigma_\perp$ fixed to 50 km/s, chosen as a typical value from the range of streams considered in Table 5.1. The three values chosen for α correspond to ICs that enter the galaxy in prograde, perpendicular, or retrograde directions. Total speeds below the escape velocity were considered, with the understanding that some energy would be lost to dynamical friction as the ICs accreted into the galaxy. Values for $\sigma_{||}$ were investigated less than or equal to $\sigma_\perp$ under the assumptions that tidal forces will elongate streams and decrease the dispersion in that direction. Fig. 5.11(b) shows velocity distributions for the two ICs selected.

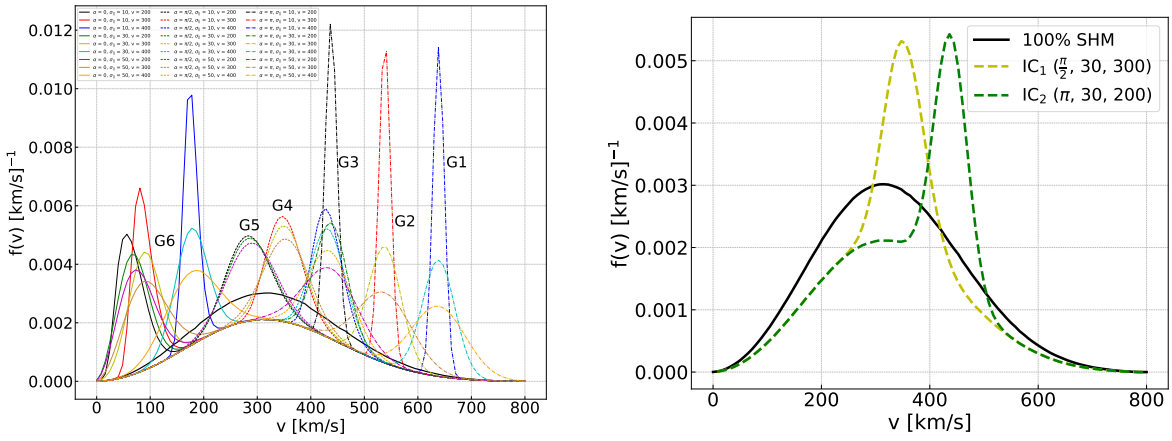

(a) (b)

FIGURE 5.11: a) Velocity distributions of 27 ICs combinations explored with 30% of DM. As the VDFs tend to form groups, they were classified from G1 to G6. The two VDF groups with the lowest mean were labeled as one (G6) since all curves produce the same exclusion limit. b) Selected IC VDF representatives for groups G3 (green) and G4 (yellow), the other IC's groups matched with any of the previously introduced velocity distributions, so they were used instead.

5.8 Summary of the substructures properties

A compendium of the substructures' characteristics is given in Table 5.1. It is important to recall that the kinematic features of the stellar streams were used to trace possible DM components, although there are large uncertainties on interpreting the stellar tracers for streams. Even though most substructures have been reported with few member stars, there could be more not yet catalogued, or the accreted DM may also greatly out-weight the accreted stars.
Regarding the DM fraction of the substructures, in the literature diverse values are reported. Authors from [20] used the DM density of the S1 stream as a free parameter ranging it up to 100% ρ_0. On the other hand, in [21] authors constrained such fraction for the GS to be 10% - 30%, with preferred value of 20% and it was also argued in [113]; whilst Necib *et.al.*[13] estimated a mean value of 42^{+26}_{-22} %. Because this parameter η_{sub} is unknown and its overall impact on DEAP-3600 limits seemed more relevant, $\eta_{sub} \leq 30\%$ was set for most of the substructures and $\eta_{sub} \leq 70\%$ for the GS models, this way a broad range of possibilities is covered.

TABLE 5.1: Summary of substructures considered. The mean velocity vector for each galactic-frame VDF is given as $\vec{\mu}_S = (v_r, v_\theta, v_\phi)$ [km/s], and the dispersion tensor as $\boldsymbol{\sigma} = \text{diag}\,(\sigma_r, \sigma_\theta, \sigma_\phi)$ [km/s]. The mass fraction of the local DM in each substructure is $\eta_{sub} = \rho_{sub}/\rho_0$, with $\rho_0 = 0.3$ GeV/(c^2 cm^3). The classification of substructures follows as: debris flow (GS), streams (S1, Nyx, Hel, Kop1) and in-falling clumps (IC). For *Gaia Sausages*, GS_1 refers to Necib's files from Github and GS_2 to O'Hare's VDF numerically implemented. To model Kop1 and Helmi VDFs, the central value of the dispersion components was used.

Group	Subs.	v_r	v_θ	v_ϕ	σ_r	σ_θ	σ_ϕ	η_{sub}
GS_1	Necib	—	—	—	—	—	—	0-70%
GS_2	O'Hare	-8.2	0.99	25.7	158.9	80.9	61.5	0-70%
G1	Kop1	-169	-59	-375	11-37	3-16	6-28	0-30%
G2	S1	-29.6	-72.8	-297.4	82.6	58.5	26.9	0-30%
G3	IC_2	0	0	200	35.4	35.4	30	0-30%
G4	IC_1	212.1	212.1	0	21.2	21.2	50	0-30%
G5	Hel	29	-287	141	37 - 83	6 - 21	4 - 15	0-30%
G6	Nyx	$156.8^{+2.1}_{-2.2}$	$-1.4^{+3.1}_{-3.0}$	$141.0^{+2.5}_{-2.6}$	$46.9^{+1.7}_{-1.6}$	$70.9^{+2.4}_{-2.2}$	$52.5^{+1.8}_{-1.8}$	0-30%

Chapter 6

Results and discussion

This chapter presents the results of the research as well as an assessment of them. Content includes: velocity distributions modeled, recoil energy spectra, constraints on effective operators for substructures, isospin scenarios, specific interactions, and finally the propagation of uncertainties.

6.1 Velocity distributions modeled

All VDF models discussed in the previous chapter distribute over the velocity range 1–800 km/s. Interestingly, when they are overlapped tend to form groups that are characterized just by choosing a representative VDF. Fig. 5.11(a) is a clear example of the VDF clustering, where a label was utilized for identifying each group. Fig. 6.1 contains the velocity distributions used for this analysis going from the fastest distribution (Kop1) to the slowest one (Nyx). They were modeled with the following proportion of DM: 70% Halo + 30% Substructure, and the two GS realizations with 30% Halo + 70% GS. Table 6.1 summarizes the SHM values, some of them were input parameters when modeling the VDFs.

TABLE 6.1: Parameters used for describing the SHM: local DM density, circular velocity at the Sun's position, Sun's peculiar velocity, and the escape speed of the Milky Way, respectively. Vectors are given as (v_r, v_θ, v_ϕ) with r pointing radially inward and ϕ in the direction of the Sun's motion.

Parameter	Value	Ref.
ρ_0	0.3 GeV/cm^3	[56]
$\vec{v}_c$	(0, 0, 220) km/s	[117]
$\vec{v}_{pec}$	(11.1, 12.24, 7.25) km/s	[20]
$v_{\rm esc}$	544 km/s	[134]

For slow VDFs (e.g. G6 group) most of the DM particles have $v < v_{min}$ and therefore would not create an observable nuclear recoil. Fig. 6.2 includes the result of integrating all these VDFs as function of v_{min} for η and η^T. The ideal case is to have a small v_{min} magnitude because it serves as the lower integration limit of the VDFs and would allow integrating a bigger area which translates into a higher event rate.

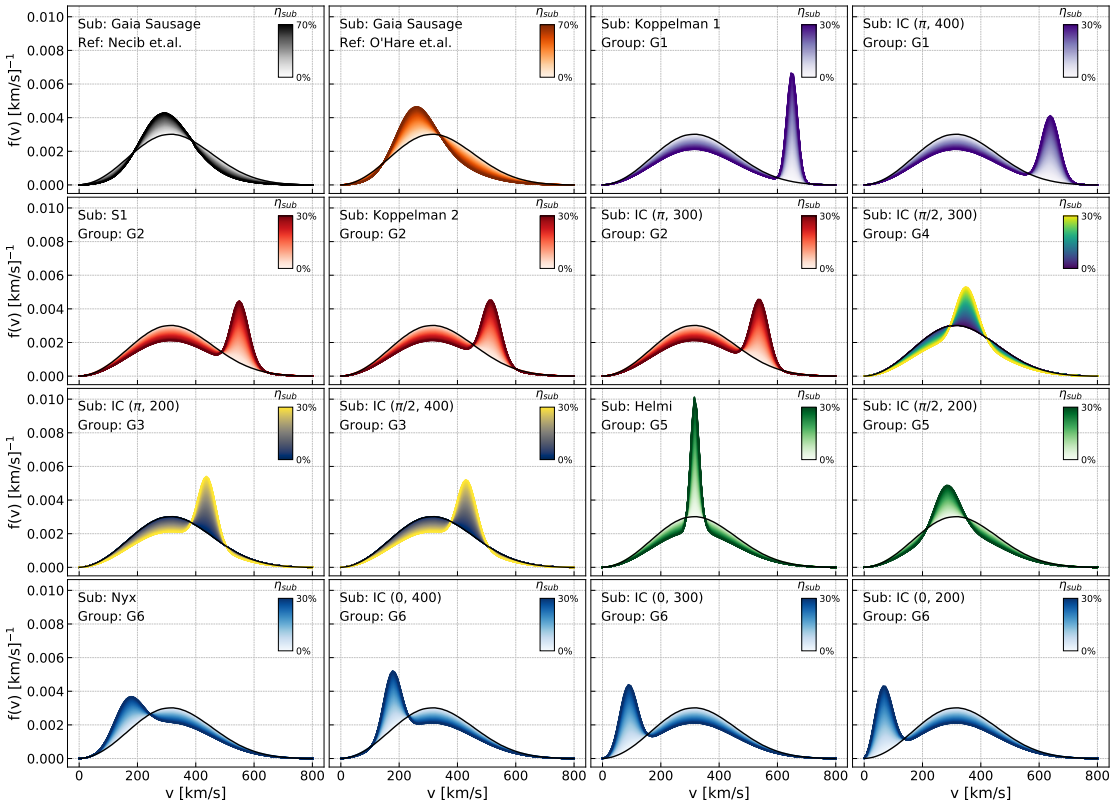

FIGURE 6.1: Velocity distributions modeled for this analysis. They were arranged by groups from G1 to G6 with the GS models labeled as independent. The first substructure listed in each group marks the chosen representative: G1 = Kop1, G2 = S1, G3 = IC(π, 200) , G4 = IC($\pi/2$, 300), G5 = Helmi, and G6 = Nyx. The color gradient indicates the relative DM density in each substructure, varying from 0% (light) to 30% (dark), with the exception of the two GS models, which go up to 70%. The solid black line corresponds to the SHM.

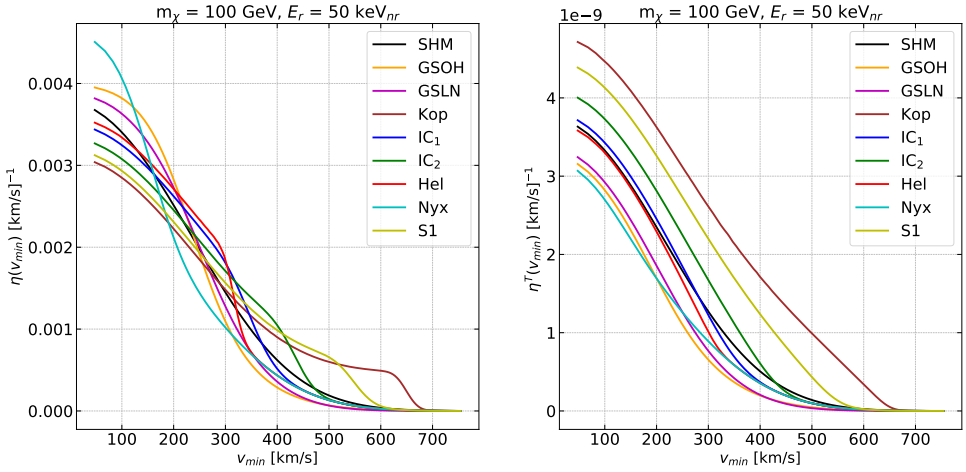

FIGURE 6.2: (Left) Integral (η) of the velocity distributions as a function of v_{min}. (Right) Integral (η^T) of the velocity distributions as a function of v_{min}. The VDFs were assumed at their maximum values of η_{sub} (see Table 5.1).

6.2 Recoil energy spectra for different interactions and VDFs

This section reports on the expected NR energy spectra. They depend on the underlying VDF as well as the DM and nuclear response functions. The differential rate was estimated via a boolean option inside the `eval_maxpatch.cc` file of Maxpatch. The spectra were normalized to the cross-section values defined by each operator at $m_\chi = 100\ \mathrm{GeV}/c^2$: $\mathcal{O}_1$ (3.7×10^{-45} cm^2), $\mathcal{O}_3$ (3.1×10^{-38} cm^2), $\mathcal{O}_5$ (2.9×10^{-36} cm^2), $\mathcal{O}_8$ (1.9×10^{-38} cm^2), and $\mathcal{O}_{11}$ (2.3×10^{-42} cm^2).

Fig. 6.3(a) shows the recoil energy spectra of the studied effective operators, assuming the SHM. Operators that introduce a factor of q^2 to the DM response function ($\mathcal{O}_5, \mathcal{O}_{11}$) are suppressed at low recoil energies, exhibiting a peak around 25 keV while $\mathcal{O}_3$ ($\sim q^4$) has a peak around 50 keV. On the other hand, the operators that add a factor of $v_\perp^2$ ($\mathcal{O}_5$ and $\mathcal{O}_8$) have qualitatively little effect on the recoil spectra, though the spectra drop off slightly faster because $v_\perp$ suppresses backscattering.

In Fig. 6.3(b), the effects of substructures on the $\mathcal{O}_1$ recoil spectrum are illustrated, where each substructure has been taken at its maximum η_{sub}. Spectra from slow substructures (GS, G4, G5, and G6) decrease faster than predicted by the SHM, while those resulting from fast substructures (G1, G2, and G3) are flattened by a knee around 75–175 keV. While these distortions affect the expected rate of recoils in the energy region of interest, the spectra in this range are similar.

The effect that substructures may have for $\mathcal{O}_1$, $\mathcal{O}_8$, and $\mathcal{O}_{11}$ is shown in Fig. 6.4(a). These operators were selected, for their respective scaling factors of 1, $v_\perp^2$ and q^2. The effects of GS (O'Hare) and G1 streams are compared to the spectra derived from the pure SHM, assuming the maximum considered value of η_{sub}. These substructures were chosen to span the range of low- and high-speed VDFs.

The spectra from $\mathcal{O}_8$ and $\mathcal{O}_{11}$ are more strongly affected by these substructures than $\mathcal{O}_1$. For $\mathcal{O}_{11}$, the GS causes the recoil spectrum to decrease nearly exponentially, at a faster rate than the SHM alone predicts, while G1 renders it near flat in the range of 25–175 keV. This shape is a result of the higher momentum transfers accessible by the fast components of G1; the cross-section for such interactions is increased by the q^2-enhancement of this operator. However, the energy region of interest used in this study extends to 100 keV, below much of this enhancement.

Stronger effects are observed for O8, for which the nuclear scattering cross-section scales with $v_\perp^2$. In this case, fast DM particles in G1 have an enhanced nuclear scattering cross-section, even when the momentum transfer is relatively small. This behavior leads to enhanced cross-sections across all accessible energy scales. Similarly, substructures like the GS that decrease the amount of fast DM suppress the recoil spectrum.

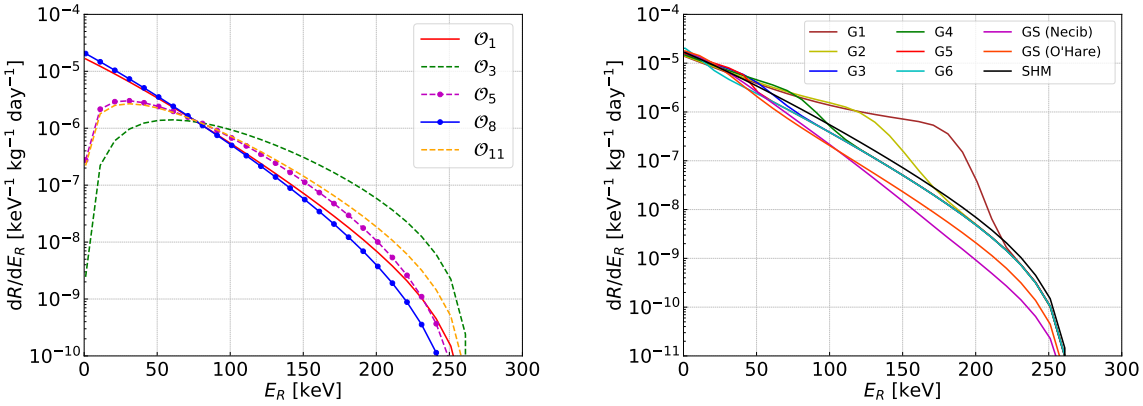

(a) (b)

FIGURE 6.3: a) Recoil spectra of the effective operators with SHM. b) Recoil spectra for $\mathcal{O}_1$ and different substructures at maximum η_{sub}.

Fig. 6.4(b) shows the recoil energy spectra for DM-nucleon couplings via the same three operators, assuming the SHM, for isoscalar (IS), isovector (IV), and Xenonphobic (XP) isospin scenarios (described in Section 6.4). Similar behavior is observed for all three operators. IS interactions have the strongest nuclear couplings, due to the coherent A^2 enhancement (where A is the atomic mass number), while interferences between protons and neutrons suppress IV and XP interactions. These interactions all have slightly different shapes, governed by their corresponding nuclear response function (Eq.4.12). These functions are defined for IS and IV components, as well as their cross terms, which appear in XP interactions. The IV term decreases the most quickly with recoil energy, while the cross-terms are relatively flat. As a result, the IV energy spectrum decreases the fastest, while the XP spectrum (the only one including the cross-terms) decreases the slowest.

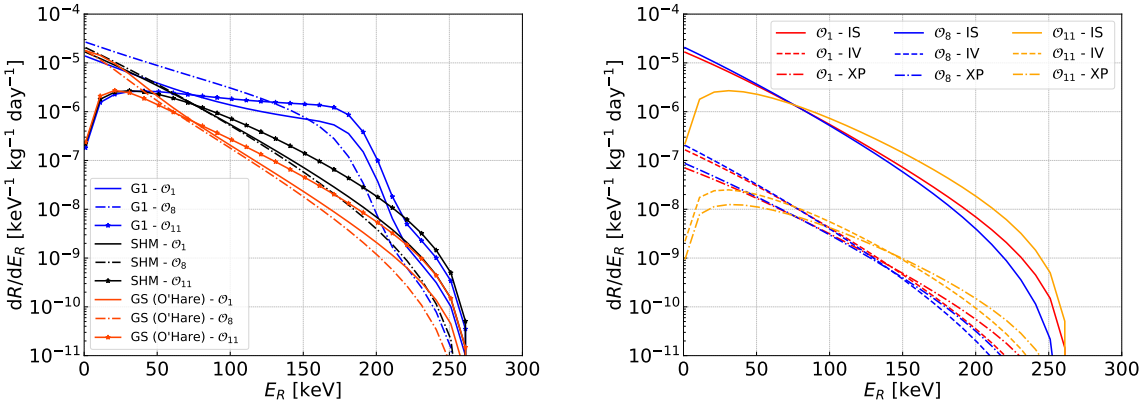

(a) (b)

FIGURE 6.4: a) Recoil spectra for m_χ=100 GeV/c^2 and with VDFs from G1 (blue), SHM (black), and GS(O'Hare) (orange). b) Recoil spectra for m_χ=100 GeV/c^2 and SHM with IS, IV, and XP couplings.

6.3 Constraints on effective operators with the SHM

Exclusion curves on the operators $\mathcal{O}_1$, $\mathcal{O}_3$, $\mathcal{O}_5$, $\mathcal{O}_8$ and $\mathcal{O}_{11}$ using the SHM are presented in Fig. 6.5. Besides the isoscalar interaction (IS), isospin-violating cases were also covered (IV, XP). The plot specifies the DM-proton cross-section σ_p as a function of the WIMP mass m_χ.

Operators $\mathcal{O}_1$, $\mathcal{O}_5$, $\mathcal{O}_8$ and $\mathcal{O}_{11}$ depend on the M response function, and $\mathcal{O}_3$ depends on Φ'' (responses defined in Section 4.3). The interactions governed by $\mathcal{O}_5$, $\mathcal{O}_8$ and $\mathcal{O}_{11}$ are suppressed relative to $\mathcal{O}_1$, despite using the same nuclear response function. This suppression is due to the additional factor of $(q/m_N)^2 \sim 10^{-3} - 10^{-2}$ in $\mathcal{O}_{11}$ and the factor of $v_\perp^2 \sim 10^{-6}$ in $\mathcal{O}_8$; while both factors suppress $\mathcal{O}_5$.

The operator $\mathcal{O}_3$ is proportional to $(q/m_N)^4$, and $\mathcal{O}_{11}$ goes as $(q/m_N)^2$. $\mathcal{O}_3$ is described by the Φ'' multipole operator, while $\mathcal{O}_{11}$ is described by M. Since the former operator is related to spin-orbit coupling, it couples to the two unpaired neutrons and proton holes in ^{40}Ar, rather than to all 40 nucleons. This leads to a suppression of $\sim 10^2$ in addition to the extra q^2 suppression.

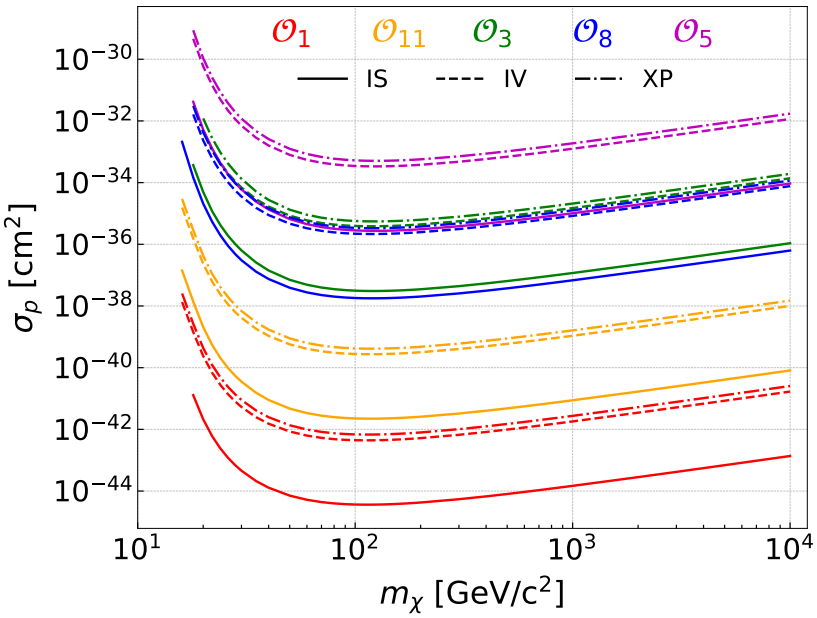

FIGURE 6.5: Upper limits (90% C.L.) on DM-nucleon cross-sections with the SHM and operators: $\mathcal{O}_1$ (red), $\mathcal{O}_{11}$ (orange), $\mathcal{O}_3$ (green), $\mathcal{O}_8$ (blue) and $\mathcal{O}_5$ (magenta). IS interactions (solid lines) set the strongest constraints. Isospin-violating cases (IV: dash lines, and XP: dash-dot lines) are also shown.

6.4 Effects of isospin violation

Isospin-violating DM has been previously studied [135] as a way of reconciling the positive signals from experiments like DAMA with the null result of others, e.g. XENON1T. The interactions of WIMPs relate to electroweak symmetry, particularly to hypercharge. Since right-handed up and down quarks have different hypercharge, it would be natural to expect these interactions to depend on isospin [135].

The case where the WIMP couples equally with neutrons and protons ($f_n = f_p$) is known as isospin-conserving or isoscalar (IS) interaction, which is assumed by default on direct detection experiments. This assumption has non-definitive theoretical and experimental motivations since it is just a particular case. More general is to consider scenarios of isospin-violation, $f_n \neq f_p$. If the relationship between couplings is $f_n = -f_p$, corresponds to the isovector case (IV). Commonly, the exclusion limits are given in terms of DM-nucleon cross-section, σ_N^Z:

$$\sigma_N^Z = \sigma_p \frac{\sum_i \eta_i \mu_{A_i}^2 \left[Z + (A_i - Z) f_n/f_p\right]^2}{\sum_i \eta_i \mu_{A_i}^2 A_i^2}, \tag{6.1}$$

where the sum is over isotopes i of a target material, with η_i as the natural abundance of each isotope. σ_p denotes the DM-proton cross-section, μ_{A_i} is the DM-nucleus reduced mass, and f_p and f_n correspond to the proton and neutron couplings, respectively. The SI DM-proton cross-section is $\sigma_p = 4\mu_p^2 f_p^2/\pi$. The particular case in which $\sigma_N^Z = \sigma_p$ is for $f_n = f_p$ (isospin-conservation), but it would be reasonable to expect a different relationship between couplings because nucleons' internal structure differs. Specially, scenarios where $f_n/f_p < 0$ can yield to $\sigma_N^Z \ll \sigma_p$. In general, it is σ_p, rather than σ_N^Z, that is physically meaningful and that should be used to present and compare different experimental results [136]. The loss of sensitivity in a DM experiment when the interaction violates isospin symmetry could be accounted for with the parameter $F_Z \equiv \sigma_p/\sigma_N^Z$.

For elements with only one naturally abundant isotope, there exists a choice of f_n/f_p such that $F_Z \to \infty$, resulting in zero sensitivity for scattering off those elements. In contrast, if an element has multiple isotopes, there is an upper bound on F_Z, since completely destructive interference cannot be simultaneously achieved for all isotopes at once, and there is a reduced but nonzero sensitivity in such elements [135]. This behavior can be seen in Fig. 6.6, where three target materials are used as examples: argon, xenon, and germanium. In the argon case, as it consists mostly of a single isotope, F_Z goes to arbitrarily high values at the Argonphobic point ($f_n/f_p = -0.82$), where there is an exact cancellation between the neutron and proton contributions to the cross-section and the DM does not interact with an argon nucleus. However, since natural Xe and Ge elements are composed of several isotopes, an exact cancellation is not possible and F_Z has a maximum value. In particular, is the value of $f_n/f_p \approx -0.7$ at the maximum for xenon, what defines the so-called Xenonphobic DM scenario (XP) [135–137].

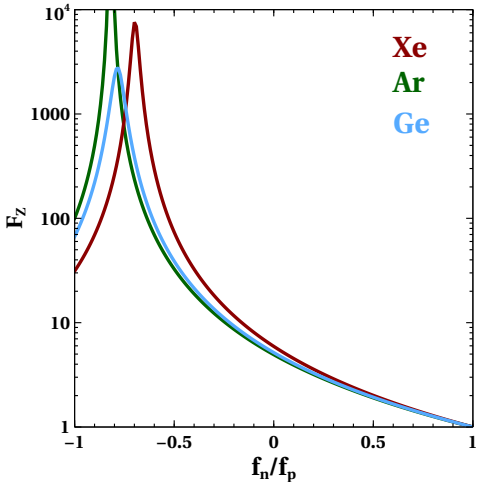

FIGURE 6.6: Suppression factor (F_Z) as a function of f_n/f_p for argon (green), xenon (red) and germanium (cian) targets. Image from [137].

Shortly after the DEAP collaboration reported the first-year WIMP search results, an article pointing out that ^{40}Ar experiments could be more sensitive than Xe to some isospin-violating DM scenarios was published [136]. The paper claimed the DEAP limit does set a world-leading result for a specific region of the parameter space. Fig. 6.7 shows how the DEAP constraint (dash blue) is better than that of XENON1T (dash red) for WIMP masses above ~ 120 GeV. The former result was achieved by re-scaling the cross-section values reported in [1]. In this thesis, the limit becomes even stronger after using NREFT with $\mathcal{O}_1$ (dash black). The reason lies in the form factor used. While the Helm form factor employed by [136] shows loss of coherence with the increase of q^2; within NREFT the M nuclear response (its equivalent) changes assuming $f_n \neq f_p$ and ends up dropping off less fast. IV limits were also determined and included in the plot.

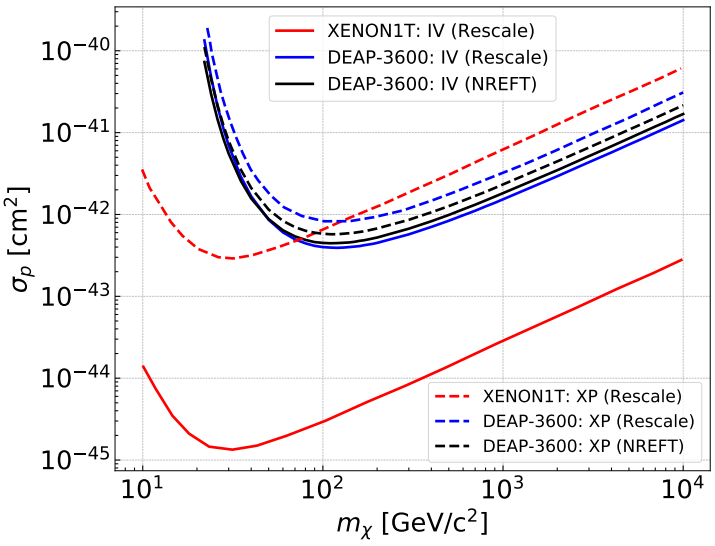

FIGURE 6.7: Constraints on the $\mathcal{O}_1$ interaction in presence of isospin-violating scenarios for XENON1T and DEAP experiments. A neutron-to-proton coupling ratio of $f_1^n/f_1^p = -0.7$ for XP and $f_1^n/f_1^p = -1$ for IV were employed. Limits labeled rescale follow the approach from [136].

6.5 Effects of non-thermal components on the constraints

The effects of various DM halo substructures on cross-section upper limits for the IS $\mathcal{O}_1$ interaction appears in Fig. 6.8(a), using the maximum values of η_{sub}. The strongest effects are seen at lower m_χ, where the experiment probe larger v_{min} values, and is therefore sensitive to the high-velocity tail of the VDFs. Therefore, slow substructures weaken the limits at low m_χ, while fast ones strengthen them. These effects diminish at higher m_χ, where a higher fraction of the DM will have enough kinetic energy to produce visible signals until they level off at some constant deviation from the limits derived with the SHM.

Once slow particles have enough kinetic energy to reliably produce detectable signals, the effects of increasing their velocity become smaller. As a result, streams modeled by G1, G2, and G3 lead to stronger limits, while both GS models and the streams G4, G5, and G6 result in weaker limits. Fig. 6.8(b) illustrates how these limits change when $\mathcal{O}_5$ is considered, instead. Each substructure is again taken at its maximum η_{sub}. A similar trend is observed, in which faster substructures lead to stronger limits and slower substructures lead to weaker limits. However, the effects are much more significant, due to the dependence of $\mathcal{O}_5$ on $v_\perp^2$ with more than an order of magnitude variation seen near $m_\chi \approx 100$ GeV/c^2. These differences persist at higher masses.

For operators that depend on $v_\perp$, enhancing the high-velocity component of the VDF increases the fraction of candidates with enough kinetic energy to produce a detectable signal, as for $\mathcal{O}_1$. These high-velocity DM particles also have enhanced nuclear scattering cross-section, yielding stronger constraints. Likewise, slower substructures have DM with suppressed interactions and weaker limits.

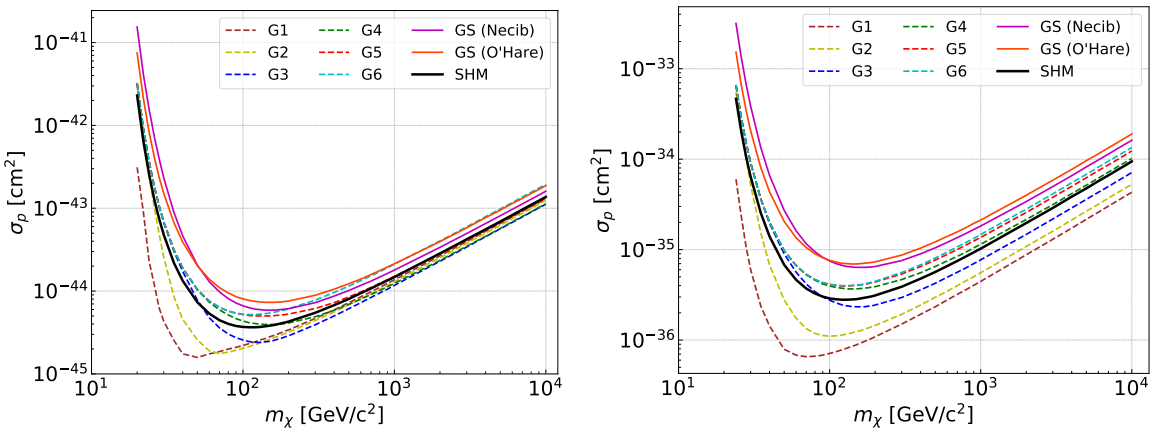

FIGURE 6.8: a) Exclusion limits (90% C.L.) on effective operators $\mathcal{O}_1$ (a) and $\mathcal{O}_5$ (b) for substructures in this study.

6.6 Isoscalar limits in the presence of halo substructures

Exclusion curves for each operator under consideration and substructure VDF were obtained (Fig. 6.9, Fig. 6.10). The figures include the effect of varying η_{sub}, visualized as a gradient. This was achieved by linearly interpolating curves between the extremes and assigning a color from *Matplotlib* colormaps. A subplot with the relative difference between the substructure's limit at its maximum value of η_{sub} and the minimum value (SHM limit) was inserted.

As noted earlier, DM particles with $m_\chi < 100$ GeV/c^2 exhibit the most sensitivity to substructures, since potential signals in the energy region of interest come from high-velocity tails of the VDFs, where the DM speed can compensate for the lower mass. For $\mathcal{O}_1$, $\mathcal{O}_3$, and $\mathcal{O}_{11}$, exclusion curves drawn for higher-mass DM become relatively insensitive to most of the substructures considered here, typically deviating from the SHM result by 10% or less. For $\mathcal{O}_5$ and $\mathcal{O}_8$, for which $R_k \propto v_\perp^2$, these differences persist at higher m_χ, as the velocity enhancement of the cross-section is independent of m_χ. As a result, these operators are more sensitive to changes in the VDF than the others.

Both models of the GS result in weaker constraints, due to their relatively low velocity in the laboratory frame. However, the parametrization by O'Hare (Fig. 6.9(b)) affects the constraints more strongly at higher m_χ compared to the model by Necib (Fig. 6.9(a)). Their relative effects reverse at lower masses where Necib's model has a greater impact. This behavior is because the model described by O'Hare is both slower and narrower than the model by Necib.

The fastest streams, represented by G1 and G2 groups (Fig. 6.9(c), Fig. 6.9(d)), strengthen the limits with a significant effect between 20 and 200 GeV/c^2 WIMP masses. The $v_\perp$-dependent $\mathcal{O}_5$ and $\mathcal{O}_8$ interactions are particularly affected at higher masses compared to the rest of the operators. A similar phenomenon was indicated in [22]. This can be explained through Eq. 4.25, where η^T appears as a function of v_{min}^2 and it tends to be nearly constant by increasing the DM mass (Fig. 2.6), so the second term in such expression decreases while the first one dominates resulting in a larger value of η^T and thus a greater event rate. The relative deviation subplot clearly indicates the split among curves.

Limits from streams G3 and G4 are shown in Fig. 6.10(b) and Fig. 6.10(a), respectively. Both streams decrease sensitivity by up to 40% at 40 GeV/c^2, with varying behavior at higher masses. For $\mathcal{O}_5$ and $\mathcal{O}_8$ at higher masses, G4 decreases the sensitivity by up to 9%, while it increases the sensitivity by up to 20% for the other operators. At these masses, G3 streams increase the sensitivity for all operators, though limits for $\mathcal{O}_5$ and $\mathcal{O}_8$ are strengthened by 24%, while the others are improved by up to 20%. These streams increase the sensitivity in some mass ranges and decrease it at other masses due to their narrow VDFs; while the VDFs have a slightly higher means than the SHM, their lower spread decreases the population of the high-velocity tail.

Streams described by G5 (Fig. 6.10(c)) consistently yield limits within 40% of those obtained from the pure SHM at 40 GeV/c^2, and agree with the SHM prediction to within 3% at 3 TeV/c^2. These streams have a mean close to that of the SHM, and their impact on DM sensitivity mostly derives from the effect of narrowing the VDF. The slowest stream, G6 (Fig. 6.10(d)), decreases sensitivity uniformly across all masses. DM particles in these substructures have too little kinetic energy across at all considered masses, and so cannot produce a signal in the energy region of interest. Instead, all candidate signals would come from the residual SHM-like component.

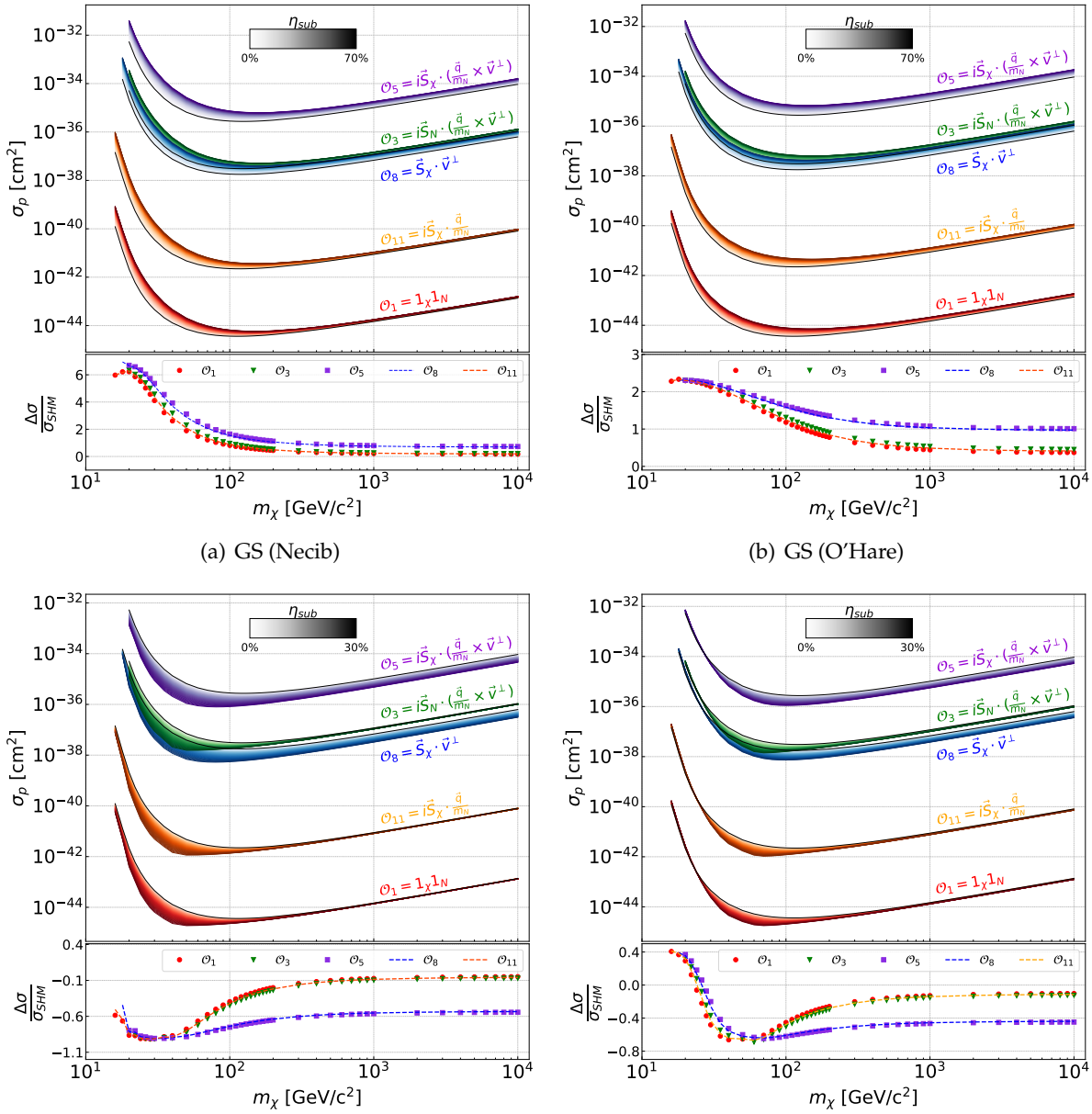

(a) GS (Necib)

(b) GS (O'Hare)

(c) G1 streams

(d) G2 streams

FIGURE 6.9: Upper limits (90% C.L.) on WIMP-nucleon scattering cross-sections for the $\mathcal{O}_1$, $\mathcal{O}_3$, $\mathcal{O}_5$, $\mathcal{O}_8$, and $\mathcal{O}_{11}$ effective operators, in the presence of VDFs corresponding to both Gaia Sausage models, G1 streams, and G2 streams with η_χ of the DM contained in the specified substructure. Beneath each set of exclusion curves is the relative deviation of each operator with the given substructure at its maximum value compared to the SHM and where $\Delta\sigma = \sigma_{\text{Sub}} - \sigma_{\text{SHM}}$.

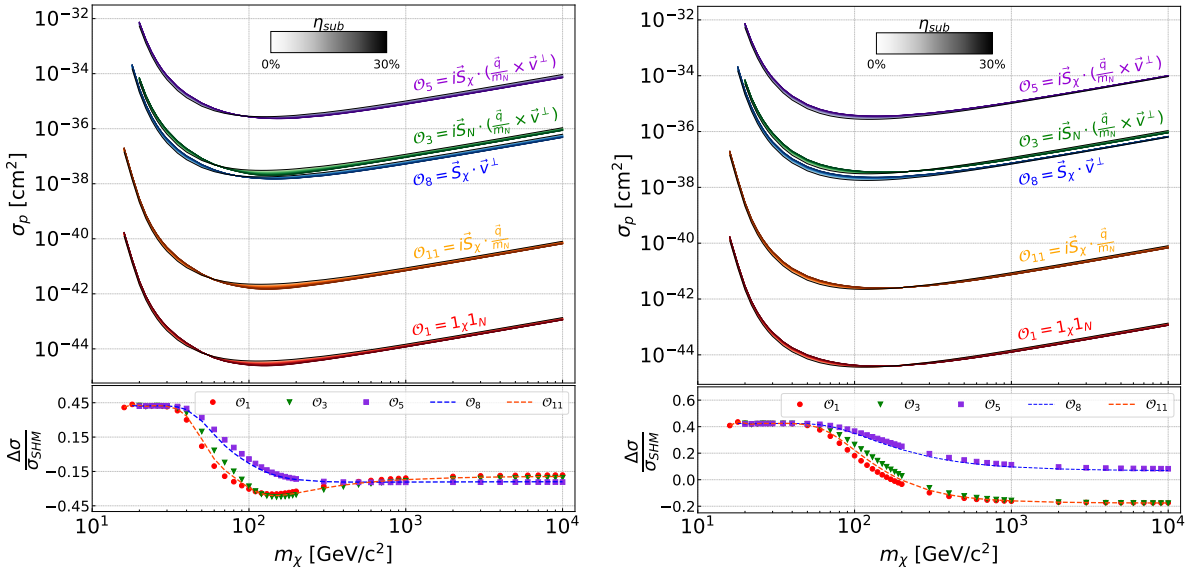

(a) G3 streams

(b) G4 streams

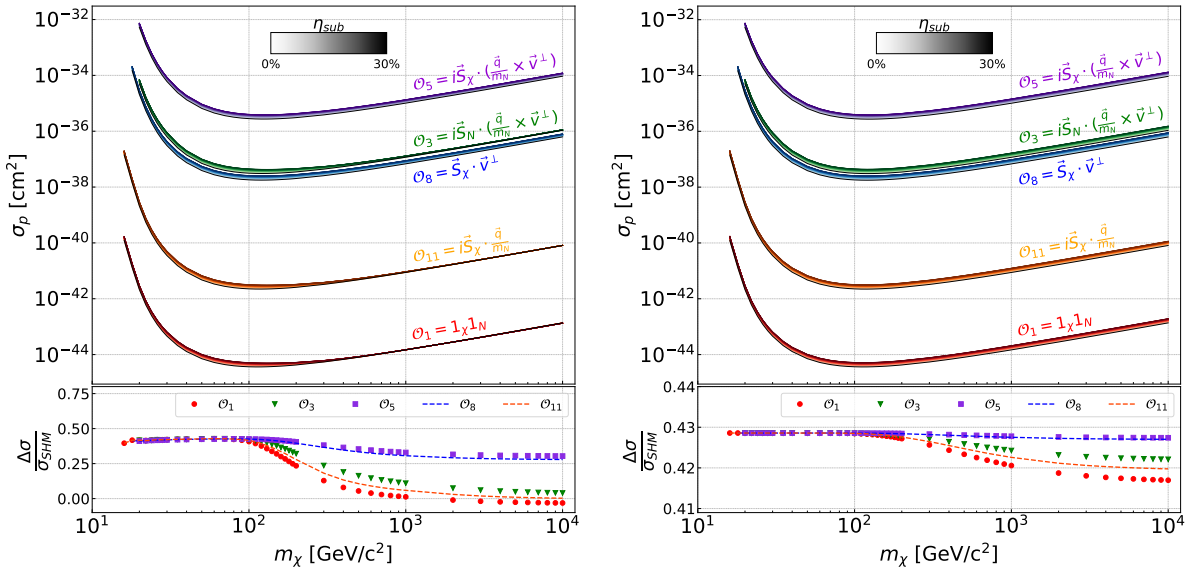

(c) G5 streams

(d) G6 streams

FIGURE 6.10: Upper limits (90% C.L.) on WIMP-nucleon scattering cross-sections for the $\mathcal{O}_1$, $\mathcal{O}_3$, $\mathcal{O}_5$, $\mathcal{O}_8$, and $\mathcal{O}_{11}$ effective operators, in the presence of VDFs corresponding to the G3, G4, G5 and G6 streams, with η_χ of the DM contained in the specified substructure. Beneath each set of exclusion curves is the relative deviation of each operator with the given substructure at its maximum value compared to the SHM and where $\Delta\sigma = \sigma_{\text{Sub}} - \sigma_{\text{SHM}}$.

6.7 Simultaneous effects of all model variations

As a way to visualize the effect of all model variations (operators, substructures, isospin cases and η_{sub} values), summary plots at three specific masses (40 GeV/c^2, 100 GeV/c^2 and 3 TeV/c^2) were created, containing information of 360 constraints (Fig. 6.11(a), 6.11(b), 6.11(c)). Limits

were calculated using ComputeCanada computational resources and later processed with a Python code. Each figure was conformed with 8 independent subplots, where one color was associated to each operator, and the gradient in rectangles represents the change of η_{sub}. If the color of the gradient becomes darker towards the left (right) it means a stronger (weaker) limit on σ_p. Wider shadings reflect the substructures with more impact on DEAP limits. For all operators, constraints on lower-mass DM candidates are most strongly affected by substructures. Upper limits derived from $\mathcal{O}_1$, $\mathcal{O}_3$, and $\mathcal{O}_{11}$ become relatively insensitive to substructures at higher masses, while $\mathcal{O}_5$ and $\mathcal{O}_8$ remain sensitive.

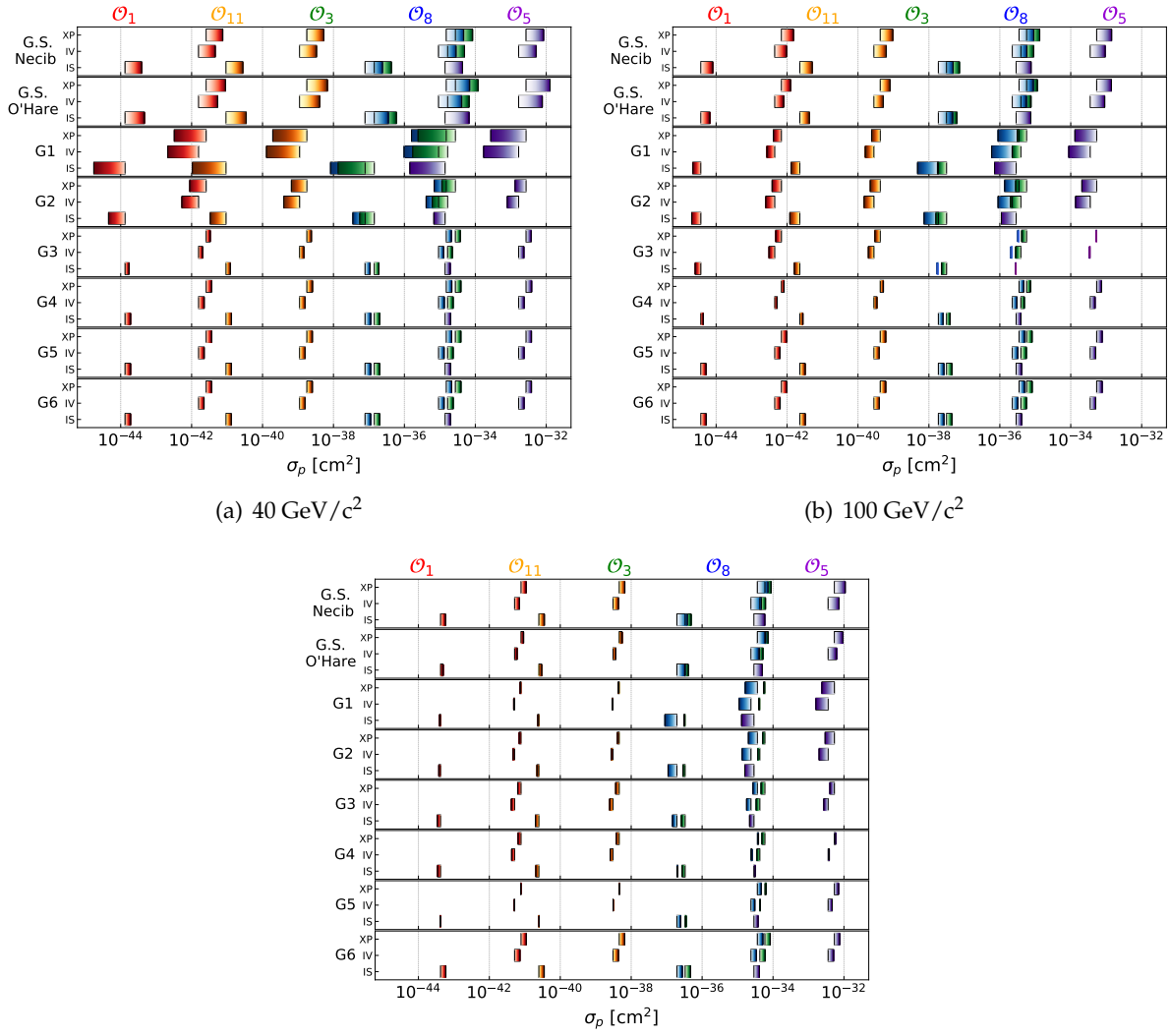

(a) 40 GeV/c^2

(b) 100 GeV/c^2

(c) 3 TeV/c^2

FIGURE 6.11: Summary plots showing cross-section values at 40 GeV/c^2, 100 GeV/c^2 and 3 TeV/c^2 WIMP masses for chosen VDFs and isospin cases (IS, IV, XP). Operators' color (from left to right on the σ_p axis) are: $\mathcal{O}_1$ (red), $\mathcal{O}_{11}$ (orange), $\mathcal{O}_3$ (green), $\mathcal{O}_8$ (blue) and $\mathcal{O}_5$(magenta). GS_1 refers to the Gaia Sausage VDF from *O'Hare* and GS_2 to *Necib*'s. A shading band indicates where the maximum (darker side) and minimum (clearer side) of DM fraction lie for a given operator. The minimum always coincides with $\eta_{\text{sub}} = 0\%$, the cross-section value at the SHM.

6.8 Limits on photon-mediated interactions

Fig. 6.12 includes upper bounds on photon-mediated interactions derived by using NREFT with the SHM VDF. For $m_\chi = 100$ GeV/c^2, this analysis excludes an anapole coupling $c_A > 4.76 \times 10^{-5}$ GeV^{-2} ($\sigma_A > 2.39 \times 10^{-37}$ cm^2) at 100 GeV/c^2, a magnetic dipole $\mu_\chi > 1.08 \times 10^{-8}\ \mu_B$ GeV^{-1} ($\sigma_\mu > 1.24 \times 10^{-44}$ cm^2), an electric dipole moment $d_\chi > 1.46 \times 10^{-9}$, and an electric charge $\epsilon_\chi > 7.43 \times 10^{-10}\ e$.

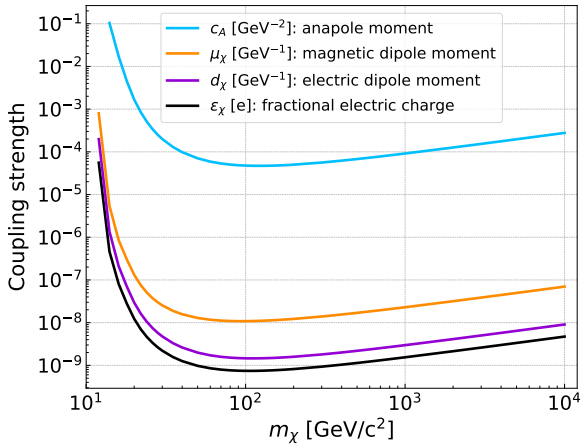

FIGURE 6.12: Limits on the coupling strength of specific interactions using the SHM.

Previous limits were compared with those reported by Buch *et.al.*[22] for XENON1T. As can be seen in Fig. 6.13, the constraints from XENON1T are stronger.

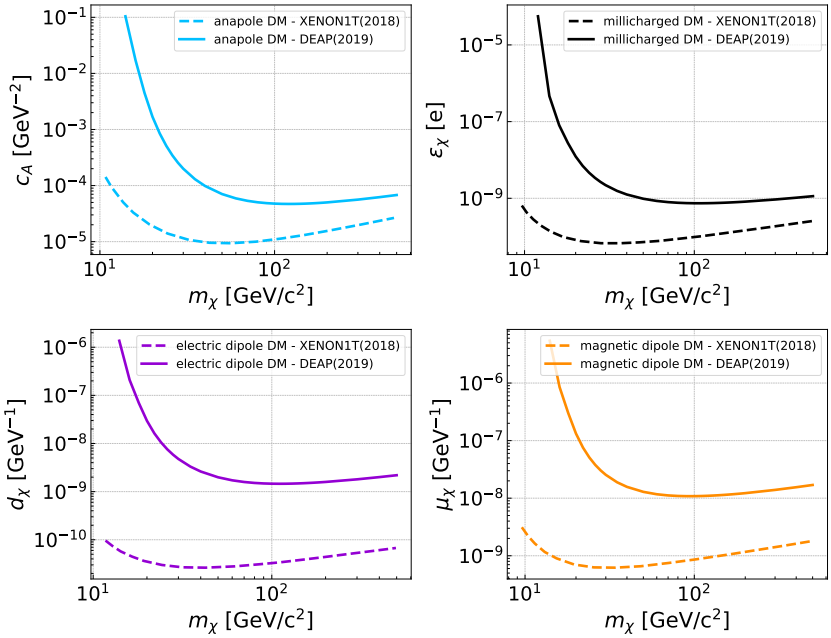

FIGURE 6.13: Comparison of specific interactions for Ar and Xe targets, in the DEAP-3600 and XENON1T experiments, respectively.

However, the anapole case seems to be less than a factor of 3 less sensitive than XENON1T, which means the ongoing analysis of the DEAP collaboration including machine learning methods and enlarged statistics could produce a world-leading result for anapole DM at high WIMP masses. These interactions computed for all substructures are shown in Fig. 6.14(a), 6.14(b), 6.15(a) and 6.15(b).

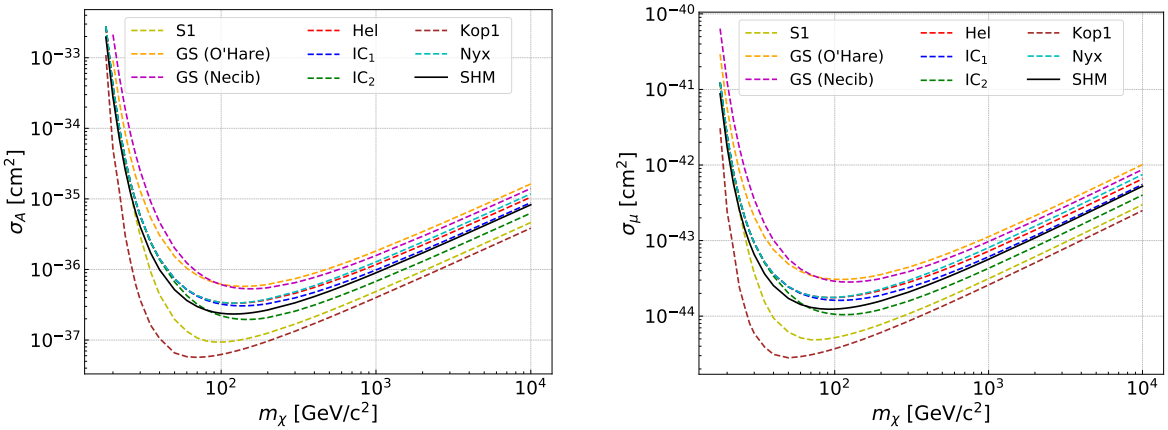

(a) (b)

FIGURE 6.14: Constraints on anapole (a) and magnetic dipole (b) interactions for selected VDFs.

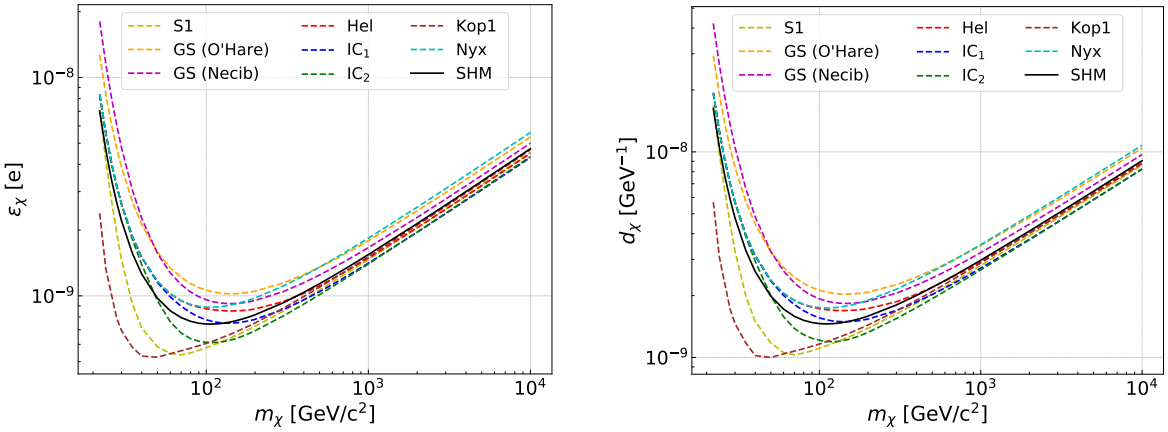

(a) (b)

FIGURE 6.15: Constraints on millicharge (a) and electric dipole (b) interactions for selected VDFs.

6.9 DEAP-3600 plans and projections

Currently, DEAP-3600 is under a hardware upgrade mainly addressed to reduce neck alpha and dust backgrounds; components like coated flow-guides and an alternate cooling system are close to being installed. These upgrades would allow the detector to recover the design sensitivity. Also, multivariate analyses to improve signal acceptance, a study for ^{8}B solar neutrinos

detection, and the analysis of 3 years of data are ongoing. Recently, constraints on Multiply-Interacting Massive Particles (MIMP) have been published [138]. In this thesis, projections for 1 year livetime exposure after hardware upgrades considering specific interactions (Fig. 6.16) and the xenonphobic scenario (Fig. 6.17) were calculated. Plots presented show leading results compared to XENON1T for certain regions of the parameter space.

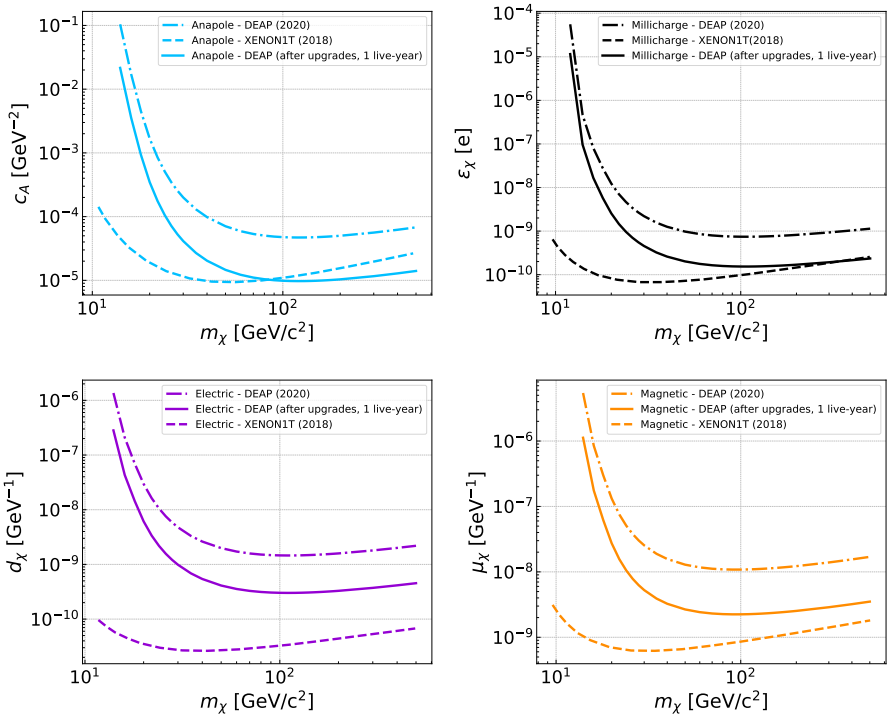

FIGURE 6.16: Limits on specific interactions after hardware upgrades with 1 year exposure. Constraints for XENON1T taken from [22].

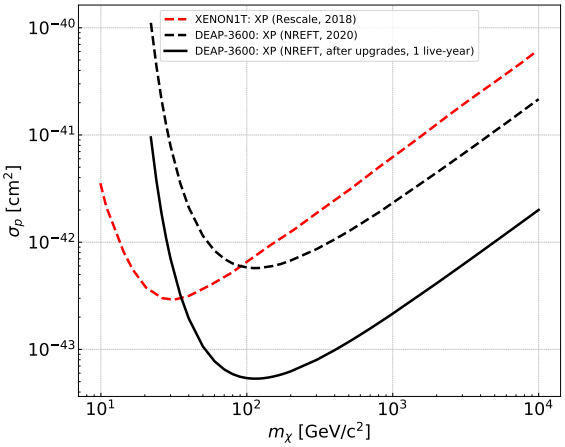

FIGURE 6.17: Projection for DEAP in the NREFT-XP scenario after hardware upgrades with 1 year exposure.

6.10 Propagation of uncertainties

The experimental parameters used for calculating the exclusion curves in DEAP have uncertainties (Table 6.2), hence it is required to propagate such errors onto the limits. The uncertainties concerning the PSD were neglected.

TABLE 6.2: Parameters employed for propagating the systematic uncertainties onto the exclusion curves: Exposure [kg·days], Light Yield (LY), Resolution, F_{prompt} (fp), Quenching, and Acceptance.

Parameter	Value	Type	Parameter	Name	Type
Exposure	780637.5	$+1\sigma$	fp_model	fpmean_upper_pf	$+1\sigma$
	758433.0	Nom		fpmean_pf	Nom
	736227.9	-1σ		fpmean_lower_pf	-1σ
LY_offset	1.5	$+1\sigma$	quench_model	global_qf_max.root	$+1\sigma$
	1.1	Nom		global_qf_mean.root	Nom
	0.7	-1σ		global_qf_min.root	-1σ
LY_linear	6.5	$+1\sigma$	accept	erfidacceptance_up	$+1\sigma$
	6.1	Nom		erfidacceptance_nom	Nom
	5.7	-1σ		erfidacceptance_dn	-1σ
Res_linear	1.55	$+1\sigma$	————	————	————
	1.42	Nom			
	1.29	-1σ			
Res_quadratic	0.0014	$+1\sigma$	————	————	————
	0.0004	Nom			
	0.0000	-1σ			

About 2160 exclusion curves were computed in order to assess the impact of the experimental uncertainties on the reported limits. In general, the effect was negligible as can be noted in Fig. 6.18, 6.19, 6.20 for some operators ($\mathcal{O}_1$, $\mathcal{O}_8$, $\mathcal{O}_{11}$) and VDFs (SHM, Helmi, GSLN).

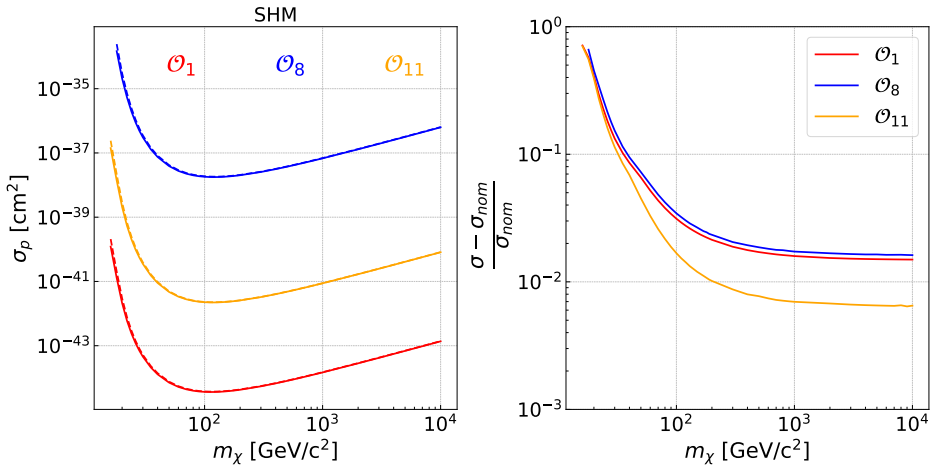

FIGURE 6.18: (Left) Upper limits before (solid lines) and after (dash lines) propagating the uncertainties on experimental input parameters for SHM VDF, three effective operators, and isoscalar spin case. (Right) Residual plot.

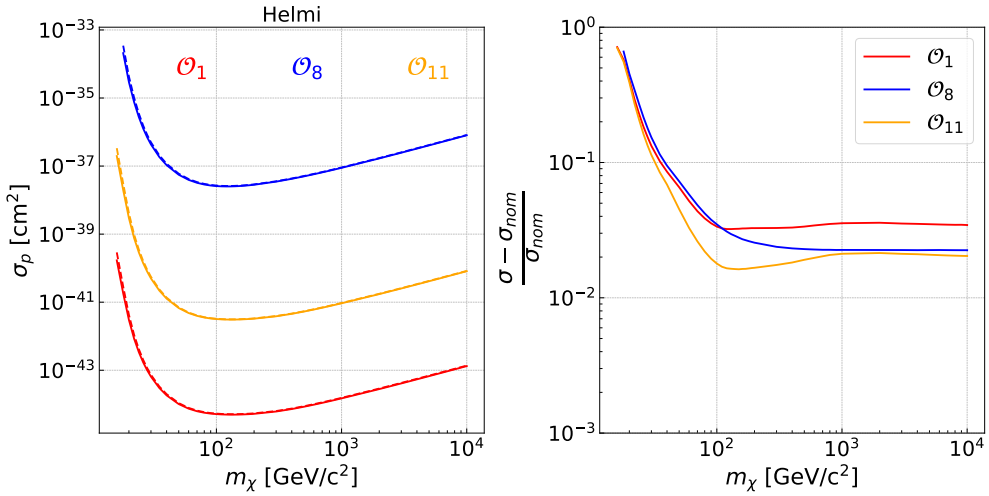

FIGURE 6.19: (Left) Upper limits before (solid lines) and after (dash lines) propagating the uncertainties on experimental input parameters for Helmi VDF, three effective operators, and isoscalar spin case (Right) Residual plot.

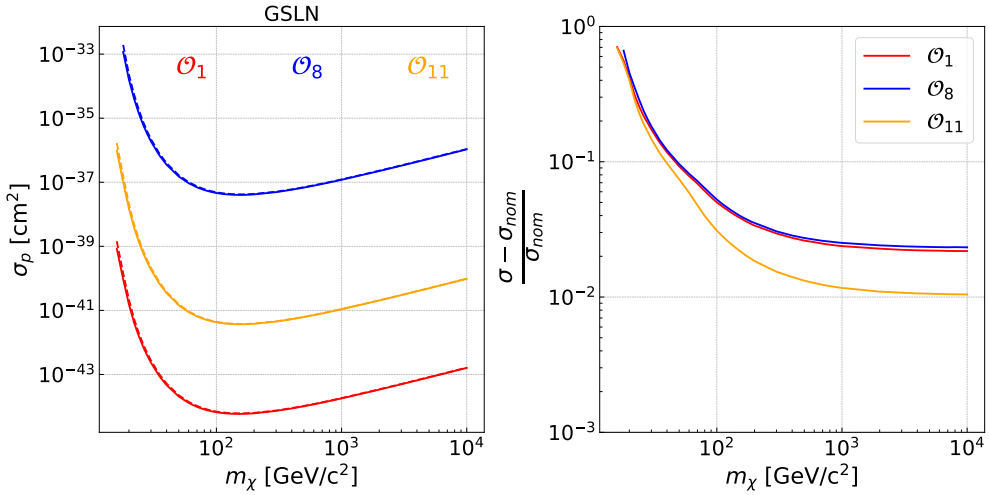

FIGURE 6.20: (Left) Upper limits before (solid lines) and after (dash lines) propagating the uncertainties on experimental input parameters for GS (L. Necib) VDF, three effective operators, and isoscalar spin case. (Right) Residual plot.

Chapter 7

Conclusions

This study (published in [3]) provides a better understanding of how particle/nuclear physics and astrophysical uncertainties could affect DEAP-3600 results. In case of future detection, it could help to disentangle the nature of dark matter. The main conclusions and final remarks are:

- Applying a Non-Relativistic Effective Field Theory to the DEAP-3600 results, new interaction terms describing the WIMP-nucleus elastic scattering for an argon target were considered.
- Reported upper limits (90% C.L.) on the effective operators: $\mathcal{O}_1$, $\mathcal{O}_3$, $\mathcal{O}_5$, $\mathcal{O}_8$, and $\mathcal{O}_{11}$, which comprise the nuclear responses M and Φ''.
- The $\mathcal{O}_1$ operator, classical SI interaction, sets the strongest limit followed by q^2-dependent operator $\mathcal{O}_{11}$.
- Operators $\mathcal{O}_5$ and $\mathcal{O}_8$, which scale with $v_\perp^2$, set the weakest constraints but are particularly sensitive to the VDF considered having a major impact at higher WIMP masses.
- Scenarios of isospin-violation (isovector, xenonphobic) were explored, with weaker limits in comparison to the typical isospin-invariant (isoscalar) case, $f_n = f_p$.
- Regarding the astrophysical model, six VDFs derived from stellar data and two generic in-falling clumps VDF were studied. They were modeled with a certain relative DM density (η_{sub}). There are significant changes in limits after varying η_{sub} for some substructures (e.g. G1, G2, and Gaia Sausage models).
- The principal modification in constraints was observed for $m_\chi < 300$ GeV/c^2, caused by the fastest substructures and the Gaia Sausages.
- Interestingly, the limits for in-falling clumps switch over the mass range, so for some WIMP masses the curves increase sensitivity and for others, it decreases.
- Two realizations of the Gaia Sausage VDF were considered, O'Hare's and Necib's. The latter suppressed more the sensitivity at low masses as η_{sub} increases.
- NREFT enabled to consider specific types of DM interactions: anapole, electric/magnetic dipole, and millicharged DM, which arise within this theory by combining the effective operators. Stringent exclusion limits were set for the coupling strength of these specific interactions after analyzing 231 live-days of data.

- It was demonstrated in [136] under a Xenonphobic DM scenario, that there is a region of parameter space where DEAP could set a stronger limit than XENON1T. This analysis reproduced such a scenario within the NREFT formalism and the limit becomes even stronger than previously reported.

- Different recoil energy spectra plots were included combining NREFT along with substructures VFD and isospin cases. The q-dependent operators ($\mathcal{O}_3, \mathcal{O}_5, \mathcal{O}_{11}$) suppress the rate for low-energy recoils, while VDFs with high-speed DM particles tend to produce a nearly constant event rate (e.g. G1) what might imply extending the ROI to higher energies. Isospin-violation cases suppress the rate compared to IS, and among themselves, IV dominates at low recoil energies and XP at energies greater than $\sim$ 150 keV.

- For the first time a measure of the gamma-ray flux between 10 and 70 MeV at SNOLAB has been reported from the analysis of four years of data with a NaI crystal (0.13 ± 0.01 $\mathrm{cm}^{-2}\ \mathrm{yr}^{-1}$).

Appendix A

Codes employed in the thesis

A.1 Code for modeling a velocity distribution: S1 example

```
%matplotlib inline
import numpy as np
import matplotlib.pyplot as pl
import scipy.stats
import uproot
import matplotlib as mpl

#------------------------------------------------------------------------
#Input parameters
vesc = 544
v0   = 220
sigmav = v0/np.sqrt(2.)

U = 11.1
V = 12.24
W = 7.25

vorb_x = 29.4
vorb_y = -0.11
vorb_z = 5.90

npart = 20000000
mean  = [0,0,0]

#------------------------------------------------------------------------
#Round halo simulation_SHM

cov = [[sigmav**2,0,0],[0,sigmav**2,0],[0,0,sigmav**2]]
vx,vy,vz = np.random.multivariate_normal(mean, cov, npart).T

v = np.sqrt(vx**2 + vy**2 + vz**2)

vx_red = vx[v <= vesc]
vy_red = vy[v <= vesc]
vz_red = vz[v <= vesc]
```

```
v_red  = np.sqrt(vx_red**2 + vy_red**2 + vz_red**2)

vx_lab = vx_red + 0  + U + vorb_x
vy_lab = vy_red + 0  + V + vorb_y
vz_lab = vz_red + v0 + W + vorb_z

vR_lab = np.sqrt(vx_lab**2 + vy_lab**2 + vz_lab**2)
#------------------------------------------------------------------------
#S1 stream simulation

sigma_r  = 82.6
sigma_t  = 58.5
sigma_p  = 26.9

cov1     = [[sigma_r**2,0,0],[0,sigma_t**2,0],[0,0,sigma_p**2]]
vx1,vy1,vz1 = np.random.multivariate_normal(mean, cov1, npart).T

v1 = np.sqrt(vx1**2 + vy1**2 + vz1**2)

vx1_red = vx1[v1 <= vesc]
vy1_red = vy1[v1 <= vesc]
vz1_red = vz1[v1 <= vesc]

vstr_r = -29.6
vstr_t = -72.8
vstr_p = -297.4

vx1_lab = vx1_red + 0  + U + vorb_x - vstr_r
vy1_lab = vy1_red + 0  + V + vorb_y - vstr_t
vz1_lab = vz1_red + v0 + W + vorb_z - vstr_p

vS1_lab = np.sqrt(vx1_lab**2 + vy1_lab**2 + vz1_lab**2)

#------------------------------------------------------------------------
#Plotting the PDF
pl.figure(figsize=(10,8))

nbins = 100
npts  = 100
x  = np.linspace(0.0, 800.0, npts)

h1  = np.histogram(vR_lab, nbins, range=(0,800))
hist_vR = scipy.stats.rv_histogram(h1)
fv_R = hist_vR.pdf(x)
#pl.plot(x, fv_R, 'k--', label='100% SHM')

h2 = np.histogram(vS1_lab, nbins, range=(0,800))
```

```
hist_vS1 = scipy.stats.rv_histogram(h2)
fv_S1 = hist_vS1.pdf(x)
#pl.plot(x,fv_S1 , 'r.', label='PDF s1')



eta = 0.0
fv_S1_total = (1 - eta)*fv_R + eta*fv_S1
#pl.plot(x, fv_S1_total , 'b.', label='100% SHM + 0% S1')

eta2 = 0.3
fv_S1_total2 = (1 - eta2)*fv_R + eta2*fv_S1
pl.plot(x, fv_S1_total2 , 'y--', label='70% Halo + 30% S1')

pl.grid(True, color='silver', linestyle='--', linewidth=0.5)
pl.xlabel(v [km/s])
pl.ylabel(f(v) [km/s]$^{-1}$)
pl.legend(loc=0, prop={'size': 15})
pl.show()
```

A.2 Code of specific interactions

Recoil rate implementation for anapole Dark Matter.

```
double RecoilRate_Isotropic::get_recoilrate_at(double Er_keV){

 //Units in GeV^-2

 double _vE = get_velocity_profile()->get_vE();
 double sigmav= 156.0;

 double cn[11];
 double cp[11];

 for(int k=0;k<=10;k++){ cn[k] = 0; cp[k] = 0; }

 double alpha = 0.007297;
 double e = sqrt(4*TMath::Pi()*alpha);

 //Operator 8
 cp[7] = -2.0*e*sqrt(_sigma0_cm2*TMath::Pi())/mu;

 double rate = dRdE_NREFT(Er_keV,_Mwimp_GeV, cp, cn,_A,_vE, sigmav,_v_esc);
 return rate;
}
```

The function `dRdE_NREFT()` was defined as:

```
double RecoilRate_Isotropic::dRdE_NREFT(double E, double m_x, double cp[11],
            double cn[11], int A, double vlag, double sigmav, double vesc){

    double pi=TMath::Pi();
    double eta  = calcEta_num(vmin(E, A, m_x), vlag, vesc);
    double meta = calcMEta_num(vmin(E, A, m_x),vlag, vesc);

    double amu = 931.5e3;                  // keV
    double q1 = sqrt(2*A*amu*E);

    //Recoil momentum over nucleon mass
    double qr = q1/amu;

    // Required for form factors
    double q2 = q1*(1e-12/1.97e-7);
    double b  = sqrt(41.467/(45*pow(A,-1.0/3.0) - 25*pow(A,-2.0/3.0)));
    double y  = pow((q2*b)/2, 2);

    //Dark matter spin factor
    double jx = 0.5;
    double jfac = jx*(jx+1.0);

    double rate  = E*0.0;
    double Jval  = 0.0;
    double rho0  = 0.3;   //GeV/cm^3

    double R_M   = 0;
    double R_P2  = 0;
    double R_P2M = 0;

    double c_sum[11];
    double c_diff[11];
    double c[11][2];

    for (int i=0;i<=10;i++){
        c_sum[i]  = cp[i] + cn[i];
        c_diff[i] = cp[i] - cn[i];
        c[i][0] = c_sum[i];
        c[i][1] = c_diff[i];
    }

    for (int tau1=0; tau1<=1; tau1++){
        for(int tau2=0; tau2<=1; tau2++){

    R_M = c[0][tau1]*c[0][tau2]*eta +  jfac/3.0*(pow(qr,2)*meta*c[4][tau1]*c[4][tau2] + \
        meta*c[7][tau1]*c[7][tau2] + pow(qr,2)*eta*c[10][tau1]*c[10][tau2]);
        rate += R_M*Ar40WM(tau1, tau2, y);
```

```
        R_P2 = 0.25*pow(qr,2)*c[2][tau1]*c[2][tau2]*eta;
        rate += pow(qr,2)*R_P2*Ar40WP2(tau1, tau2, y);

        R_P2M = eta*c[2][tau1]*c[0][tau2];
        rate += pow(qr,2)*R_P2M*Ar40WMP2(tau1, tau2, y);
        }
    }
    //GeV^-4*cm^-3*km^-1*s*c^6*hbar^2 to keV^-1 kg^-1 day^-1
    double conv = (rho0/2.0/pi/m_x)*1.69612985e14;


    double diff_rate = (4*pi/(2*Jval+1))*rate*conv;

    return diff_rate;
}
```

Recoil rate implementation for magnetic dipole Dark Matter

```
double RecoilRate_Isotropic::get_recoilrate_at(double Er_keV){

 //Units of the Bohr Magneton.

 double _vE = get_velocity_profile()->get_vE();
 double sigmav= 156.0;

 double cn[11];
 double cp[11];

 for(int k=0;k<=10;k++){
    cn[k] = 2*k*0;
    cp[k] = (2*k+1)*0; }

 double amu = 931.5e3;                // keV
 double q1 = sqrt(2*_A*amu*Er_keV);  //Recoil momentum in keV
 double alpha = 0.007297;
 double e = sqrt(4*TMath::Pi()*alpha);
 double m_p = 0.9315;

 //Bohr Magneton
 double mu_B = 297.45;  //GeV^-1 (in natural units)

 double mu_x = sqrt(_sigma0_cm2*TMath::Pi())/mu;

 //Operator 1
 cp[0] = e*(mu_x*mu_B)/(2.0*_Mwimp_GeV);

 //Operator 5
```

```
 cp[4] = 2*e*(mu_x*mu_B)*m_p/pow((q1*1e-6),2);

 double rate = dRdE_NREFT(Er_keV,_Mwimp_GeV,cp,cn,_A,_vE,sigmav,_v_esc);
 return rate;
}
```

Recoil rate implementation for millicharge Dark Matter

```
double RecoilRate_Isotropic::get_recoilrate_at(double Er_keV){

 double _vE = get_velocity_profile()->get_vE();
 double sigmav= 156.0;

 double rate = dRdE_milli(Er_keV,_Mwimp_GeV,_sigma0_cm2,_A,_vE, sigmav,_v_esc);
 return rate;
}
```

Recoil rate implementation for electric dipole Dark Matter

```
double RecoilRate_Isotropic::get_recoilrate_at(double Er_keV){

 double _vE = get_velocity_profile()->get_vE();
 double sigmav= 156.0;

 double rate = dRdE_elec(Er_keV,_Mwimp_GeV,_sigma0_cm2,_A,_vE, sigmav,_v_esc);
 return rate;
}
```

Bibliography

1. Ajaj, R. *et al.* Search for dark matter with a 231-day exposure of liquid argon using DEAP-3600 at SNOLAB. *Phys. Rev.* **D100,** 022004. arXiv: 1902.04048 [astro-ph.CO] (2019).
2. Baxter, D. *et al.* Recommended conventions for reporting results from direct dark matter searches. arXiv: 2105.00599 [hep-ex] (May 2021).
3. Adhikari, P. *et al.* Constraints on dark matter-nucleon effective couplings in the presence of kinematically distinct halo substructures using the DEAP-3600 detector. *Phys. Rev. D* **102,** 082001. arXiv: 2005.14667 [astro-ph.CO] (2020).
4. Fan, J., Reece, M. & Wang, L.-T. Non-relativistic effective theory of dark matter direct detection. *J. Cosmol. Astropart. Phys.* **1011,** 042. arXiv: 1008.1591 [hep-ph] (2010).
5. Fitzpatrick, A. L., Haxton, W., Katz, E., Lubbers, N. & Xu, Y. The effective field theory of dark matter direct detection. *J. Cosmol. Astropart. Phys.* **1302,** 004. arXiv: 1203.3542 [hep-ph] (2013).
6. Anand, N., Fitzpatrick, A. L. & Haxton, W. C. Weakly Interacting Massive Particle-nucleus elastic scattering response. *Phys. Rev.* **C89,** 065501. arXiv: 1308.6288 [hep-ph] (2014).
7. Aprile, E. *et al.* Effective field theory search for high-energy nuclear recoils using the XENON100 dark matter detector. *Phys. Rev. D* **96,** 042004. arXiv: 1705.02614 [astro-ph.CO] (2017).
8. Akerib, D. S. *et al.* Constraints on effective field theory couplings using 311.2 days of LUX data. *Phys. Rev. D* **104,** 062005. arXiv: 2102.06998 [astro-ph.CO] (2021).
9. Schneck, K. *et al.* Dark matter effective field theory scattering in direct detection experiments. *Phys. Rev. D* **91,** 092004. arXiv: 1503.03379 [astro-ph.CO] (2015).
10. Adhikari, G. *et al.* COSINE-100 and DAMA/LIBRA-phase2 in WIMP effective models. *JCAP* **06,** 048. arXiv: 1904.00128 [hep-ph] (2019).
11. Agnes, P. *et al.* Effective field theory interactions for liquid argon target in DarkSide-50 experiment. *Phys. Rev. D* **101,** 062002. arXiv: 2002.07794 [hep-ex] (2020).
12. Necib, L., Lisanti, M. & Belokurov, V. Inferred evidence for dark matter kinematic substructure with SDSS–Gaia. *The Astrophysical Journal* **874,** 3. https://doi.org/10.3847/1538-4357/ab095b (Mar. 2019).
13. Necib, L., Lisanti, M., Garrison-Kimmel, S., Wetzel, A., Sanderson, R., Hopkins, P. F., Faucher-Giguère, C.-A. & Kereš, D. Under the FIRElight: stellar tracers of the local dark matter velocity distribution in the Milky Way. *Astrophys. J* **883,** 27. ISSN: 1538-4357. http://dx.doi.org/10.3847/1538-4357/ab3afc (Sept. 2019).
14. Herzog-Arbeitman, J., Lisanti, M., Madau, P. & Necib, L. Empirical determination of dark matter velocities using metal-poor stars. *Phys. Rev. Lett.* **120,** 041102. arXiv: 1704.04499 [astro-ph.GA] (2018).

15. Herzog-Arbeitman, J., Lisanti, M. & Necib, L. The metal-poor stellar halo in RAVE-TGAS and its implications for the velocity distribution of dark matter. *J. Cosmol. Astropart. Phys.* **1804,** 052. arXiv: 1708.03635 [astro-ph.GA] (2018).
16. Ostdiek, B., Necib, L., Cohen, T., Freytsis, M., Lisanti, M., Garrison-Kimmel, S., Wetzel, A., Sanderson, R. E. & Hopkins, P. F. Cataloging accreted stars within *Gaia* DR2 using deep learning. *Astron. Astrophys.* **636,** A75. arXiv: 1907.06652 [astro-ph.GA] (2020).
17. Necib, L., Ostdiek, B., Lisanti, M., Cohen, T., Freytsis, M. & Garrison-Kimmel, S. Chasing Accreted Structures within Gaia DR2 using Deep Learning. *Astrophys. J.* **903,** 25. arXiv: 1907.07681 [astro-ph.GA] (2020).
18. Baushev, A. N. Extragalactic dark matter and direct detection experiments. *Astrophys. J* **771,** 117. https://doi.org/10.1088%2F0004-637x%2F771%2F2%2F117 (June 2013).
19. Freese, K., Gondolo, P. & Stodolsky, L. On the direct detection of extragalactic weakly interacting massive particles. *Phys. Rev. D* **64,** 123502. https://link.aps.org/doi/10.1103/PhysRevD.64.123502 (12 Oct. 2001).
20. O'Hare, C. A. J., McCabe, C., Evans, N. W., Myeong, G. & Belokurov, V. Dark matter hurricane: measuring the S1 stream with dark matter detectors. *Phys. Rev.* **D98,** 103006. arXiv: 1807.09004 [astro-ph.CO] (2018).
21. Evans, N. W., O'Hare, C. A. J. & McCabe, C. Refinement of the standard halo model for dark matter searches in light of the Gaia Sausage. *Phys. Rev.* **D99,** 023012. arXiv: 1810.11468 [astro-ph.GA] (2019).
22. Buch, J., Fan, J. & Leung, J. S. C. Implications of the Gaia Sausage for dark matter nuclear interactions. *Phys. Rev.* **D101,** 063026. arXiv: 1910.06356 [hep-ph] (2020).
23. Ade, P. A. R. *et al.* Planck 2013 results. I. Overview of products and scientific results. *Astron. Astrophys.* **571,** A1. arXiv: 1303.5062 [astro-ph.CO] (2014).
24. Adam, R. *et al.* Planck 2015 results. I. Overview of products and scientific results. *Astron. Astrophys.* **594,** A1. arXiv: 1502.01582 [astro-ph.CO] (2016).
25. Bertone, G., Hooper, D. & Silk, J. Particle dark matter: evidence, candidates and constraints. *Phys. Rept.* **405,** 279–390. arXiv: hep-ph/0404175 (2005).
26. Schumann, M. Direct detection of WIMP dark matter: concepts and status. *J. Phys. G* **46,** 103003. arXiv: 1903.03026 [astro-ph.CO] (2019).
27. Roszkowski, L., Sessolo, E. M. & Trojanowski, S. WIMP dark matter candidates and searches—current status and future prospects. *Rept. Prog. Phys.* **81,** 066201. arXiv: 1707.06277 [hep-ph] (2018).
28. Feng, J. L. Dark matter candidates from particle physics and methods of detection. *Ann. Rev. Astron. Astrophys.* **48,** 495–545. arXiv: 1003.0904 [astro-ph.CO] (2010).
29. Bertone, G. & Hooper, D. History of dark matter. *Rev. Mod. Phys.* **90,** 045002. arXiv: 1605.04909 [astro-ph.CO] (2018).
30. Navarro, J. F., Frenk, C. S. & White, S. D. M. The structure of cold dark matter halos. *Astrophys. J.* **462,** 563–575. arXiv: astro-ph/9508025 (1996).
31. Read, J. I. The local dark matter density. *J. Phys. G* **41,** 063101. arXiv: 1404.1938 (2014).
32. Benito, M., Iocco, F. & Cuoco, A. Uncertainties in the galactic dark matter distribution: an update. *Phys. Dark Univ.* **32,** 100826. arXiv: 2009.13523 [astro-ph.GA] (2021).

33. Ludlow, A. D., Bose, S., Angulo, R. E., Wang, L., Hellwing, W. A., Navarro, J. F., Cole, S. & Frenk, C. S. The mass–concentration–redshift relation of cold and warm dark matter haloes. *Mon. Not. Roy. Astron. Soc.* **460,** 1214–1232. arXiv: 1601.02624 [astro-ph.CO] (2016).
34. Iocco, F., Pato, M. & Bertone, G. Evidence for dark matter in the inner Milky Way. *Nature Phys.* **11,** 245–248. arXiv: 1502.03821 [astro-ph.GA] (2015).
35. Bhattacharjee, P., Chaudhury, S. & Kundu, S. Rotation curve of the Milky Way out to ∼200 kpc. *The Astrophysical Journal* **785,** 63. https://doi.org/10.1088/0004-637x/785/1/63 (Mar. 2014).
36. Begeman, K. G., Broeils, A. H. & Sanders, R. H. Extended rotation curves of spiral galaxies: dark haloes and modified dynamics. *Mon. Not. Roy. Astron. Soc.* **249,** 523 (1991).
37. Massey, R., Kitching, T. & Richard, J. The dark matter of gravitational lensing. *Rept. Prog. Phys.* **73,** 086901. arXiv: 1001.1739 [astro-ph.CO] (2010).
38. NASA, E. & Calçada, L. *Gravitational lensing in action* https://esahubble.org/images/heic1106c/. (accessed: 11.07.2021).
39. NASA ESA, J. R. & Kneib., J. *Annotated view of Abell 383* https://esahubble.org/images/heic1106b/. (accessed: 11.07.2021).
40. Paraficz, D., Kneib, J.-P., Richard, J., Morandi, A., Limousin, M., Jullo, E. & Martinez, J. The Bullet cluster at its best: weighing stars, gas, and dark matter. *Astron. Astrophys.* **594,** A121. ISSN: 1432-0746. http://dx.doi.org/10.1051/0004-6361/201527959 (Oct. 2016).
41. Clowe, D., Bradac, M., Gonzalez, A. H., Markevitch, M., Randall, S. W., Jones, C. & Zaritsky, D. A direct empirical proof of the existence of dark matter. *Astrophys. J. Lett.* **648,** L109–L113. arXiv: astro-ph/0608407 (2006).
42. Fixsen, D. J. The temperature of the Cosmic Microwave Background. *Astrophys. J* **707,** 916–920. https://doi.org/10.1088/0004-637x/707/2/916 (Nov. 2009).
43. Durrer, R. The Cosmic Microwave Background: the history of its experimental investigation and its significance for cosmology. *Class. Quant. Grav.* **32,** 124007. arXiv: 1506.01907 [astro-ph.CO] (2015).
44. Hu, W. & Dodelson, S. Cosmic Microwave Background anisotropies. *Ann. Rev. Astron. Astrophys.* **40,** 171–216. arXiv: astro-ph/0110414 (2002).
45. Hu, W., Sugiyama, N. & Silk, J. The physics of microwave background anisotropies. *Nature* **386,** 37–43. arXiv: astro-ph/9604166 (1997).
46. Aghanim, N. *et al.* Planck 2018 results. VI. Cosmological parameters. *Astron. Astrophys.* **641.** [Erratum: Astron.Astrophys. 652, C4 (2021)], A6. arXiv: 1807.06209 [astro-ph.CO] (2020).
47. Berezinsky, V., Bottino, A., Ellis, J. R., Fornengo, N., Mignola, G. & Scopel, S. Neutralino dark matter in supersymmetric models with nonuniversal scalar mass terms. *Astropart. Phys.* **5,** 1–26. arXiv: hep-ph/9508249 (1996).
48. Servant, G. & Tait, T. M. P. Is the lightest Kaluza-Klein particle a viable dark matter candidate? *Nucl. Phys. B* **650,** 391–419. arXiv: hep-ph/0206071 (2003).
49. Arcadi, G., Döring, C., Hasterok, C. & Vogl, S. Inelastic dark matter nucleus scattering. *JCAP* **12,** 053. arXiv: 1906.10466 [hep-ph] (2019).

50. Essig, R., Mardon, J. & Volansky, T. Direct detection of sub-GeV dark matter. *Phys. Rev. D* **85,** 076007. arXiv: 1108.5383 [hep-ph] (2012).
51. Kouvaris, C. & Pradler, J. Probing sub-GeV dark matter with conventional detectors. *Phys. Rev. Lett.* **118,** 031803. arXiv: 1607.01789 [hep-ph] (2017).
52. Aprile, E. *et al.* Search for light dark matter interactions enhanced by the Migdal effect or Bremsstrahlung in XENON1T. *Phys. Rev. Lett.* **123,** 241803. arXiv: 1907.12771 [hep-ex] (2019).
53. Ibe, M., Nakano, W., Shoji, Y. & Suzuki, K. Migdal effect in dark matter direct detection experiments. *JHEP* **03,** 194. arXiv: 1707.07258 [hep-ph] (2018).
54. Dolan, M. J., Kahlhoefer, F. & McCabe, C. Directly detecting sub-GeV dark matter with electrons from nuclear scattering. *Phys. Rev. Lett.* **121,** 101801. arXiv: 1711.09906 [hep-ph] (2018).
55. Figueroa-Feliciano, E. Direct detection searches for WIMP dark matter. *Progress in Particle and Nuclear Physics* **66,** 661–673. ISSN: 0146-6410. https://www.sciencedirect.com/science/article/pii/S0146641011000044 (2011).
56. Lewin, J. D. & Smith, P. F. Review of mathematics, numerical factors, and corrections for dark matter experiments based on elastic nuclear recoil. *Astropart. Phys.* **6,** 87–112 (1996).
57. Aprile, E. *et al.* Dark matter search results from a one ton-year exposure of XENON1T. *Phys. Rev. Lett.* **121,** 111302. arXiv: 1805.12562 [astro-ph.CO] (2018).
58. Bernabei, R. *et al.* First model independent results from DAMA/LIBRA-phase2. *Nucl. Phys. Atom. Energy* **19,** 307–325. arXiv: 1805.10486 [hep-ex] (2018).
59. Amare, J. *et al.* Annual modulation results from three years exposure of ANAIS-112. *Phys. Rev. D* **103,** 102005. arXiv: 2103.01175 [astro-ph.IM] (2021).
60. Adhikari, G. *et al.* Search for a dark matter-induced annual modulation signal in NaI(Tl) with the COSINE-100 experiment. *Phys. Rev. Lett.* **123,** 031302. arXiv: 1903.10098 (2019).
61. Drozd, A., Grzadkowski, B., Gunion, J. F. & Jiang, Y. Isospin-violating dark-matter-nucleon scattering via two-Higgs-doublet-model portals. *JCAP* **10,** 040. arXiv: 1510.07053 [hep-ph] (2016).
62. Hamaguchi, K., Liew, S. P., Moroi, T. & Yamamoto, Y. Isospin-violating dark matter with colored mediators. *JHEP* **05,** 086. arXiv: 1403.0324 [hep-ph] (2014).
63. Bélanger, G., Goudelis, A., Park, J.-C. & Pukhov, A. Isospin-violating dark matter from a double portal. *JCAP* **02,** 020. arXiv: 1311.0022 [hep-ph] (2014).
64. Aprile, E. *et al.* Excess electronic recoil events in XENON1T. *Phys. Rev. D* **102,** 072004. arXiv: 2006.09721 [hep-ex] (2020).
65. Amole, C. *et al.* Dark matter search results from the complete exposure of the PICO-60 C_3F_8 Bubble Chamber. *Phys. Rev. D* **100,** 022001. arXiv: 1902.04031 [astro-ph.CO] (2019).
66. Agnese, R. *et al.* Projected sensitivity of the SuperCDMS SNOLAB experiment. *Phys. Rev. D* **95,** 082002. arXiv: 1610.00006 [physics.ins-det] (2017).
67. Akerib, D. S. *et al.* The LUX-ZEPLIN (LZ) experiment. *Nucl. Instrum. Meth. A* **953,** 163047. arXiv: 1910.09124 [physics.ins-det] (2020).
68. Bartram, C. *et al.* Axion dark matter experiment: Run 1B analysis details. *Phys. Rev. D* **103,** 032002. arXiv: 2010.06183 [astro-ph.CO] (2021).

69. Meng, Y. *et al.* Dark matter search results from the PandaX-4T commissioning run. arXiv: 2107.13438 [hep-ex] (July 2021).
70. Aguilar-Arevalo, A. *et al.* Results on low-mass weakly interacting massive particles from a 11 kg-day target exposure of DAMIC at SNOLAB. *Phys. Rev. Lett.* **125,** 241803. arXiv: 2007.15622 [astro-ph.CO] (2020).
71. Barak, L. *et al.* SENSEI: direct-detection results on sub-GeV dark matter from a new skipper-CCD. *Phys. Rev. Lett.* **125,** 171802. arXiv: 2004.11378 [astro-ph.CO] (2020).
72. Picciau, E. Latest results of dark matter detection with the DarkSide experiment. *Nuovo Cim. C* **43** (eds D'Ambrosio, G. & De Nardo, G.) 26 (2020).
73. Jiang, H. *et al.* Limits on light Weakly Interacting Massive Particles from the first 102.8 kg $\times$ day data of the CDEX-10 experiment. *Phys. Rev. Lett.* **120,** 241301. arXiv: 1802.09016 [hep-ex] (2018).
74. Aalseth, C. E. *et al.* DarkSide-20k: A 20 tonne two-phase LAr TPC for direct dark matter detection at LNGS. *Eur. Phys. J. Plus* **133,** 131. arXiv: 1707.08145 [physics.ins-det] (2018).
75. Aprile, E. *et al.* Projected WIMP sensitivity of the XENONnT dark matter experiment. *JCAP* **11,** 031. arXiv: 2007.08796 [physics.ins-det] (2020).
76. Arnaud, Q. *et al.* First results from the NEWS-G direct dark matter search experiment at the LSM. *Astropart. Phys.* **97,** 54–62. arXiv: 1706.04934 [astro-ph.IM] (2018).
77. Flores, L. J. *et al.* Physics reach of a low threshold scintillating argon bubble chamber in coherent elastic neutrino-nucleus scattering reactor experiments. *Phys. Rev. D* **103,** L091301. arXiv: 2101.08785 [hep-ex] (2021).
78. Antonello, M. *et al.* The SABRE project and the SABRE proof-of-principle. *Eur. Phys. J. C* **79,** 363. arXiv: 1806.09340 [physics.ins-det] (2019).
79. Billard, J. *et al.* Direct detection of dark matter – APPEC committee report. arXiv: 2104.07634 [hep-ex] (Apr. 2021).
80. Aprile, E. *et al.* Observation of two-neutrino double electron capture in ^{124}Xe with XENON1T. *Nature* **568,** 532–535. arXiv: 1904.11002 [nucl-ex] (2019).
81. Vahsen, S. E., O'Hare, C. A. J. & Loomba, D. Directional recoil detection. *Ann. Rev. Nucl. Part. Sci.* **71,** 189–224. arXiv: 2102.04596 [physics.ins-det] (2021).
82. Vahsen, S. E. *et al.* CYGNUS: Feasibility of a nuclear recoil observatory with directional sensitivity to dark matter and neutrinos. arXiv: 2008.12587 [physics.ins-det] (Aug. 2020).
83. O'Hare, C. A. J. Can we overcome the neutrino floor at high masses? *Phys. Rev. D* **102,** 063024. arXiv: 2002.07499 [astro-ph.CO] (2020).
84. Amaudruz, P. A. *et al.* Design and construction of the DEAP-3600 dark matter detector. *Astropart. Phys.* **108,** 1–23. arXiv: 1712.01982 [astro-ph.IM] (2019).
85. Wahl, C. G., Bernard, E. P., Lippincott, W. H., Nikkel, J. A., Shin, Y. & McKinsey, D. N. Pulse-shape discrimination and energy resolution of a liquid-argon scintillator with xenon doping. *JINST* **9,** P06013. arXiv: 1403.0525 [physics.ins-det] (2014).
86. Lidgard, J. *Pulse shape discrimination studies in liquid argon for the DEAP-1 detector* MA thesis (Queen's University, 2008).

87. Lindner, T. DEAP-3600 data acquisition system. *Journal of Physics: Conference Series* **664,** 082026. https://doi.org/10.1088/1742-6596/664/8/082026 (Dec. 2015).
88. Cao, H. *et al.* Measurement of scintillation and ionization yield and scintillation pulse shape from nuclear recoils in liquid argon. *Phys. Rev. D* **91,** 092007. arXiv: 1406.4825 [physics.ins-det] (2015).
89. Amaudruz, P. A. *et al.* First results from the DEAP-3600 dark matter search with argon at SNOLAB. *Phys. Rev. Lett.* **121,** 071801. arXiv: 1707.08042 [astro-ph.CO] (2018).
90. Lehnert, B. Backgrounds in the DEAP-3600 dark matter experiment. *J. Phys. Conf. Ser.* **1342** (eds Clark, K., Jillings, C., Kraus, C., Saffin, J. & Scorza, S.) 012072. arXiv: 1805.06073 [astro-ph.IM] (2020).
91. Langrock, S. Energy response and position reconstruction in the DEAP-3600 dark matter experiment. **1342,** 012071. https://doi.org/10.1088/1742-6596/1342/1/012071 (Jan. 2020).
92. Chen, Y. Position reconstruction using photon timing for the DEAP-3600 dark matter experiment. *JINST* **15,** C05061. arXiv: 2004.02058 [physics.ins-det] (2020).
93. Westerdale, S. *Latest results from the DEAP-3600 dark matter search with 231 live days at SNOLAB* in *54th Rencontres de Moriond on Electroweak Interactions and Unified Theories* (2019), 215–220.
94. Westerdale, S. Analysis and dark matter search results from DEAP-3600 with 231 live days at SNOLAB. *J. Phys. Conf. Ser.* **1468** (ed Nakahata, M.) 012031 (2020).
95. Viel, S. Dark matter search results from DEAP-3600 at SNOLAB. *PoS* **ICHEP2020,** 655 (2021).
96. Ohsumi, H. *et al.* Gamma-ray flux in the Frejus underground laboratory measured with NaI detector. *Nucl. Instrum. Meth. A* **482,** 832–839 (2002).
97. Aharmim, B. *et al.* Measurement of the cosmic ray and neutrino-induced muon flux at the Sudbury Neutrino Observatory. *Phys. Rev. D* **80,** 012001. arXiv: 0902.2776 [hep-ex] (2009).
98. Pollmann, T. R. & Smith, B. Database support of detector operation and data analysis in the DEAP-3600 dark matter experiment. *Eur. Phys. J. C* **79,** 683. arXiv: 1905.02964 [physics.ins-det] (2019).
99. Henderson, S., Monroe, J. & Fisher, P. The Maximum Patch method for directional dark matter detection. *Phys. Rev. D* **78,** 015020. arXiv: 0801.1624 [astro-ph] (2008).
100. Lisanti, M. *Lectures on dark matter physics* in *Proceedings, Theoretical Advanced Study Institute in Elementary Particle Physics: New Frontiers in Fields and Strings (TASI 2015): Boulder, CO, USA, June 1-26, 2015* (2017), 399–446. arXiv: 1603.03797 [hep-ph].
101. Baudis, L. Direct dark matter detection: the next decade. *Phys. Dark Univ.* **1,** 94–108. arXiv: 1211.7222 [astro-ph.IM] (2012).
102. Marrodán Undagoitia, T. & Rauch, L. Dark matter direct-detection experiments. *J. Phys. G* **43,** 013001. arXiv: 1509.08767 [physics.ins-det] (2016).
103. Catena, R. & Schwabe, B. Form factors for dark matter capture by the Sun in effective theories. *J. Cosmol. Astropart. Phys.* **1504,** 042. arXiv: 1501.03729 [hep-ph] (2015).

104. Cerdeno, D. G. & Green, A. M. Direct detection of WIMPs, 347–369. arXiv: 1002.1912 [astro-ph.CO] (Feb. 2010).

105. Helm, R. H. Inelastic and elastic scattering of 187-MeV electrons from selected even-even nuclei. *Phys. Rev.* **104,** 1466–1475. https://link.aps.org/doi/10.1103/PhysRev.104.1466 (5 1956).

106. Gresham, M. I. & Zurek, K. M. Effect of nuclear response functions in dark matter direct detection. *Phys. Rev. D* **89,** 123521. arXiv: 1401.3739 [hep-ph] (2014).

107. Ho, C. M. & Scherrer, R. J. Anapole dark matter. *Phys. Lett B* **722,** 341–346. ISSN: 0370-2693. http://dx.doi.org/10.1016/j.physletb.2013.04.039 (May 2013).

108. Sigurdson, K., Doran, M., Kurylov, A., Caldwell, R. R. & Kamionkowski, M. Dark matter electric and magnetic dipole moments. *Phys. Rev. D* **70.** [Erratum: Phys.Rev.D 73, 089903 (2006)], 083501. arXiv: astro-ph/0406355 (2004).

109. Kavanagh, B. J. & Edwards, T. D. P. WIMpy_NREFT v1.1 [Computer Software], doi:10.5281/zenodo.1230503. Available at *https://github.com/bradkav/WIMpy_NREFT* 2018.

110. Helmi, A. Streams, substructures, and the early history of the Milky Way. *Annu. Rev. Astron. Astrophys.* **58,** 205–256. eprint: https://doi.org/10.1146/annurev-astro-032620-021917. https://doi.org/10.1146/annurev-astro-032620-021917 (2020).

111. Myeong, G. C., Evans, N. W., Belokurov, V., Amorisco, N. C. & Koposov, S. Halo substructure in the SDSS-Gaia catalogue : streams and clumps. *Mon. Not. Roy. Astron. Soc.* **475,** 1537–1548. arXiv: 1712.04071 [astro-ph.GA] (2018).

112. Li, H., Du, C., Liu, S., Donlon, T. & Newberg, H. J. The substructures in the local stellar halo from Gaia and LAMOST. *The Astrophysical Journal* **874,** 74. ISSN: 1538-4357. http://dx.doi.org/10.3847/1538-4357/ab06f4 (Mar. 2019).

113. O'Hare, C. A. J., Evans, N. W., McCabe, C., Myeong, G. & Belokurov, V. Velocity substructure from Gaia and direct searches for dark matter. *Phys. Rev. D* **101,** 023006. arXiv: 1909.04684 [astro-ph.GA] (2020).

114. *European Space Agency (ESA) mission Gaia.* https://www.cosmos.esa.int/gaia.

115. *Sloan Digital Sky Survey (SDSS) telescope.* https://www.sdss.org/.

116. Green, A. M. Astrophysical uncertainties on the local dark matter distribution and direct detection experiments. *J. Phys. G* **44,** 084001. arXiv: 1703.10102 [astro-ph.CO] (2017).

117. McCabe, C. Astrophysical uncertainties of dark matter direct detection experiments. *Phys. Rev. D* **82,** 023530. https://link.aps.org/doi/10.1103/PhysRevD.82.023530 (2 July 2010).

118. Magni, S. *Astrophysical aspects of dark matter direct detection* Theses (Université Montpellier, Nov. 2015). https://tel.archives-ouvertes.fr/tel-01986333.

119. Zyla, P. *et al.* Review of Particle Physics. *PTEP* **2020,** 083C01 (2020).

120. Belokurov, V, Erkal, D, Evans, N. W., Koposov, S. E. & Deason, A. J. Co-formation of the disc and the stellar halo. *Mon. Not. Roy. Astron. Soc.* **478,** 611–619. ISSN: 1365-2966. http://dx.doi.org/10.1093/mnras/sty982 (June 2018).

121. Deason, A. J., Belokurov, V., Koposov, S. E. & Lancaster, L. Apocenter pile-up: origin of the stellar halo density break. *Astrophys. J* **862,** L1. ISSN: 2041-8213. http://dx.doi.org/10.3847/2041-8213/aad0ee (July 2018).

122. Myeong, G. C., Evans, N. W., Belokurov, V., Sanders, J. L. & Koposov, S. E. The Sausage globular clusters. *Astrophys. J.* **863,** L28. arXiv: 1805.00453 [astro-ph.GA] (2018).

123. *The Gaia Sausage. The major collision that changed the Milky Way galaxy* https://people.ast.cam.ac.uk/~vasily/gaia_sausage/info.html. Accessed: 2020-01-16.

124. *Dark matter in disequilibrium: the local velocity distribution from SDSS-GAIA* https://github.com/linoush/DM_Velocity_Distribution. Accessed: 2020-01-16.

125. Myeong, G. C., Evans, N. W., Belokurov, V, Sanders, J. L. & Koposov, S. E. Discovery of new retrograde substructures: the shards of ω·Centauri? *Mon. Not. Roy. Astron. Soc.* **478,** 5449–5459. ISSN: 0035-8711. https://doi.org/10.1093/mnras/sty1403 (June 2018).

126. Necib, L., Ostdiek, B., Lisanti, M., Cohen, T., Freytsis, M., Garrison-Kimmel, S., Hopkins, P. F., Wetzel, A. & Sanderson, R. Evidence for a vast prograde stellar stream in the solar vicinity. *Nature Astron.* **4,** 1078–1083. arXiv: 1907.07190 [astro-ph.GA] (2020).

127. Helmi, A., White, S. D. M., de Zeeuw, P. T. & Zhao, H.-S. Debris streams in the solar neighbourhood as relicts from the formation of the Milky Way. *Nature* **402,** 53–55. arXiv: astro-ph/9911041 [astro-ph] (1999).

128. Koppelman, H. H., Helmi, A., Massari, D., Roelenga, S. & Bastian, U. Characterization and history of the Helmi streams with Gaia DR2. *Astron. Astrophys.* **625,** A5. ISSN: 1432-0746. http://dx.doi.org/10.1051/0004-6361/201834769 (Apr. 2019).

129. Koppelman, H., Helmi, A. & Veljanoski, J. One large blob and many streams frosting the nearby stellar halo in Gaia DR2. *Astrophys. J* **860,** L11. ISSN: 2041-8213. http://dx.doi.org/10.3847/2041-8213/aac882 (June 2018).

130. Stiff, D., Widrow, L. M. & Frieman, J. Signatures of hierarchical clustering in dark matter detection experiments. *Phys. Rev. D* **64,** 083516. https://link.aps.org/doi/10.1103/PhysRevD.64.083516 (8 Sept. 2001).

131. Gelmini, G. & Gondolo, P. Weakly interacting massive particle annual modulation with opposite phase in late-infall halo models. *Phys. Rev. D* **64,** 023504. https://link.aps.org/doi/10.1103/PhysRevD.64.023504 (2 June 2001).

132. Green, A. M. Potential weakly interacting massive particle signature for the caustic ring halo model. *Phys. Rev. D* **63,** 103003. https://link.aps.org/doi/10.1103/PhysRevD.63.103003 (10 Apr. 2001).

133. Sikivie, P., Tkachev, I. I. & Wang, Y. Secondary infall model of galactic halo formation and the spectrum of cold dark matter particles on Earth. *Phys. Rev. D* **56,** 1863–1878. https://link.aps.org/doi/10.1103/PhysRevD.56.1863 (4 Aug. 1997).

134. Smith, M. C. *et al.* The RAVE survey: constraining the local galactic escape speed. *Mon. Not. Roy. Astron. Soc.* **379,** 755–772. arXiv: astro-ph/0611671 [astro-ph] (2007).

135. Feng, J. L., Kumar, J. & Sanford, D. Xenophobic dark matter. *Phys. Rev.* **D88,** 015021. arXiv: 1306.2315 [hep-ph] (2013).

136. Yaguna, C. E. New constraints on Xenonphobic dark matter from DEAP-3600. *J. Cosmol. Astropart. Phys.* **1904,** 041. arXiv: 1902.10256 [hep-ph] (2019).

137. Yaguna, C. E. Isospin-violating dark matter in the light of recent data. *Phys. Rev.* **D95,** 055015. arXiv: 1610.08683 [hep-ph] (2017).

138. Adhikari, P. *et al.* First direct detection constraints on Planck-scale mass dark matter with multiple-scatter signatures using the DEAP-3600 detector. arXiv: 2108.09405 (Aug. 2021).